

Solid State Phase Transformation Kinetics

von der Fakultät Chemie der Universität Stuttgart zur
Erlangung der Würde eines Doktors der Naturwissenschaften
(Dr.rer.nat) genehmigte Abhandlung

vorgelegt von

ANTONIUS THEODORUS WILHELMUS KEMPEN

aus Kamerik/Niederlande

Hauptberichter: Prof. Dr. Ir. E.J. Mittemeijer
Mitberichter: Prof. Dr. Ir. S. van der Zwaag
Tag der mündlichen Prüfung: 20. November 2001

INSTITUT FÜR METALLKUNDE DER UNIVERSITÄT STUTTGART
MAX-PLANCK-INSTITUT FÜR METALLFORSCHUNG STUTTGART

2001

Contents

1	INTRODUCTION	1
1.1	SCOPE AND CONTENTS OF THIS THESIS	1
2	DETERMINATION AND INTERPRETATION OF ISOTHERMAL AND NON-ISOTHERMAL TRANSFORMATION KINETICS; THE EFFECTIVE ACTIVATION ENERGIES IN TERMS OF NUCLEATION AND GROWTH	5
	ABSTRACT	5
2.1	INTRODUCTION	7
2.2	THE PATH VARIABLE FOR ISOTHERMAL AND NON-ISOTHERMAL TRANSFORMATIONS	7
2.3	GENERAL KINETIC THEORY	8
2.4	VALIDITY OF JOHNSON-MEHL-AVRAMI DESCRIPTION	14
2.5	DETERMINATION OF KINETIC PARAMETERS	18
2.6	DETERMINATION AND INTERPRETATION OF KINETIC PARAMETERS; PRACTICAL LIMITS IN THE USE OF THE JMA DESCRIPTION	19
2.7	CONCLUSIONS	28
	APPENDIX A: CALCULATING THE KINETIC PARAMETERS ANALYTICALLY	30
3	THE ISOTHERMAL AND ISOCHRONAL KINETICS OF THE CRYSTALLISATION OF BULK AMORPHOUS $Pd_{40}Cu_{30}P_{20}Ni_{10}$	35
	ABSTRACT	35
3.1	INTRODUCTION	37
3.2	TRANSFORMATION KINETICS	38
3.3	EXPERIMENTAL	40
3.4	RESULTS AND EVALUATION	43
3.5	GENERAL DISCUSSION	50
3.6	CONCLUSIONS	52
4	KINETICS OF CONSECUTIVE, COUPLED PHASE TRANSFORMATIONS	53
	ABSTRACT	53
4.1	INTRODUCTION	55
4.2	KINETIC MODEL	55
4.3	EXPERIMENTAL PROCEDURES AND DATA EVALUATION	57
4.4	RESULTS AND DISCUSSION	57
4.5	CONCLUSIONS	59
5	CRYSTALLISATION KINETICS OF AMORPHOUS MAGNESIUM-RICH MAGNESIUM-COPPER AND MAGNESIUM-NICKEL ALLOYS	61
	ABSTRACT	61
5.1	INTRODUCTION	63
5.2	THEORETICAL BACKGROUND	63

5.3	EXPERIMENTAL	65
5.4	RESULTS AND EVALUATION	69
5.5	CONCLUDING DISCUSSION	85
5.6	CONCLUSIONS	87
5.7	ACKNOWLEDGEMENT	88
6	CALIBRATION AND DESMEARING OF A DIFFERENTIAL THERMAL ANALYSIS MEASUREMENT SIGNAL UPON HEATING AND COOLING	89
	ABSTRACT	89
6.1	INTRODUCTION	91
6.2	CALIBRATION AND DESMEARING METHODS FOR DTA	91
6.3	DTA HEAT FLUX MODEL	93
6.4	DATA EVALUATION	96
6.5	EXPERIMENTAL	98
6.6	RESULTS AND DISCUSSION	98
6.7	CONCLUSIONS	104
7	THE KINETICS OF THE AUSTENITE–FERRITE PHASE TRANSFORMATION OF FE-MN; DIFFERENTIAL THERMAL ANALYSIS DURING COOLING	105
	ABSTRACT	105
7.1	INTRODUCTION	107
7.2	PHASE TRANSFORMATION KINETICS	107
7.3	EXPERIMENTAL	111
7.4	RESULTS AND DISCUSSION	115
7.5	CONCLUSIONS	124
8	ZUSAMMENFASSUNG	125
8.1	EINFÜHRUNG	125
8.2	KINETISCHES MODELL	125
8.3	EXPERIMENTELLES	129
8.4	ERGEBNISSE	130
	REFERENCES	135
	CURRICULUM VITAE	143
	DANKSAGUNG	145

1 Introduction

The properties of materials depend on chemical composition and microstructure. Thus, the background of improvement of materials involves changes of the composition and/or microstructure. Without knowledge of this background, craftsmen had obtained the skill, using purely empirical procedures, to improve the properties of iron in the Middle Ages [1]. Albeit unrecognised, they used a phase transformation to change the microstructure, i.e. the phases present and their grain size and shape. Similarly, aluminium alloys were precipitation hardened at the beginning of the 20th century, without knowledge of the phase transformation involved [1]. A better understanding of these results evolved in the 20th century, leading to improvement of the processing conditions, and thus improvement of the material properties. Nowadays, steels are often hot rolled after casting, where the combination of deformation and elevated temperatures determine the obtained microstructure [2, 3]. The precipitation hardening of aluminium is optimised as well [4]. Mostly, the processing parameters are still obtained empirically. Reliable (non-empirical) assessment of the processing parameters, based on the thermodynamics and kinetics of the phase transformations, is a next goal in the development of metallurgy. The economical urge is to control solid state phase transformations in order to improve material properties. The scientific interest is the description of the transformations, and the recognition and the understanding of the processes which govern the phase transformation. The main incentive for this thesis is to give a *general* model description of the kinetics of solid state phase transformations.

1.1 Scope and contents of this thesis

The description of solid state phase transformation has long been a field of interest, where especially the contributions from Johnson and Mehl [5] and Avrami [6-8], known as the Johnson-Mehl-Avrami model (JMA) are, and have been, influential. The derivation of the JMA kinetics is based on the combination of three specific partial processes: nucleation, growth, and impingement of growing particles. The nucleation processes considered are continuous nucleation, i.e. the nucleation rate is temperature dependent according to an Arrhenius equation, and site saturation, where all nuclei are present before the growth starts. The growth processes considered are volume diffusion controlled, or interface controlled. The impingement process considered is hard impingement of homogeneously dispersed particles. Only for combinations of the mentioned nucleation, growth, and impingement processes, the resulting kinetic model is the Johnson-Mehl-Avrami (JMA) model.

This resulting model has been adopted very widely, however mostly on a empirical

basis. Without any considerations the JMA model has been applied, not realising that in certain cases (some of) the basic assumptions in the derivation of the JMA model could not hold. In Chapter 2 and 3 of this thesis one of these cases is explored both experimentally and mathematically: the case where a mixture of nucleation models occurs. Although such cases are found to occur (as is evidenced by the value of the JMA exponent, cf. Table 3.1) experimentally, this case has, strictly speaking, not been possible to describe by the JMA model. However, it is shown in Chapter 2 numerically that the JMA model gives a very good approximation of phase transformation where the nucleation model is of mixed nature.

In order to perform this numerical calculation the formalism of the Johnson-Mehl-Avrami derivation is adopted, however different nucleation models are used, thus resulting in a more *general* kinetic phase transformation model. Not in all cases, this model leads to an analytical solution. Throughout this entire thesis, this general phase transformation model is used upon adopting several nucleation, growth and impingement models, according to specific properties of the studied model systems. Based on the knowledge of the microstructure of the materials researched, the according nucleation, growth and impingement models have been selected, resulting in a model description of the transformation kinetics. The model description could then be compared with the experimentally determined transformation kinetics. In this thesis, different model systems have been researched applying several experimental techniques.

In Chapter 3, the power compensated differential scanning calorimetry (DSC) has been used to determine the isothermal and isochronal crystallisation kinetics of the bulk amorphous alloy $\text{Pd}_{40}\text{Cu}_{30}\text{P}_{20}\text{Ni}_{10}$. The resulting microstructure has been observed by Scanning Electron Microscopy. Here, isothermal annealing before the crystallisation has been performed in order to vary the influence of the nucleation in the entire crystallisation process. This variation, in combination with the phase transformation model as adopted in Chapter 2 allows for determination of the separate activation energies for nucleation and growth.

In Chapter 4, the kinetic model has been adopted for the description of two consecutive, coupled phase transformations. This description has been applied to the two occurring stages of crystallisation of the amorphous $\text{Mg}_{50}\text{Ni}_{30}\text{La}_{20}$, which has been detected by DSC.

Chapter 5 treats the isothermal and isochronal crystallisation of amorphous Mg-rich Mg-Ni and Mg-Cu alloys as observed by DSC and in situ crystallisation during high temperature X-ray diffraction. Associated resulting microstructures have been observed using Transmission Electron Microscopy and Electron Energy Loss Spectroscopy. The kinetic model has been able to describe the kinetics of phase transformation in specific cases, but not

in all cases studied. Thus, the boundaries of the validity of the kinetic model have been explored. It is e.g. found that the crystallisation of the Mg-Cu alloys is not isokinetic throughout the entire temperature window employed: at low temperatures the mechanism of transformation is different from the mechanism occurring at high temperatures. Hence, a single kinetic model cannot describe the phase transformation kinetics observed.

In Chapter 7, Differential Thermal Analysis (DTA) is employed for the study of the austenite to ferrite phase transformation of a Fe-Mn alloy during cooling. A new method for the calibration and desmearing of the DTA upon cooling has been developed as described in Chapter 6. The general kinetic model has been used in a different way as compared to the chapters 3-5. In those chapters, the kinetic model was used to simulate the phase transformation kinetics. In Chapter 7, the general model is used for the calculation of the unknown value of the interface velocity of the interface separating the austenite parent phase and the ferrite phase that forms during the transformation. The found values of the interface velocity do not agree with values of the interface velocity as given in literature, due to neglecting of misfit accommodation energy. The accommodation misfit energy is seen to be of the same order of magnitude as the chemical Gibbs energy difference.

2 Determination and interpretation of isothermal and non-isothermal transformation kinetics; the effective activation energies in terms of nucleation and growth

A.T.W. Kempen, F. Sommer and E.J. Mittemeijer

Keywords: phase transformation, isothermal, non-isothermal, kinetics, crystallisation, activation energy, Johnson-Mehl-Avrami, Pd₄₀Cu₃₀P₂₀Ni₁₀

Abstract

A general model for the kinetics of solid state phase transformations has been discussed. The model is valid for both isothermal as well as non-isothermal transformations. In certain specific cases, the model can be simplified such that it reduces to so-called Johnson-Mehl-Avrami (JMA) kinetics. The model kinetic parameters are independent of the time-temperature program. In addition, it has been shown that in certain cases where the presented model does not pertain to JMA exactly, the JMA description still holds within practical accuracy. This holds for example, for nucleation of mixed nature. In this case, it is possible to obtain the activation energies for growth and for nucleation, separately, from measurements, if it is possible to vary the nucleation mode, for example by pre-annealing. This determination of the separate activation energies has been tested on a virtual and a real phase transformation: crystallisation of glassy Pd₄₀Cu₃₀P₂₀Ni₁₀.

2.1 Introduction

Solid state phase transformations play an important role in the production of very many materials. Therefore, a great interest exists for a (potentially) general description of the kinetics, i.e. the time-temperature behaviour of phase transformations. Solid state phase transformations are generally the outcomes, for both isothermally and non-isothermally conducted annealings, of two, often simultaneously operating, mechanisms: nucleation and growth. For special cases of nucleation and growth, it is possible to derive the well-known analytical description of transformation kinetics according to Johnson, Mehl and Avrami (JMA) [5-8]. However, the JMA kinetics description is often applied generally, whereas it can be shown that, e.g. in the case of a non-isothermal transformation, such an analytical description does not hold without more ado (cf. section 2.4). Therefore, fitting of JMA kinetics to some phase transformation in general only yields a phenomenological description, and the obtained kinetic parameters do not necessarily have a physical meaning.

In the present work, a general kinetic, numerical model is described that combines nucleation and growth models. The model is applicable to both isothermal and non-isothermal transformations. This allows correction of erroneous application to non-isothermal transformation of certain concepts that in fact are only valid for isothermal transformations (see section 2.2). Depending on the type of nucleation and growth models adopted and approximations applied, it is possible to derive analytical expressions for the transformation kinetics, such as the JMA equation, as will be shown here.

The general model will be used (i) to assess the limits to which JMA can be applied in practice, (ii) to provide a physical interpretation of the values of the JMA parameters and (iii) to derive an expression for the overall activation energy of the transformation in terms of the separate activation energies for the nucleation and growth processes, that can be utilised in experimental analysis of transformation kinetics (section 2.6).

2.2 The path variable for isothermal and non-isothermal transformations

By measuring a suitable material parameter during a phase transformation, it is possible to trace the progress of this phase transformation as a function of the time(t)-temperature(T) program to which the material is subjected. The degree of transformation f ($0 \leq f \leq 1$) can be calculated from such data. The transformed fraction does not depend on t or $T(t)$ in a direct way: the thermal history of the material determines the degree of transformation. Therefore a path variable β is introduced which fully determines the degree of transformation, and

depends on the thermal history. The transformed fraction can then be given as [9]:

$$f = F(\beta). \quad (2.1)$$

The dependence of the path variable β on the thermal history (i.e. the path in the time-temperature diagram) can be described as the integral over time of a rate constant $k(T(t))$, not conceived to be dependent on t other than through T :

$$\beta = \int k(T(t)) dt. \quad (2.2)$$

This equation is compatible with the additivity rule [9], which supposes that throughout the temperature range of interest the transformation mechanism is the same. The rate constant $k(T(t))$ can be given by an Arrhenius equation:

$$k(T(t)) = k_0 \exp\left(-\frac{Q}{RT(t)}\right), \quad (2.3)$$

with k_0 as the pre-exponential factor, Q as the overall, effective activation energy (cf. section 2.4), and R as the gas constant.

It follows from Eq.(2.2) for isothermal annealing:

$$\beta = k(T)t. \quad (2.4)$$

In the literature, kinetic theories for non-isothermal transformations have usually been derived starting with formulations for isothermal transformations [10-13]. If a non-isothermal experiment is described as a series of subsequent isothermal anneals, each of infinitesimal length of time, and Eq.(2.4) is applied to each time step(as done in Refs.[11, 13] for isochronal (i.e. constant heating rate) experiments), then, obviously, the outcome is in accordance with the postulate Eq.(2.2). However, in the literature, the straightaway application of an equation equivalent to Eq.(2.4) to isochronal annealing is often erroneously made (see, e.g. Ref.[12]) which leads to false values for the kinetic parameters.

2.3 General kinetic theory

It is supposed that the overall transformation is the result of, more or less, simultaneously occurring nucleation and growth processes. One strives for determination of the kinetic parameters of these processes from the overall kinetics. First, different nucleation and growth models are considered.

2.3.1 Nucleation models

Various possible models are illustrated in Fig.2.1, for the case of isothermal annealing.

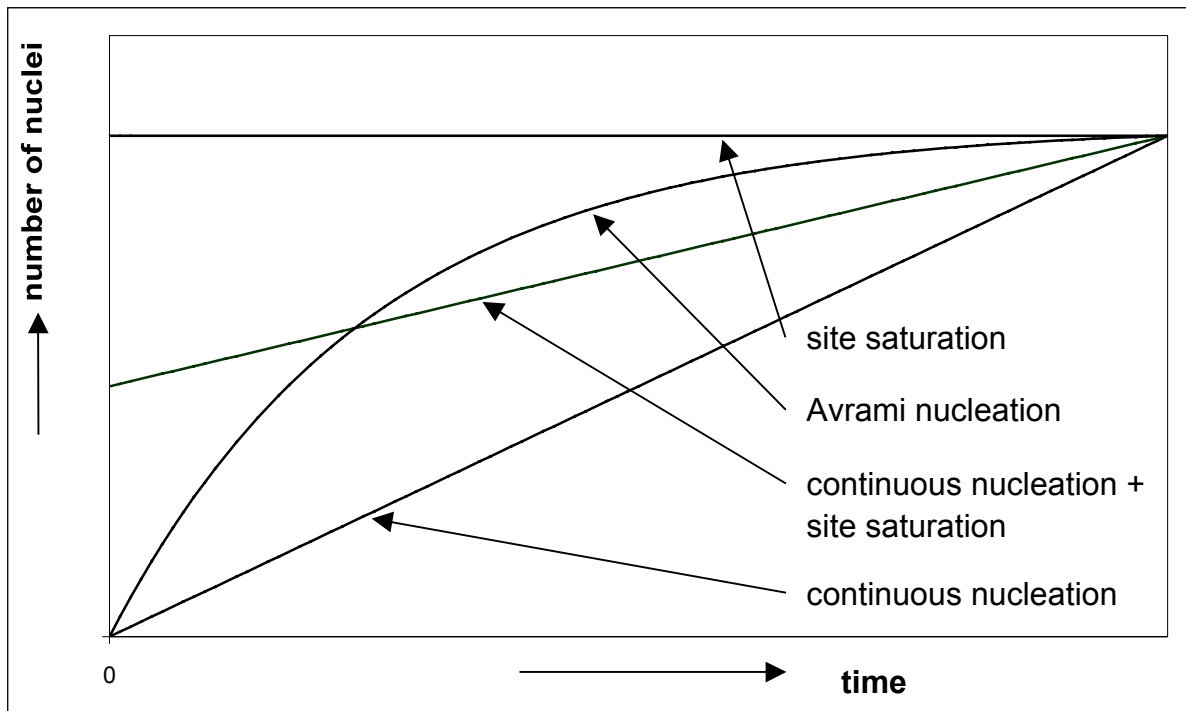


Fig.2.1 Schematic diagram of the number of nuclei as a function of time at constant temperature for four different nucleation models.

2.3.1.1 Continuous nucleation

Upon a phase transformation interfaces develop between the old and the new phases, and (possibly) misfit strain is introduced in the system. Whereas the production of the new phase releases chemical Gibbs energy, the creation of the interfaces and the introduction of misfit strain costs Gibbs energy. According to the classical nucleation theory [2], a critical particle size of the new phase can be defined such that if the particle (nucleus) is of sub-critical size, it costs energy to increase the size of the particle, whereas if the particle (nucleus) is of super-critical size, energy is released if the particle grows. The formation of particles of super-critical size from particles of sub-critical size is called nucleation.

The nucleation rate is determined by the number of nuclei of critical size and the rate of the jumping of atoms through the interface between the nucleus of critical size and the parent phase. The frequency of jumping through the interface is given by an Arrhenius term. The number of nuclei of critical size depends on an activation energy ΔG^* , which, according to the above description depends on the decrease of the chemical Gibbs free energy per unit volume, the interface energy per unit area interface and the misfit strain energy per unit volume. ΔG^* can be approximated as $\frac{A}{\Delta T^2}$ [3], where A is a constant, and ΔT is the undercooling or overheating with respect to the temperature at which the two phases are in equilibrium. If the

undercooling or the overheating is very large, ΔG^* can be considered to be very small. This is the case for a frozen-in metastable state, which transforms to the stable state upon heating. The nucleation rate per unit volume $\dot{N}(T)$ (i.e. the rate of formation of particles (nuclei) of supercritical size) is then only determined by the atomic mobility for transport through the interface, which can be given by an Arrhenius term:

$$\dot{N}(T) = N_0 \exp\left(-\frac{Q_N}{RT}\right), \quad (2.5a)$$

where N_0 is the pre-exponential factor, and Q_N is the temperature independent activation energy for nucleation. The definition of continuous nucleation implies that the number of particles (nuclei) N of supercritical size equals 0 at $t=0$.

2.3.1.2 Site saturation

The term site saturation is used in those cases where the number of (supercritical) nuclei does not change during the transformation: all nuclei, of number N^* , are present at $t=0$ already:

$$\dot{N}(T) = N^* \delta(t-0), \quad (2.5b)$$

with $\delta(t-0)$ denoting the Dirac function.

2.3.1.3 Mixture of Site Saturation and Continuous Nucleation

In practice, intermediate types of nucleation occur often: a significant amount of nuclei is present before the transformation starts and other nuclei are formed during the transformation. Two explicit models for this type of nucleation are given.

(a) Summation of site saturation and continuous nucleation

The first model involves that the nucleation rate at a certain stage is equal to some weighted sum of the nucleation rates according to the given continuous nucleation and site saturation models. By variation of the contribution of the two nucleation models, the mode of nucleation can be varied from pure site saturation to pure continuous nucleation:

$$\dot{N}(T) = N^* \delta(t-0) + N_0 \exp\left(-\frac{Q_N}{RT}\right). \quad (2.5c)$$

where N^* and N_0 express the relative contributions of the separate modes of nucleation.

(b) Avrami nucleation

The second model is due to Avrami [6-8]. The nuclei of supercritical size are formed from the nuclei of subcritical size N_{sub} ($\dot{N} = -\dot{N}_{sub}$), such that the total number of nuclei, of sub- and supercritical size, N' , is constant. The change of the number of nuclei of supercritical size is thus equal to the product of the number of nuclei of subcritical size, N_{sub} , and the rate, λ , at which an individual subcritical nucleus becomes supercritical:

$$\dot{N} = -\dot{N}_{sub} = \lambda N_{sub} \quad (2.6)$$

It is supposed that λ obeys Arrhenius-type temperature dependence:

$$\lambda = \lambda_0 \exp\left(-\frac{Q_N}{RT}\right). \quad (2.7)$$

with λ_0 as the pre-exponential constant.

Upon integration of Eq.(2.6), after separation of variables, using Eq.(2.7) and the boundary condition that the number of subcritical nuclei equals N' at $t=0$, it is obtained for the rate of formation of supercritical nuclei at $t=\tau$:

$$\dot{N}(T) = -\dot{N}_{sub} = \lambda N' \exp\left(-\int_0^\tau \lambda dt\right). \quad (2.5d)$$

By variation of λ_0 the mode of nucleation can be varied from site saturation (λ_0 infinitely large) to continuous nucleation (λ_0 infinitely small).

2.3.2 Growth models

Two (extreme) growth models are considered; one for volume diffusion controlled growth and one for interface controlled growth. Volume diffusion controlled growth can occur upon phase transformations where long range compositional changes take place. The case of interface controlled growth can occur in the absence of compositional changes, e.g. in cases of allotropic phase transformations.

2.3.2.1 Diffusion controlled growth.

In this case, long distance diffusion in the matrix governs the growth of the new phase particles. A characteristic diffusion length, L , is in the isothermal case given by

$$L = (Dt)^{1/2}, \quad (2.8a)$$

where D is the diffusion coefficient. The squared diffusion length is proportional to the time. This leads to so-called parabolic growth laws for phase transformations. For non-isothermal annealing the characteristic diffusion length is accordingly given by (e.g. see Ref.[14]):

$$L = \left(\int D(T(t))dt\right)^{1/2}. \quad (2.8b)$$

The diffusion coefficient depends on temperature according to:

$$D(T(t)) = D_0 \exp\left(-\frac{Q_D}{RT}\right), \quad (2.9)$$

with D_0 as the pre-exponential factor and Q_D as the activation energy for diffusion.

Growth laws corresponding to Eqs.(2.8a,b) are only valid for growth of a second phase particle into an infinitely large parent phase matrix, and thereby application of such growth

laws is strictly valid only for initial stages of transformation (see also Ref.[15]).

If Eqs.(2.8a,b) hold, the volume of the growing particle, Y , is given by:

$$Y = gL^d, \quad (2.10)$$

with d as the number of dimensions in which the particle grows and g as a particle-geometry factor.

2.3.2.2 Interface controlled growth.

In this case, processes at the particle/matrix interface govern the growth of the new phase particle. The velocity of the particle/matrix interface is determined by the net number of atoms that jump through the interface from the matrix to the new phase particle per unit of time. The Gibbs energy of an atom in the new phase differs an amount ΔG with the Gibbs energy in the parent phase (ΔG is the driving force for the phase transformation; i.e. $\Delta G < 0$). The transfer of this atom is however frustrated by the interface, which forms an energy barrier. The Gibbs energy of an atom in the interface differs an amount ΔG^a with the Gibbs energy in the matrix (i.e. $\Delta G^a > 0$).

The net flux of atoms from the parent phase to the new phase particle is the difference between the flux of atoms from the matrix to the particle and the flux of atoms from the particle to the matrix. The flux of atoms in one direction can be given by an Arrhenius equation with the corresponding Gibbs energy barrier as the activation energy. If the pre-exponential factors for both fluxes are equal, the net flux for growth, J , can be given as [2]:

$$J \propto \exp\left(-\frac{\Delta G^a}{RT}\right) - \exp\left(-\frac{\Delta G^a + \Delta G}{RT}\right) = \exp\left(-\frac{\Delta G^a}{RT}\right) \left(1 - \exp\left(-\frac{\Delta G}{RT}\right)\right). \quad (2.11)$$

If the driving force ΔG is large as compared to RT , as for large undercooling or overheating, then it follows for the net flux:

$$J \propto \exp\left(-\frac{\Delta G^a}{RT}\right) \quad (2.12)$$

The flux, J , is proportional to the interface velocity, j , and therefore the volume of a growing particle, Y , is given by:

$$Y = g \left(\int j dt \right)^d$$

$$j = j_0 \exp\left(-\frac{\Delta G^a}{RT}\right), \quad (2.13)$$

where j_0 is a pre-exponential factor.

2.3.2.3 Diffusion controlled growth and interface controlled growth

Both growth models, diffusion controlled growth and interface controlled growth, represented

by Eqs.(2.10) and (2.13), can be given in a compact form. At time t , the volume, Y , of a particle nucleated at time τ is given by:

$$Y = g \left(\int_{\tau}^t v dt \right)^{\frac{d}{m}}, \quad (2.14)$$

$$v = v_0 \exp \left(-\frac{Q_g}{RT} \right),$$

with v_0 as the pre-exponential factor for growth, Q_g the activation energy for growth, and m as the growth mode parameter. For the case of diffusion controlled growth, $m=2$, Q_g equals Q_D (activation energy for diffusion) and v_0 equals D_0 . For the case of interface controlled growth $m=1$, Q_g equals ΔG^a (interface energy barrier) and v_0 equals j_0 .

2.3.3 Impingement of growing particles; the total degree of transformation

The number of (supercritical) nuclei formed in a unit volume, at time τ during a time lapse $d\tau$ is given by $\dot{N}(T(\tau))d\tau$ with $\dot{N}(T(\tau))$ according to Eqs.(2.5). The volume of each of these nuclei grows from τ until t according to Eq.(2.14), where it is supposed that every particle grows into an infinitely large parent phase, in the absence of other growing particles (see discussion below Eq.(2.9)). The volume of all particles at time t , according to this treatment is then given by:

$$V_e = \int_0^t V \dot{N} Y d\tau, \quad (2.15)$$

with V as the total volume of the system, which is supposed to be constant throughout the transformation. This result, V_e , is called the extended volume. Clearly, in reality, the particles are not growing into an infinitely large parent phase: V_e does not account for the overlap of particles (hard impingement) and their possibly surrounding diffusion fields (soft impingement). Therefore, the relationship between the extended volume V_e and the actual volume V^t of transformed phase is required.

It is supposed that the nuclei are dispersed randomly throughout the volume. Suppose that at time t the actually transformed volume is V^t . If the time is increased by dt , the extended and the actual transformed volumes will increase by dV_e and dV^t . From the change of the extended volume dV_e , only a part will contribute to the change of the actually transformed volume dV^t , namely a part as large as the untransformed volume fraction $(V-V^t)/V$. Hence,

$$dV^t = \left(\frac{V - V^t}{V} \right) dV_e. \quad (2.16)$$

This equation can be integrated, giving the degree of transformation, f , as:

$$f \equiv \frac{V'}{V} = 1 - \exp\left(-\frac{V_e}{V}\right). \quad (2.17)$$

2.3.4 Summary of main assumptions

For the above treated nucleation and growth models, some assumptions have been made.

It has been assumed, (i) in both the continuous nucleation model (section 2.3.1.1) and in the interface controlled growth model (section 2.3.2.2) that the undercooling, or the overheating is large, in order to obtain an Arrhenius temperature dependence for the continuous nucleation and growth rates. In the literature the use of an Arrhenius-like temperature dependence for both the nucleation rate, and for the growth rate has been assumed several times, without motivation (e.g. see Refs.[10, 12, 13, 16]). It should be recognised that such a description of the growth rate and especially the nucleation rate is problematic if the undercooling is small [17, 18]. Experimental proof of Arrhenius temperature dependence of both the nucleation rate and the growth rate has been obtained for the crystallisation of metallic glasses [19].

In the impingement treatment, it has been assumed that (ii) the nuclei are dispersed randomly in space and (iii) that the specific volume is constant throughout the transformation. The assumption of randomly dispersed nuclei is justified in the case of homogeneous nucleation, and in the case of heterogeneous nucleation if the nucleation takes place on randomly dispersed nucleation sites, as with clustering of solute atoms or crystallisation of a glass. The assumption of constant specific volume is an approximation for almost all transformations, which is justified as long as the change of the specific volume is small.

2.4 Validity of Johnson-Mehl-Avrami description

The general recipe for deriving an explicit analytical formulation for the degree of transformation in terms of the nucleation and growth mechanisms is as follows. The extended volume is calculated according to Eq.(2.15), using the appropriate nucleation (Eqs.(2.5)) and growth models (Eq.(2.14)). The expression for the extended volume is then substituted into Eq.(2.17) to give the degree of transformation.

2.4.1 Isothermal annealing

If the above recipe is applied to isothermal transformations using for nucleation, either the continuous nucleation model or the site saturation model and for growth the general model (Eq.(2.14)), pertaining to either volume diffusion controlled growth or interface controlled

growth, it is straightforwardly obtained:

$$f = 1 - \exp\left(-\left(k(T)t\right)^n\right), \quad (2.18)$$

with $k(T)$ as the rate constant given in Eq.(2.3) with constant T , and n as a constant. Note that this equation cannot be derived for a mixture of the nucleation models (cf. section 2.3.1.3). Equation (2.18) has first been derived by Johnson and Mehl (for the case of isothermal transformations with continuous nucleation [5] and by Avrami (for isothermal transformations with continuous nucleation and site saturation) [6-8] and therefore it is called the JMA equation with JMA exponent n .

The above formulation of JMA kinetics is compatible with the identification of the variable β as described by Eq.(2.4): function F from Eq.(2.1) in this case becomes:

$$F(\beta) = 1 - \exp(-\beta^n). \quad (2.19)$$

The prescription of Eq.(2.1) implies that the equations describing the degree of transformation are identical for the cases of isothermal annealing and non-isothermal annealing *if they are expressed in terms of β* (see Eqs.(2.2) and (2.4)).

2.4.2 Isothermal annealing versus non-isothermal annealing

It has been shown above that for isothermal annealing definition of β according to Eq.(2.4) leads to the recognition that the JMA equation satisfies Eq.(2.1). Now the question arises if for non-isothermal annealing, on the basis of the considered nucleation and growth models, (i) an equation for V_e can be derived (from Eq.(2.15)) that after substitution into Eq.(2.17) leads to a JMA-like equation that (ii) fulfils the prescription of Eq.(2.1) with β defined according to Eq.(2.2). Additionally, if a JMA-like equation can be obtained, the associated kinetic parameters n , Q and k_0 can be given in terms of the various nucleation and growth models for the case of non-isothermal annealing too. In the following, it will be shown that this is possible for, at least, the case of isochronal annealing as long as the nucleation process involved is either site saturation or continuous nucleation.

2.4.3 Isochronal annealing

The recipe for deriving an equation for the degree of transformation given in the beginning of section 2.4 can be used in general. Now this recipe is applied to the case of isochronal annealing characterised by:

$$T(t) = T_0 + \Phi t, \quad (2.20)$$

where T_0 is the start temperature (i.e. at $t=0$) of the experiment and Φ is the constant heating

rate. Although the treatment is analogous to that for isothermal transformations, some mathematical problems now occur. The integrals in Eqs.(2.14) and (2.15) cannot be evaluated analytically in general, and also not for cases of only site saturation or only continuous nucleation. An Arrhenius term, as for example obtained by substitution of Eqs.(2.3) and (2.20) into Eq.(2.2), has to be integrated over time as follows:

$$\beta = k_0 \int_0^t \exp\left(-\frac{Q}{R(T_0 + \Phi t)}\right) dt, \quad (2.21)$$

The integral in Eq.(2.21) is also called the temperature integral [9] if it is integrated over the temperature, with the time dependent on temperature (i.e. $t=(T-T_0)/\Phi$). Here, the integration is performed over a new time parameter $t'=t+T_0/\Phi$, involving $dt=dt'$ and $T_0+\Phi t=\Phi t'=T(t')$. The boundaries for the integration then become T_0/Φ and t' . If on heating T_0 is chosen small, such that $\beta(T<T_0)\approx 0$, the start of the new time scale (i.e. $t'=T_0/\Phi$) can be shifted to $t'=0$ without changing the value of the integral [20]:

$$\beta = k_0 \int_{\frac{T_0}{\Phi}}^{t'} \exp\left(-\frac{Q}{R\Phi t'}\right) dt' \approx k_0 \int_0^{t'} \exp\left(-\frac{Q}{R\Phi t'}\right) dt'. \quad (2.22)$$

Thus, an analytical approximation of the integral becomes possible, using a series expansion of the following type [21]:

$$\int_1^{\infty} \frac{e^{-xt}}{t^n} dt = \frac{e^{-x}}{x} \left[1 - \frac{n}{x} + \frac{n(n+1)}{x^2} + \dots \right]. \quad (2.23)$$

Application of Eq.(2.23) requires variable substitution as described in [9]. An example of the result of this approximation is given here for β as expressed by Eq.(2.22):

$$\beta \approx k_0 \int_0^{t'} \exp\left(-\frac{Q}{R\Phi t'}\right) dt' \approx \frac{k_0 \Phi R t'^2}{Q} \exp\left(-\frac{Q}{R\Phi t'}\right) \left[1 - 2 \frac{R\Phi t'}{Q} + 6 \left(\frac{R\Phi t'}{Q}\right)^2 - \dots \right]_0^{t'} \quad (2.24)$$

For practical use (see below Eq.(2.27)), the back substitution $t'=T(t')/\Phi$ is made, and thus none of the time parameters (t or t') is involved anymore. On basis of Eq.(2.24), explicit analytical equations can be derived for the degree of transformation in the case of isochronal annealing, and for specific nucleation and growth models following the recipe indicated at the beginning of section 2.4: see Appendix A. In general, (e.g. for a mixture of nucleation mechanisms (cf. section 2.3.1.3)) the derivations do *not* lead to JMA-like equations for the degree of transformation. However, for pure site saturation (section 2.3.1.2) and for pure continuous nucleation (section 2.3.1.1), both in combination with growth according to Eq.(2.14), JMA-like equations are obtained that are compatible with Eq.(2.1) with β as given by Eq.(2.2) and k

as given by Eq.(2.3).

The case of a mixture of nucleation mechanisms (cf. section 2.3.1.3)), in combination with growth, is considered separately: see section 2.6.

The above treatment leads to explicit expressions for n , Q and k_0 in terms of the operating nucleation and growth mechanisms: see Table 2.1.

Table 2.1: Expressions for n , Q , and k_0 in terms of nucleation and growth mechanisms. The nucleation model parameters given are the pre-exponential factor N_0 , activation energy Q_N (continuous nucleation, cf. Eq.(2.5a)) or the number of nuclei N^* (site saturation cf. Eq.(2.5b)). The growth model parameters are the pre-exponential factor v_0 and the activation energy Q_g for growth, dimensionality of growth d , a geometrical factor g and the growth mode parameter m (cf. Eq.(2.14)). The parameter s is a correction factor for the difference between the activation energies of nucleation and growth, specified by Eq.(A.17).

Continuous Nucleation	Isothermal	Isochronal
n	$\frac{d}{m} + 1$	$\frac{d}{m} + 1^*$
Q	$\frac{(n-1)Q_g + Q_N}{n}$	$\frac{(n-1)Q_g + Q_N^*}{n}$
k_0	$\sqrt[n]{\frac{gN_0v_0^{n-1}}{n}}$	$\sqrt[n]{\frac{gN_0v_0^{n-1}s^*}{n}}$
Site saturation		
n	$\frac{d}{m}$	$\frac{d}{m}$
Q	Q_g	Q_g
k_0	$\sqrt[n]{gN^*v_0^n}$	$\sqrt[n]{gN^*v_0^n}$

*Only possible to proof analytically for d/m having an integer value

It is striking to observe that, for the nucleation and growth cases considered, the JMA parameters pertaining to isothermal annealing and to isochronal annealing are equal (except for the correction factor s). Two related treatments regarding this type of kinetic analysis have been published before. The oldest work is incomplete (Ref.[10]: no expression for s (cf. Table 2.1) is given, and diffusional growth is not considered), whereas the more extended, recent work [12] is erroneous. In Ref.[12] equations for β^n have been interpreted according to $\beta^n = kt^n$ for both isothermal and isochronal annealing, whereas Eq.(2.2) and Eq.(2.3) should have been used for non-isothermal (isochronal) annealing. Then, the conclusion in Ref.[12] that the

kinetic parameters for isochronal and isothermal annealing are not equal is obvious in view of the assumption made, but unjustified. If the kinetic descriptions used for isothermal and non-isothermal transformations are compatible, as in this work, then the kinetic parameters for isothermal and for non-isothermal annealing are equal, as is shown in Table 2.1, for the cases considered.

2.4.4 General representation of the overall activation energy; mixture of nucleation mechanisms

The expressions for the overall, effective activation energy, Q , given in Table 2.1 can be represented by a single equation, incorporating the exponent n , the ratio of the number of growth dimensions and the growth mode, d/m , and the separate activation energies for nucleation, Q_N , and for growth, Q_g , as follows:

$$Q = \frac{\frac{d}{m} Q_g + (n - \frac{d}{m}) Q_N}{n}, \quad (2.25)$$

where n has the value $\frac{d}{m}$ in the case of site saturation and $\frac{d}{m} + 1$ in the case of continuous nucleation. Eq.(2.25) pertains to both isothermal and non-isothermal annealing. For the case of isothermal annealing an equation similar to Eq.(2.25) has been given in Refs.[13, 16]. Eq.(2.25) demonstrates that, for the cases considered, the effective activation energy Q can be conceived as a weighted sum of the activation energies for nucleation and growth, with $\frac{d}{nm}$ and $(n - \frac{d}{m})/n$ as weighing factors. It is suggested here (and this will be verified: section 2.6) that this equation has a more general validity, and thus it may be applied to cases where a mixture of nucleation mechanisms occurs. No JMA-like equations can be derived for such cases (see section 2.6), and thus exact explicit analytical expressions for Q cannot be given.

2.5 Determination of kinetic parameters

In order to evaluate the kinetics of a transformation, measurements have to be performed from which the transformed fraction as a function of time and temperature can be obtained. By adopting a certain function $f=F(\beta)$ (Eq.(2.1)), which describes the relation between the path variable β and the transformed fraction, f , it is possible to calculate β as a function of time/temperature from the measurement.

If JMA kinetics occurs, the function F is given by Eq.(2.19). Then, if values for the transformed fraction are known from measurements, the corresponding values of β^n are also known. The kinetic parameters n , Q and k_0 , can then be determined from the β^n data as follows.

For isothermal annealing it holds (cf. Eq.(2.4)):

$$\beta^n = (k(T)t)^n. \quad (2.26)$$

Both parameters $k(T)$ and n can be determined from one isothermal experiment (i.e. measuring the progress of the transformation as a function of time at a constant temperature) comprising at least two data points (t, β^n) . Determination of Q and k_0 , incorporated in $k(T)$ according to Eq.(2.3), requires at least two such isothermal experiments, each at a different temperature.

For isochronal annealing it holds (cf. Eq.(2.24)):

$$\beta^n \approx \left(\frac{k_0 \Phi R t'^2}{Q} e^{\left(\frac{Q}{R \Phi t'} \right)} \right)^n. \quad (2.27)$$

In practical cases, β^n is measured as a function of temperature T . In order to obtain an equation compatible with this measurement, back substitution of t' by T/Φ in the right hand side of Eq.(2.27) is often performed (see below Eq.(2.21)).

In principle, values of n , Q and k_0 can be obtained from one isochronal experiment (i.e. measuring the progress of the transformation as a function of time/temperature at a constant heating rate) comprising at least three data points (t', β^n) . Substituting these three (t', β^n) pairs in Eq.(2.27), leads to a system of three equations with the three unknowns, k_0 , Q and n . A unique analytical solution for this system of equations does exist, but, upon testing this method in practice, it was observed that the values thus obtained for the kinetic parameters appeared to be extremely sensitive to small changes in the values of the measured data (t', β^n) , rendering the results obtained in this way practically meaningless. Therefore, in practice, at least two isochronal heating experiments, with different heating rates Φ , are required.

It should be noted that (only) the value for the overall, effective activation energy can be determined without recourse to a specific kinetic model; see discussion in Ref.[9].

The accuracy of the determination of the kinetic parameters can be increased by choosing the temperature-time program parameters (Φ (isochronal experiments) or T (isothermal experiments)) far apart, but this is bound to practical limits.

2.6 Determination and interpretation of kinetic parameters; practical limits in the use of the JMA description

If one attempts to describe the kinetics as observed in practice with JMA-like equations, one very often obtains values for the JMA exponent which cannot be interpreted directly on the

basis of Table 2.1: the value of the JMA exponent appears to be between the JMA exponent expected for site saturation and the JMA exponent expected for continuous nucleation. In these cases, it may be deduced that the actual nucleation is of ‘intermediate’ nature. However, a JMA description is in principle not applicable to cases where a mixture of nucleation mechanisms operates (see section 2.4.3). This has not always been realised, for example see Refs.[22, 23]. Nevertheless, it is worthwhile to investigate the (extent of) applicability of JMA for cases of intermediate nucleation too. Further, knowledge about the validity of Eq.(2.25), suggested to be of general applicability in section 2.4.4, is desired.

2.6.1 Exact vs. JMA kinetics; the effective activation energy

As explained before (section 2.4.3), analytical results cannot be derived for an arbitrary combination of the nucleation and growth models and therefore the recipe at the beginning of section 2.4 is used for *numerical* calculation of the transformed fraction. Then JMA kinetics is fitted to this transformed fraction as function of time/temperature. Thereby the following steps are performed successively.

1. Values are chosen for the model parameters Q_g , v_0 and d/m (Eq.(2.14)) and Q_N (Eqs.(2.5d) and (2.5c)), and N_0 and N^* (Eq.(2.5c)) or λ_0 and N' (Eq.(2.5d)); i.e. a mixture of nucleation mechanisms is adopted.
2. Rigorous numerical application of the recipe given in the beginning of section 2.4 provides the transformed fraction f as a function of time/temperature. This calculation is performed for five different temperatures (isothermal annealing) or five different heating rates (isochronal annealing).
3. JMA kinetics, (i.e. Eq.(2.2) or (2.4), in combination with Eqs.(2.3) and (2.19)) is fitted to the transformed fraction as obtained in step 2 *simultaneously* for the five different temperatures (isothermal annealing) or the five different heating rates (isochronal annealing). Fitting is performed by minimisation of the sum of the squares of the residuals, employing a simplex fitting procedure [24]. Thus, values for the (JMA) kinetic parameters n , Q , and k_0 are obtained.

The above procedure has been performed for a range of values of N_0 and N^* (Eq.(2.5c)) or λ_0 (Eq.(2.5d)). Thus, the mode of transformation varies from pure site saturation to pure continuous nucleation. The values of the preset kinetic parameters have been gathered in Table 2.2. The applicability of JMA kinetics for the cases of intermediate nucleation can be judged from the goodness of the fits. The exponent n should vary from d/m (site saturation) to $d/m+1$ (continuous nucleation). The values obtained for the activation energy Q as a function

of exponent n can be considered to see if Eq.(2.25) holds for the cases of intermediate nucleation.

Table 2.2: Values of the kinetic parameters as used in the model calculations for isothermal and isochronal annealings for a case of mixture of nucleation mechanisms, Avrami nucleation according to Eq.(2.5d) and site saturation + continuous nucleation according to Eq.(2.5c), and the growth mechanisms pertaining to both (volume) diffusion and interface controlled growth, according to Eq.(2.14).

Avrami Nucleation				site saturation + continuous nucleation			
Q_g	(kJ/mol)	200		Q_g	(kJ/mol)	200	
v_0	(s ⁻¹)	1•10 ⁹		v_0	(s ⁻¹)	1•10 ⁹	
d/m		3		d/m		3	
Q_N	(kJ/mol)	100		Q_N	(kJ/mol)	100	
λ_0^{start}	(s ⁻¹)	1•10 ⁵	λ_0^{end}	(s ⁻¹)	1•10 ⁸	N_0^{start}	(s ⁻¹)
						5•10 ¹⁵	N_0^{end}
							5•10 ¹³
N'		5•10 ¹⁵		N^{start}		5•10 ⁸	N^{end}
							5•10 ¹⁰

The results of the exact numerical calculations of the kinetics and the fits of JMA kinetics are shown in Figs.2.2-2.5. In the upper part of the Figs. the transformed fraction as a function of time/temperature is shown for the case of the worst fit (the maximum in the middle part of the Figs.). The error in the fit is given in the middle part of the Figs. as a function of the fitted JMA exponent, i.e. the least squares difference between the exact calculated transformed fraction, $f(t)$, and the JMA fitted $f(t)$.

Clearly, the JMA description provides a reasonable fit, also in the cases where it does not hold in principle. Note that the calculations have been performed for a broad 'experimental' window in relation to the kinetic parameters. A temperature range of 50K has been used for the isothermal transformations, in which the transformation time varies over two decades. Five decades in heating rate have been used for isochronal annealing, in which the transformation temperature varies over a temperature range of 250 K.

The activation energy obtained by fitting has been plotted vs. the JMA exponent as obtained by fitting in Figs.2.2c-2.5c. In these figures, the predicted values of the activation energy according to Eq.(2.25) have also been shown. It can be concluded that Eq.(2.25) provides a very good description of the operating, effective activation energy (difference within 3%)

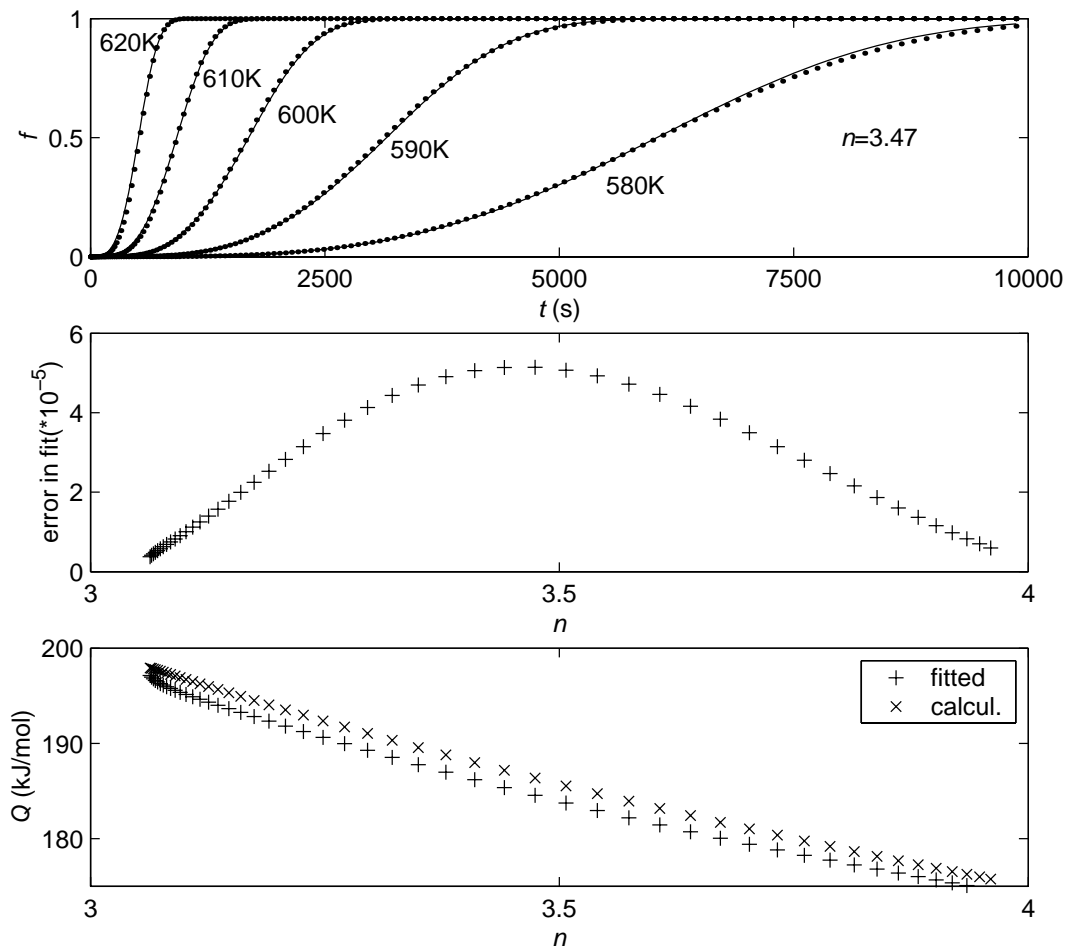


Fig.2.2a: Transformed fraction, f , against time, for five isothermal holding temperatures. The model calculations (\bullet) using Avrami nucleation and the JMA fit ($-$), for the maximum least squares difference between the transformed fraction according to the model calculations and the JMA fit, are shown. The parameter λ_0 has a value of $1.46 \cdot 10^6 \text{ s}^{-1}$.

Fig.2.2b: Least squares difference between the transformed fraction according to the model calculations and the fitted JMA kinetics, as a function of JMA exponent as determined in the fits.

Fig.2.2c: Activation energy as a function of fitted JMA exponent both according to Eq.(2.25) (\times), using the parameter prescriptions as given in Table 2.2, and according to the fits ($+$).

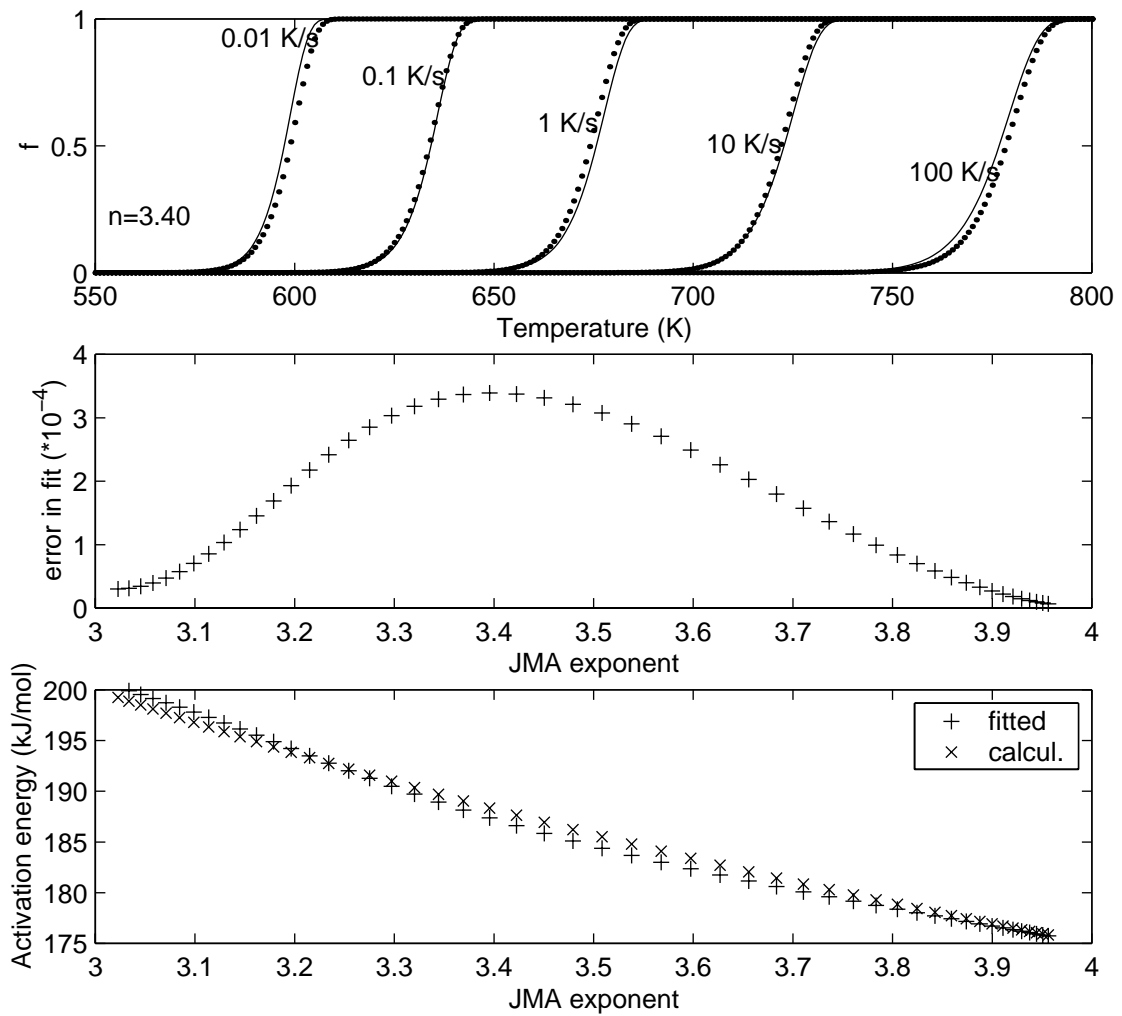


Fig.2.3a: Transformed fraction, f , against temperature, for five heating rates. The model calculations (\bullet) using Avrami nucleation and the JMA fit ($-$), for the maximum least squares difference between the transformed fraction according to the model calculations and the JMA fit, are shown. The parameter λ_0 has a value of $5.18 \cdot 10^6 \text{ s}^{-1}$.

Fig.2.3b: Least squares difference between the transformed fraction according to the model calculations and the fitted JMA kinetics, as a function of JMA exponent as determined in the fits.

Fig.2.3c: Activation energy as a function of fitted JMA exponent, both according to Eq.(2.25) (x), using the parameter prescriptions as given in Table 2.2 and according to the fits (+).

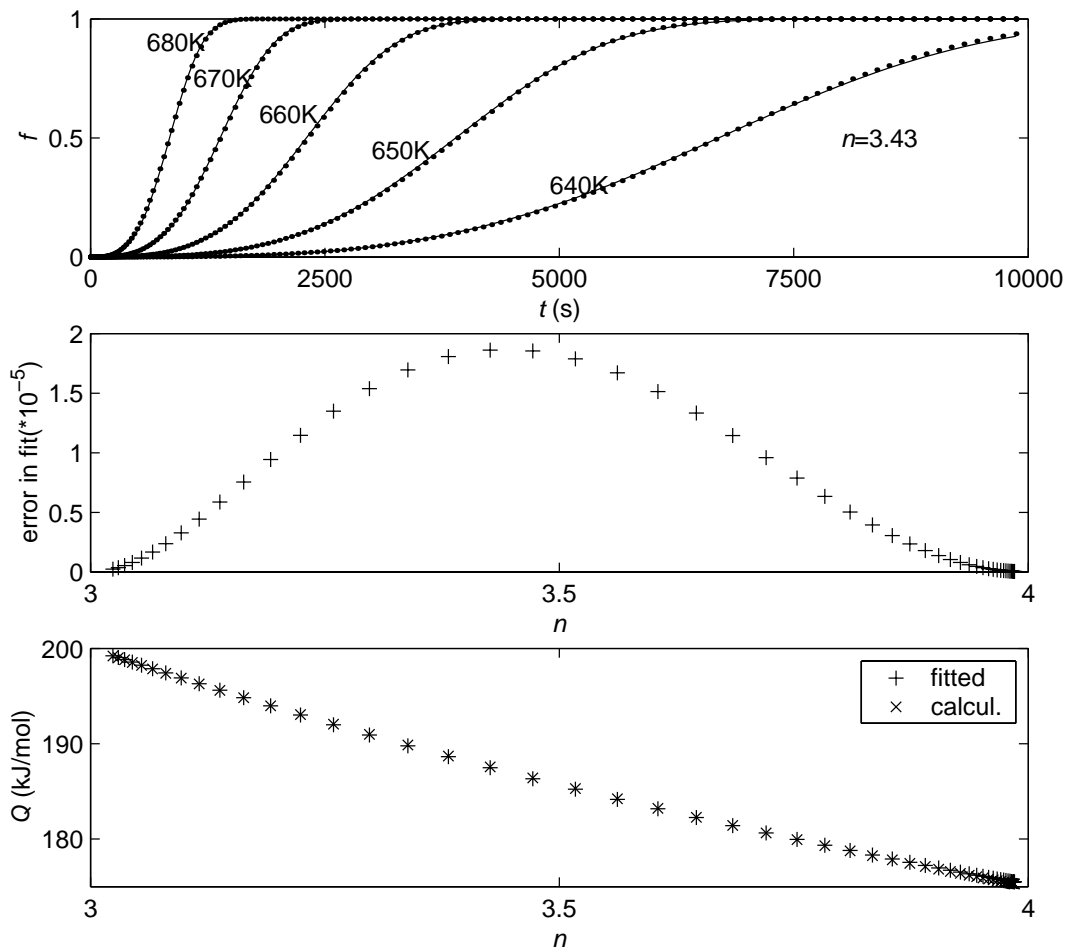


Fig.2.4a: Transformed fraction, f , against time, for five isothermal holding temperatures. The model calculations (\bullet) using the summation nucleation model and the JMA fit ($-$), for the maximum least squares difference between the transformed fraction according to the model calculations and the JMA fit, are shown. The mixing parameters from the nucleation model have the following values: $N^*=1.0 \cdot 10^{10} \text{ m}^{-3}$ and $N_0=2.5 \cdot 10^{14} \text{ s}^{-1} \text{ m}^{-3}$.

Fig.2.4b: Least squares difference between the transformed fraction according to the model calculations and the fitted JMA kinetics, as a function of JMA exponent as determined in the fits.

Fig.2.4c: Activation energy as a function of fitted JMA exponent, both according to Eq.(2.25) (\times), using the parameter prescriptions as given in Table 2.2 and according to the fits ($+$).

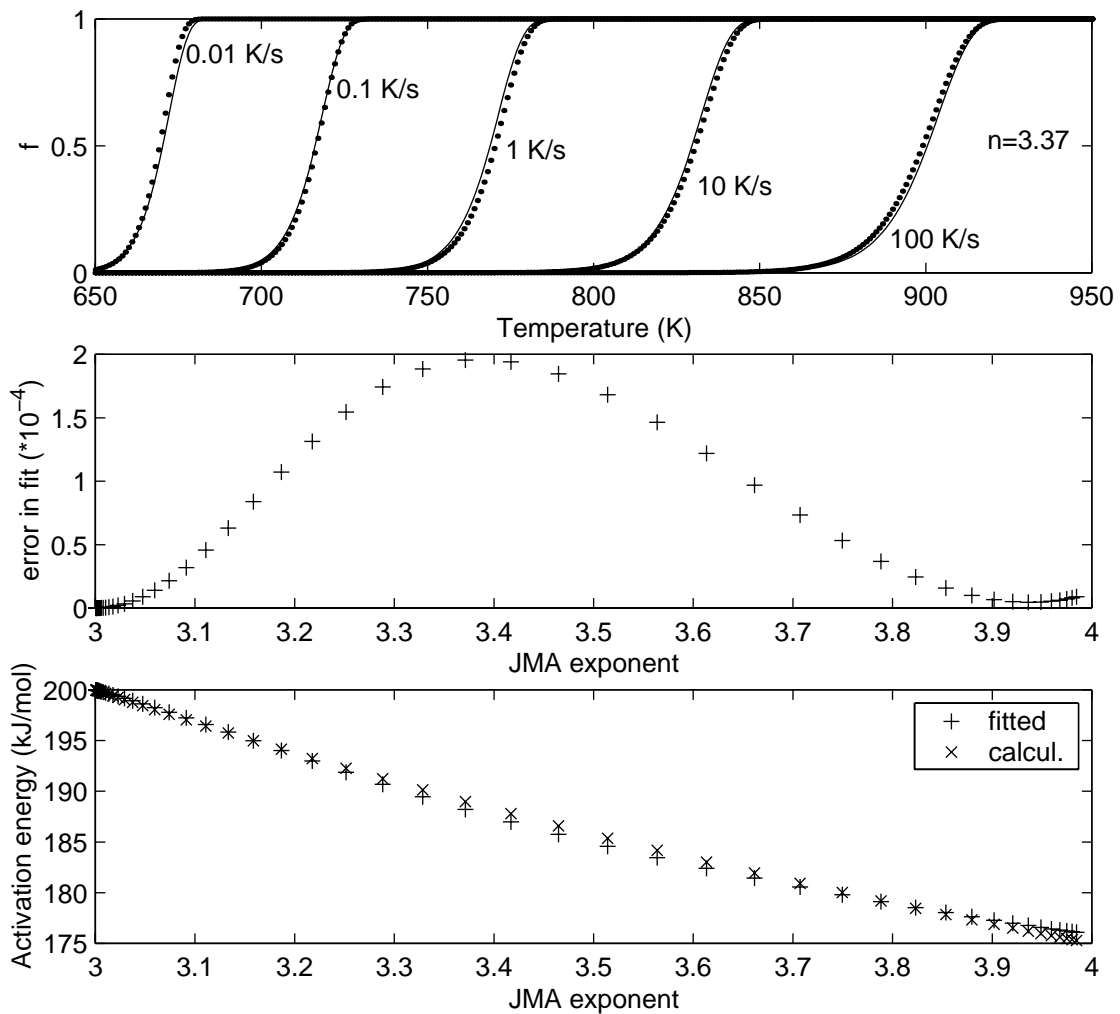


Fig.2.5a: Transformed fraction, f , against temperature, for five heating rates. The model calculations (\bullet) using the summation nucleation model and the JMA fit (—), for the maximum least squares difference between the transformed fraction according to the model calculations and the JMA fit, are shown. The mixing parameters for the nucleation model have the following values: $N^*=1.4\cdot 10^9 \text{ m}^{-3}$ and $N_0=3.5\cdot 10^{14} \text{ s}^{-1} \text{ m}^{-3}$.

Fig.2.5b: Least squares difference between the transformed fraction according to the model calculations and the fitted JMA kinetics, as a function of JMA exponent as determined in the fits.

Fig.2.5c: Activation energy as a function of fitted JMA exponent, both according to Eq.(2.25) (x), using the parameter prescriptions as given in Table 2.2 and according to the fits (+).

2.6.2 Determination of separate activation energies for nucleation and growth

The effective activation energy as a function of the JMA exponent can experimentally be determined if it is possible to vary the mode of the nucleation for the observed phase

transformation. From these data the separate activation energies for nucleation and growth can be determined using Eq.(2.25).

This case can be illustrated using several data points from the simulations dealt with in section 2.6.1. From Figs.2.2c-2.5c, the (n, Q) data points pertaining to the end points of the n range and the (n, Q) data point corresponding to Figs.2.2a-2.5a (i.e. the maximum in 2.2b-2.5b) have been used. Fitting of Eq.(2.25) to the three (n, Q) data points leads to values for the activation energies for nucleation and growth, given in Table 2.3 together with to corresponding exact values:

Table 2.3: The Activation energy for nucleation Q_N and the activation energy for growth Q_g as put in the model and determined by fitting Eq.(2.25) to three (n, Q) data points from the calculated cases considered in section 2.6.1. The value of d/m is taken 3.

	Q_N (kJ/mol)	Q_g (kJ/mol)
input (see Table 2.2)	100	200
Isothermal Avrami nucleation	97.7	198.9
Isochronal Avrami nucleation	97.1	200.4
Isothermal summation	100.9	199.9
Isochronal summation	103.9	199.5

Clearly, adoption of Eq.(2.25) leads to practically correct values of the activation energies for nucleation and growth for both isothermal and isochronal transformations.

2.6.3 Experimental example: crystallisation of bulk amorphous $Pd_{40}Cu_{30}P_{20}Ni_{10}$

The kinetics of the crystallisation of bulk amorphous $Pd_{40}Cu_{30}P_{20}Ni_{10}$ can be investigated on the basis of measurements performed in this project and as presented in Ref.[25]. Isothermal pre-annealing in the supercooled liquid temperature range has significant influence on the kinetics of the transformation (see Fig.2.6). Experimental details regarding specimen preparation and DSC analysis have been described in Ref.[25].

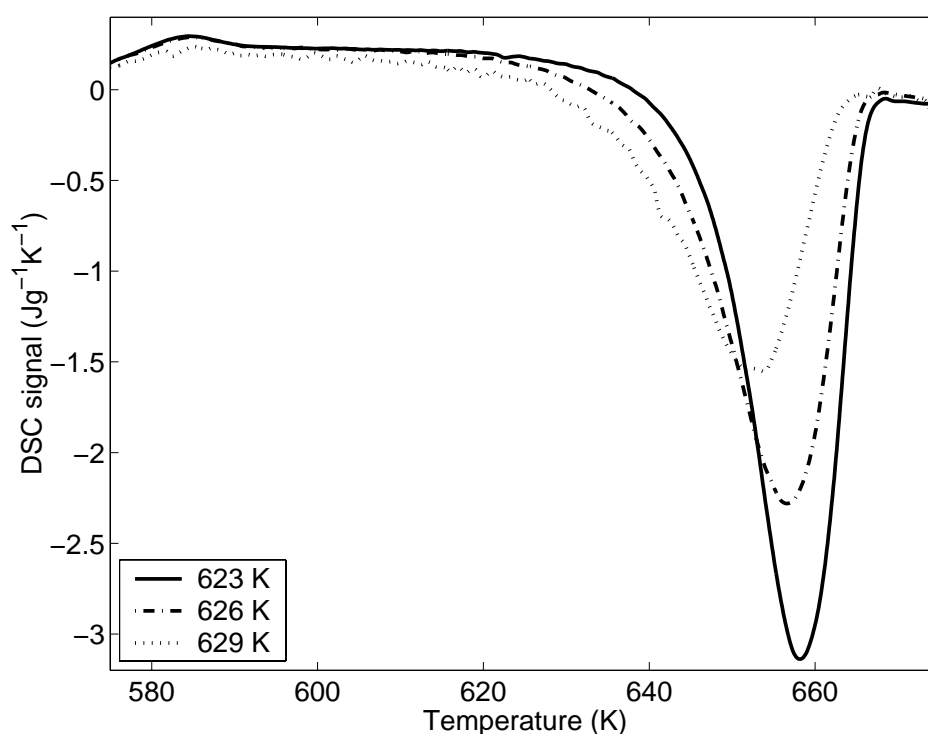


Fig.2.6: DSC scans for heating rate 20 K/min showing crystallisation behaviour of initially amorphous $\text{Pd}_{40}\text{Cu}_{30}\text{P}_{20}\text{Ni}_{10}$. Results are shown as obtained after different pre-annealing heat treatments of 600 s at the temperatures 623, 626 and 629 K.

The JMA kinetic parameters have been determined by fitting a JMA model to the measurements for 5 heating rates simultaneously. The values obtained for the kinetic parameters of the transformation have been given in Table 2.4.

Table 2.4: The JMA exponent n and the effective activation energy Q for isochronal crystallisation of amorphous $\text{Pd}_{40}\text{Cu}_{30}\text{P}_{20}\text{Ni}_{10}$ as determined by fitting.

pre annealing temperature (K)	n	Q (kJ mol ⁻¹)
623	2.44	292
625	2.04	304
626	2.01	300
628	1.71	307
629	1.55	317

This transformation involves three-dimensional diffusional growth and the pre-annealing has no influence on the growth mechanism [25]. Thus d/m has the constant value $3/2$. According

to the theoretical treatment (see section 2.4.4), the value of n can vary between d/m ($3/2$) in the case of site saturation and $d/m+1$ ($5/2$) in the case of continuous nucleation.

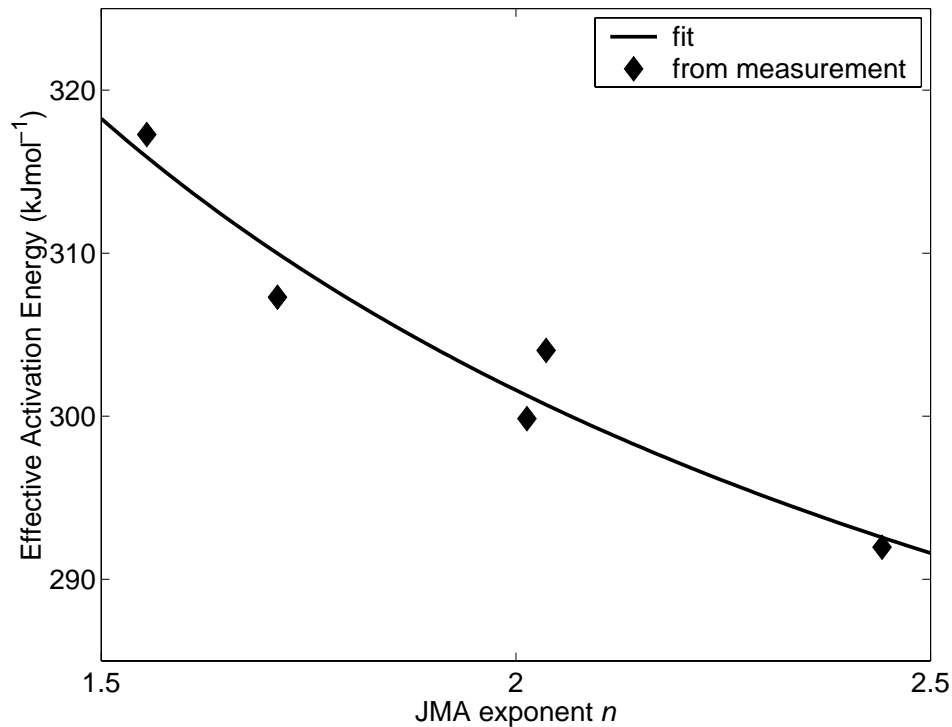


Fig.2.7 The effective activation energy, Q , as a function of JMA exponent, n , as measured (\blacklozenge) and as fitted according to Eq.(2.25) (full line) using $d/m=3/2$.

Eq.(2.25) can be fitted to the 5 data points gathered in Table 2.4, corresponding to the 5 different pre-anneals, leading to determination of values for the separate activation energies for nucleation and growth (section 2.6.2). The activation energy for nucleation is found to be 252 kJ/mol and the activation energy for growth is found to be 318 kJ/mol; see also Fig.2.7. The value of the activation energy for nucleation as determined here is within the range of activation energies for nucleation for metal-metalloid glasses ($\text{Co}_{70}\text{B}_{30}$: 191 kJ/mol, $\text{Fe}_{65}\text{Ni}_{10}\text{B}_{25}$: 300 kJ/mol [26]). The value of the activation energy for diffusion as determined here (318 kJ/mol) is low in comparison to the activation energy for Au diffusion in amorphous $\text{Pd}_{40}\text{Ni}_{40}\text{P}_{20}$ (420 kJ/mol) [27] and is high in comparison to the values for self diffusion in the crystalline constituents: Pd 266 kJ/mol, Cu 209 kJ/mol and Ni 285 kJ/mol [28], which is reasonable.

2.7 Conclusions

(i) Both for isothermal and non-isothermal transformations the degree of transformation is uniquely described by the path variable β (Eq.(2.1)), which is given, independent of the

time-temperature program, by Eqs.(2.2) and (2.3). The Johnson-Mehl-Avrami (JMA) equation is compatible with this concept: there is one JMA equation for both isothermal and non-isothermal transformations only if expressed in terms of β (Eq.(2.19)).

(ii) The JMA equation (transformed fraction, f , as function of β) holds only for specific, extreme cases of nucleation: pure site saturation or pure continuous nucleation. For general phase transformations, in particular if a mixture of nucleation mechanisms, in association with diffusion or interface controlled growth mechanisms, occurs, JMA kinetics does not hold in principle. However, the JMA equation can provide a good description of the reaction kinetics also in such cases as demonstrated by the model simulations.

(iii) The values for the JMA kinetics parameters are equal for isothermally and isochronally conducted phase transformations, in contrast with earlier published results.

(iv) The effective activation energy can be given for very many transformations as a weighted sum of the separate activation energies for nucleation and growth, with the weights d/mn for growth and $1-d/mn$ for nucleation, where d is the dimensionality of the growth, n is the JMA exponent and m depends on the growth mode: $m=1$ for interface controlled growth, and $m=2$ for diffusion controlled growth (Eq.(2.25)). This result allows determination of the separate activation energies for nucleation and growth by varying the mode of nucleation for a phase transformation, e.g. by pre-annealing.

Appendix A: Calculating the kinetic parameters analytically

A.1 Site Saturation

The extended volume of N^* particles growing from time 0 until time t is given by:

$$V^e = VN^* g \left(\int_0^t v_0 \exp\left(-\frac{Q_g}{RT(t)}\right) dt \right)^{\frac{d}{m}}, \quad (\text{A.1})$$

with the parameters as given under Eq.(2.14) and (2.15). This Eq.(A.1) is in the same form as JMA kinetics (see Eqs.(2.2), (2.3) and (2.19)):

$$V^e = V \left(\int_0^t k_0 \exp\left(-\frac{Q}{RT(t)}\right) dt \right)^n. \quad (\text{A.2})$$

If it now is considered that k_0 and n from Eq.(A.2) and v_0 , N^* , g , d and m from Eq.(A.1) are independent of time, it can be shown that:

$$V^e = V k_0^n \left(\int_0^t \exp\left(-\frac{Q}{RT(t)}\right) dt \right)^n = VN^* g v_0^{\frac{d}{m}} \left(\int_0^t \exp\left(-\frac{Q_g}{RT(t)}\right) dt \right)^{\frac{d}{m}}, \quad (\text{A.3})$$

and, from Eq.(A.3), the JMA parameters can be given in terms of nucleation and growth:

$$\begin{aligned} n &= \frac{d}{m} \\ Q &= Q_g \\ k_0 &= (N^* v_0^n g)^{\frac{1}{n}} \end{aligned} \quad (\text{A.4})$$

These values for the JMA parameters do not depend on the time temperature program and, as shown, can be derived without any mathematical assumptions.

A.2 Continuous Nucleation during Isothermal annealing

The extended volume from a ‘Continuous Nucleation’ process as described can be given by:

$$V^e = V \int_0^t g N_0 \exp\left(-\frac{Q_N}{RT}\right) \left(\int_{\tau}^t v_0 \exp\left(-\frac{Q_g}{RT}\right) dt \right)^{\frac{d}{m}} d\tau, \quad (\text{A.5})$$

with the same parameters as in Eq.(A.1), apart from N_0 which is the pre-exponential factor for nucleation, and Q_N is the activation energy for nucleation.

If the isothermal case is considered, it can be shown that:

$$V^e = V \int_0^t g N_0 v_0^{\frac{d}{m}} \exp\left(-\frac{Q_N}{RT}\right) \exp\left(-\frac{d}{m} \frac{Q_g}{RT}\right) (t-\tau)^{\frac{d}{m}} d\tau, \quad (\text{A.6})$$

which in turn can be integrated, and be equated to the integrated version of Eq.(A.2) to give:

$$V^e = V k_0^n \exp\left(-\frac{nQ}{RT}\right) t^n = V g \frac{1}{\frac{d}{m} + 1} N_0 v_0^{\frac{d}{m}} \exp\left(-\frac{\frac{d}{m} Q_g + Q_N}{RT}\right) t^{\left(\frac{d}{m} + 1\right)}, \quad (\text{A.7})$$

and thus, the JMA parameters can be given by:

$$\begin{aligned} n &= \frac{d}{m} + 1 \\ Q &= \frac{(n-1)Q_g + Q_N}{n} \\ k_0 &= \left(N_0 v_0^{n-1} \frac{g}{n}\right)^{\frac{1}{n}} \end{aligned} \quad (\text{A.8})$$

A.3 Continuous Nucleation during Isochronal annealing

During isochronal annealing, the temperature depends on time as is shown in Eq.(2.20). If this equation is combined with Eq.(A.2), it is impossible to integrate the resulting equations without any mathematical assumptions.

By using the mathematical assumption (Eq.(2.24)) twice, once for the inner integral in Eq.(A.5), and once for the outer integral in Eq.(A.5), it is possible to perform the integration. The inner integral can be written as:

$$\begin{aligned} \int_{\tau}^{t'} v_0 \exp\left(-\frac{Q_g}{R\Phi t'}\right) dt' &= v_0 \left(f\left(\frac{R\Phi t'}{Q_g}\right) - f\left(\frac{R\Phi \tau}{Q_g}\right)\right) \\ f\left(\frac{R\Phi t'}{Q_g}\right) &= \left(\frac{R\Phi t'}{Q_g}\right)^2 \exp\left(-\frac{Q_g}{R\Phi t'}\right) \left[1 - 2\frac{R\Phi t'}{Q_g}\right] \end{aligned} \quad (\text{A.9})$$

Now filling this out in equation (A.5) it follows:

$$\frac{V^e}{V} = \int_0^{t'} g N_0 \exp\left(-\frac{Q_N}{R\Phi t'}\right) \left(\int_{\tau}^{t'} v_0 \exp\left(-\frac{Q_g}{R\Phi t'}\right) dt'\right)^{\frac{d}{m}} d\tau = \int_0^{t'} g N_0 v_0^{\frac{d}{m}} \exp\left(-\frac{Q_N}{R\Phi t'}\right) \left(f\left(\frac{R\Phi t'}{Q_g}\right) - f\left(\frac{R\Phi \tau}{Q_g}\right)\right)^{\frac{d}{m}} d\tau \quad (\text{A.10})$$

This integration can be made using the same analytical approximation of the exponential in two terms, giving for the case of $d/m=1$:

$$\begin{aligned} \frac{V^e}{V} &\approx \frac{g}{2} v_0 N_0 C (R\Phi)^3 \exp\left(-\frac{Q_N + Q_g}{R\Phi t'}\right) t'^4 \\ C &= 2 \frac{Q_N^2 Q_g^2 + Q_N Q_g^3 - 6R\Phi t' Q_N Q_g^2 - 2R\Phi t' Q_g^3 - 6(R\Phi t')^2 Q_N^2 + 8(R\Phi t')^2 Q_N Q_g + 4(R\Phi t')^2 Q_g^2}{Q_g^2 Q_N^2 (Q_N + Q_g)^2} \\ &\approx \frac{2}{Q_N (Q_N + Q_g)} \end{aligned} \quad (\text{A.11})$$

By using only the first order series expansion twice during the calculation, it follows that:

$$\frac{V^e}{V} \approx \frac{g}{2} v_0 N_0 C (R\Phi)^3 \exp\left(-\frac{Q_N + Q_g}{R\Phi t'}\right) t'^4$$

$$C = \frac{2}{Q_N (Q_N + Q_g)}$$
(A.12)

If it now is considered that $R\Phi t' \ll Q$, which is the same assumption used for the termination of the analytical approximation series, it is seen that C is a constant, defined by the activation energies of nucleation and growth. It is also seen that the second order approximation is not needed in the integration, as the both assumptions will give the same result. Nevertheless, it is checked for the cases of $d/m=2$ and $d/m=3$ that the first and the second order approximation give the same result. It is seen, that the second order approximation is not needed in the calculation, and therefore, the first order approximation results are shown here.

For the cases of $d/m=2$ and $d/m=3$, first the case of $d/m=2$:

$$\frac{V^e}{V} = \frac{g}{3} N_0 v_0^2 C (R\Phi)^3 \exp\left(-\frac{Q_N + 2Q_g}{R\Phi t'}\right) t'^6$$

$$C = \frac{6}{Q_N (Q_N + Q_g) (Q_N + 2Q_g)}$$
(A.13)

And the case of $d/m=3$:

$$\frac{V^e}{V} = \frac{g}{4} N_0 v_0^3 C (R\Phi)^4 \exp\left(-\frac{Q_N + 3Q_g}{R\Phi t'}\right) t'^8$$

$$\approx \frac{24}{Q_N (Q_N + Q_g) (Q_N + 2Q_g) (Q_N + 3Q_g)}$$
(A.14)

In order to obtain the JMA kinetic parameters, equations (A.12),(A.13) and (A.14) are supposed to be identical to the JMA expression for V_e/V (Eq.(A.2)). For the comparison however, the same mathematical approximation is used for Eq.(A.2), also only developed in the first order:

$$\left(\int_0^{t'} k_0 \exp\left(-\frac{Q}{R\Phi t'}\right) dt' \right)^n \approx k_0^n \left(\frac{\Phi R}{Q}\right)^n \exp\left(-\frac{nQ}{R\Phi t'}\right) t'^{2n}$$
(A.15)

If it is now supposed that Eq.(A.15) equals Eqs.(A.12),(A.13) and (A.14) respectively, then the values for the JMA kinetic parameters are given by:

$$n = \frac{d}{m} + 1$$

$$Q = \frac{(n-1)Q_g + Q_N}{n}$$

$$k_0 = \left(N_0 v_0^{n-1} \frac{g}{n} C Q^n \right)^{\frac{1}{n}}$$
(A.16)

Now, in this equation, the value of CQ^n can be given in a more general form, which is proven to be correct for $n=2, 3$ and 4 :

$$s = CQ^n = \frac{(n-1)! (Q_N + (n-1)Q_g)^n}{n^{(n-1)} \prod_{j=0}^{j=n-1} (Q_N + jQ_g)}. \quad (\text{A.17})$$

This factor is a factor that corrects for a difference in activation energy for nucleation and growth.

To conclude, one can calculate symbolically the JMA parameters from Arrhenius nucleation and Arrhenius growth. The mathematical approximation to be made is used several times in the case of continuous nucleation on isochronal heating. The development of the exponential integral is used only in the first order approximation. This is correct in the case that $RT \ll Q$ for the used temperature and activation energy of interest. Usually, for solid-state phase transformations, this is the case.

The kinetic parameters n and Q obtained are exactly the same for the isochronal and isothermal annealing. The value of the pre-exponential factor k_0 however is not exactly the same in all cases.

3 The Isothermal and Isochronal Kinetics of the Crystallisation of Bulk Amorphous Pd₄₀Cu₃₀P₂₀Ni₁₀

A.T.W. Kempen, F. Sommer and E.J. Mittemeijer

Keywords: kinetics, activation energy, nucleation, growth, crystallisation, Johnson-Mehl-Avrami

Abstract

The amorphous alloy Pd₄₀Cu₃₀P₂₀Ni₁₀ has been produced by water quenching the molten alloy. The kinetics of crystallisation has been measured by means of isothermal and isochronal differential scanning calorimetry. The associated microstructural changes have been analysed using scanning electron microscopy. Special interest has been devoted to the influence of isothermal pre-annealing on subsequent isochronal crystallisation kinetics. By applying appropriate isothermal pre-annealing temperatures, nucleation of the crystalline phases takes place to different extents. Accordingly, the initial state for the subsequent isochronal crystallisation could be changed gradually with respect to the number of pre-existing nuclei. This leads to a gradual change of the mode of nucleation from site saturation to continuous nucleation during the crystallisation. The corresponding change of the kinetic parameters has been used to determine the activation energies of nucleation and growth separately.

3.1 Introduction

Metallic glasses often possess properties better than their crystalline counterparts. However, technological application of conventional metallic glasses is limited due to complications inherent to production and processing of the glass. Initial formation of the glass requires small specimen dimensions in order to assure high cooling rates upon quenching of the molten alloy leading to ribbon, powder, or film-like products. The forming needed to obtain a final product requires strict temperature control: if the forming is performed at elevated temperatures, crystallisation can take place.

Bulk amorphous alloys with much larger specimen dimensions than indicated above can be produced by optimisation of the alloy composition [29] and the production process [30]. Bulk amorphous Pd₄₀Cu₃₀P₂₀Ni₁₀ can for example be produced up to a diameter of 72 mm by quenching the molten alloy. This allows producing the amorphous alloy directly in a shape close to the required final product shape. Further, bulk amorphous glasses inherently possess a relatively high resistance against crystallisation, corresponding to a wide temperature range in which the alloy is in the undercooled liquid state. In this state, the viscosity is very low, thus enabling easy forming of the final product. In the case of bulk amorphous Pd₄₀Cu₃₀P₂₀Ni₁₀ it has for example been reported that forming of a product in the undercooled liquid state is possible without occurrence of crystallisation [31].

Hence, from a technological point of view, it is important for the development of such production routes to quantify the resistance against crystallisation of the undercooled liquid, in order to optimise process parameters. From a scientific point of view, the high resistance against crystallisation is advantageous because it enables unravelling of the two basic processes involved in crystallisation: nucleation and growth. By annealing at a temperature slightly below the crystallisation temperature, nucleation takes place abundantly. Subsequent complete crystallisation at higher temperature then is predominated by the growth of the existing nuclei. This method for the unravelling of the crystallisation kinetics is not practicable in rather unstable glasses, because crystallisation then probably takes place already substantially during the pre-annealing.

In the present work, the crystallisation kinetics of bulk amorphous Pd₄₀Cu₃₀P₂₀Ni₁₀ is investigated by isothermal and (subsequent) isochronal differential scanning calorimetry (DSC). Special attention is paid to the influence of isothermal pre-annealing in the undercooled liquid temperature region. The interpretation of the kinetic data obtained provides insight in processes causing structural change during isothermal holding in the

undercooled liquid state.

3.2 Transformation kinetics

In general, the progress of a phase transformation, defined as the fraction transformed f , depends on a path variable, β . This variable β is given by the integral of the temperature, T , dependent reaction rate constant, k , over time t [9, 32]:

$$\beta = \int k(T(t)) dt. \quad (3.1)$$

Note that the rate constant is considered not to depend on t other than through $T(t)$. The exact dependence of f on β , as well as the dependence of k on T , is prescribed by the specific kinetic model that is applied. For crystallisation of (metallic) glasses, Johnson-Mehl-Avrami (JMA) kinetics may provide a good description [32]. Then, the fraction transformed, f , depends on the path variable β through:

$$f = 1 - \exp(-\beta^n), \quad (3.2)$$

with n as the JMA exponent and the reaction rate constant is then given by:

$$k(T(t)) = k_0 \exp\left(-\frac{Q}{RT(t)}\right). \quad (3.3)$$

where k_0 is the pre-exponential factor, Q is the effective activation energy and R is the gas constant.

The parameter β^n is also called the extended transformed fraction [6-8, 32], x_e . This is the sum of the volumes of all (hypothetical) nucleated and grown grains, divided by the total specimen volume, assuming that the grains never stop growing (i.e. 'hard impingement' is ignored) and that new grains hypothetically nucleate also in the transformed material [33].

The formulation of the kinetic model as given in Eqs.(3.1)-(3.3) is valid for both isothermal and isochronal transformations [9, 32], and, as long as the transformation can be considered isokinetic [2, 34], the obtained JMA kinetic parameters k_0 , n and Q are independent of the temperature-time program.

3.2.1 Partial phase transformation

A phase transformation does not necessarily start at a transformed fraction equal to zero. For example, this is the case when a phase transformation has already taken place (for a small part) during a pre-annealing treatment, after which the partially transformed state has been quenched in. The subsequent rest-transformation in a second main-annealing treatment will then not start at $f=0$, but at $f_0>0$. For this main-annealing stage, the values of the kinetic

parameters are generally unequal to those valid for the pre-annealing stage. Therefore, in order to describe the transformation kinetics during the second main-annealing stage, the treatment starts with the relationship between f and the extended transformed fraction, x_e (see discussion below Eq.(3.3)). Hence, for the second annealing stage, the transformed fraction can then be given as (cf. Eq.(3.2))

$$f = 1 - \exp\left(-x_{e,0} - \int_{x_{e,0}}^{x_e} dx_e\right), \quad (3.4)$$

for $x_e > x_{e,0}$, where $x_{e,0}$ is the value of the extended transformed fraction, x_e , at the start of the main-annealing stage:

$$x_{e,0} = -\ln(1 - f_0). \quad (3.5)$$

and, where dx_e can be expressed as (cf. Eqs.(3.1) and(3.3)):

$$dx_e = d(\beta^n) = d\left[\left(\int k(T(t))dt\right)^n\right] = nk(T(t))\beta^{n-1}dt. \quad (3.6)$$

3.2.2 Interdependence of JMA kinetic parameters

Strictly speaking, the JMA kinetic parameters can only have certain values, pertaining to specific growth and nucleation models [32]. Mixtures of the specific nucleation models are not considered in the original derivation of JMA kinetics [5-8]. However, it can be proven (numerically) for such mixtures of nucleation models that, although the JMA description does not hold exactly, a very good approximation to the observed kinetics can still be given by the JMA description according to Eqs.(3.1)-(3.3) [32]. Thus, also intermediate values of the JMA kinetics parameters then are possible [32]. Determined values for the effective kinetic parameters can then be interpreted in terms of the basic nucleation and growth models, recognising the interdependence of the JMA kinetic parameters. In Ref.[32] it has been shown that the effective activation energy is given by the following weighted average of the activation energies of the involved nucleation and growth processes.

$$Q = \frac{\frac{d}{m}Q_g + \left(n - \frac{d}{m}\right)Q_N}{n}, \quad (3.7)$$

where Q_g and Q_N are the activation energies for growth and nucleation and d/m represents the growth mode with d as the number of dimensions in which the particles grow, and with $m=1$ in the case of interface controlled growth, and $m=2$ in the case of volume diffusion controlled growth. It can be shown that Eq.(3.7) holds in any case for nucleation modes varying between site saturation ($n=d/m$) and continuous nucleation ($n=d/m+1$). Now, if Q can be measured as function of n , e.g. by variation of the nucleation mode, Eq.(3.7) allows determination of the

activation energies for nucleation and growth separately.

3.3 Experimental

3.3.1 Alloy preparation

The master alloy was obtained by melting pure elemental Ni and Cu, and the compounds Ni₂P and Pd₇P₃ in an induction furnace using a BN crucible. The master alloy was then sealed in a silica glass tube under vacuum of 10⁻⁵ Torr. The tube containing the alloy was then heated in order to melt the alloy, and was quenched in water subsequently, resulting in amorphous Pd₄₀Cu₃₀P₂₀Ni₁₀. For details of the preparation of the alloy, see [35].

The amorphous material was cut to discs using a diamond saw. Different parts of the bulk alloy might have experienced (slightly) different thermal histories. In order to assure homogeneity of the material, every disc separately was crushed, and the resulting particles were mixed. Specimens used for DSC experiments consisted of many individual particles from one disc. In the following two different, crushed discs, denoted as batch I and batch II, are considered.

3.3.2 Differential scanning calorimetry

The differential scanning calorimeter (DSC) measurements were carried out using power compensated Perkin Elmer DSC's: a DSC-7 and a Pyris-1. As a function of time, the difference between the heating powers to keep the reference and sample at the same temperature was recorded, upon subjecting reference and sample to a certain temperature-time program. The temperature-time programs in this work involved both isothermal and isochronal (i.e. at constant heating rate) anneals. The applied heating rates for the isochronal experiments were 2.5, 5, 10, 20 and 40 K/min. Sample and reference pan were made of aluminium. The sample pan was filled with crushed alloy, and sealed with an aluminium cover. The reference pan was provided with two aluminium covers, in order to obtain a heat capacity of the reference comparable to that of the sample. A protective gas atmosphere of pure argon was employed. The temperature and the heat flow were calibrated by measuring the melting temperatures and the heats of fusion of pure In, Sn and Zn. The material stemming from batch I was measured using the Pyris-1 Perkin Elmer that allows a higher precision in the determination of the absolute temperature than the Perkin Elmer DSC-7 used for batch II.

3.3.2.1 Baseline correction

In the isothermal annealing experiments, a baseline drift was observed over a very long time

range. The baseline was determined by fitting an exponential decay function to the measured signal outside the time range where the crystallisation occurred.

In the isochronal annealing experiments, two baseline corrections were performed. The first correction is apparatus specific, and the second correction is specimen specific. Per sample, two identical DSC runs were made successively. The second run, then with the specimen in its crystalline state, served as an in situ recording of the baseline. Subtraction of this baseline from the first run realised the correction for the apparatus specific baseline shift, and as a result, the measurement curve was obtained.

During the crystallisation (in the first run), the state of the specimen changed from undercooled melt to crystalline. Hence, in the first run the specific heat of the specimen changed gradually from the specific heat of the undercooled melt to the specific heat of the crystalline compound. It was supposed that the overall specific heat of the specimen is given by the linear interpolation of the specific heats of the undercooled melt and the crystalline compound, and thus the overall specific heat is proportional to the fraction crystallised. Then, recognising that the specimen specific baseline is proportional to the specific heat, the second baseline correction is established iteratively:

- (i) An initial linear baseline was determined from the measurement curve in a start and an end point.
- (ii) Integration of the difference between the measurement curve and the baseline gave a signal proportional to the transformed fraction as function of temperature.
- (iii) A new baseline was estimated, by weighted averaging the values of the measurement curve in the start and the end point (see step(i)), using the transformed fraction resulting from step (ii) as weighing factor.
- (iv) Steps (ii) and (iii) were repeated until the difference between the baselines of two subsequent iteration steps was neglectably small.

The fully corrected DSC signal, i.e. after the baseline corrections as explained above, represents the rate of enthalpy uptake by the specimen due to the crystallisation: $d\Delta H/dt$, where ΔH is the enthalpy difference (ΔH is negative for crystallisation, i.e. heat is released).

3.3.2.2 Heating program

The influence of pre-annealing on the crystallisation kinetics was investigated by performing isothermal pre-annealing stages followed by isochronal or isothermal main-annealing stages. The entire temperature-time program for the experiments with an isochronal main-annealing stage is depicted in Fig.3.1.

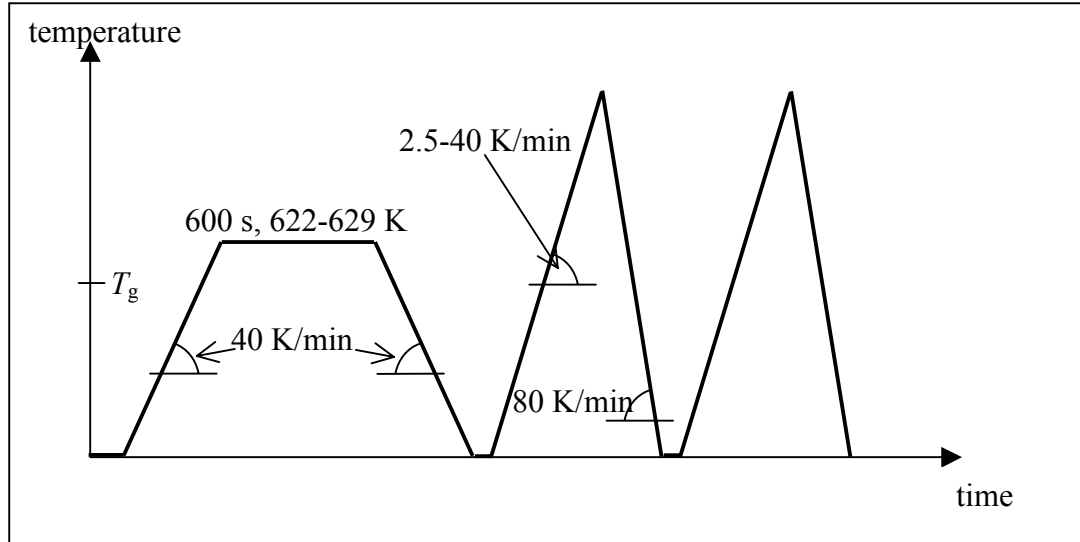


Fig.3.1: The two stage temperature-time program to which the specimens were subjected in the isochronal main-annealing experiments. The first stage was isothermal pre-annealing at temperatures higher than T_g , thus in the undercooled liquid state, at 622-629 K for 600 s. The second stage was isochronal main-annealing (twice, cf. section 3.3.2.1); applied heating rates were 2.5, 5, 10, 20 and 40 K/min.

Additionally, isothermal and isochronal annealing experiments were performed, without pre-annealing.

3.3.3 Data evaluation

The $d\Delta H/dt$ curves as obtained after the full baseline correction procedure (cf. section 3.3.2.1) were integrated, leading to values for the cumulative crystallisation enthalpy $\Delta H(t)$ during the main annealing stage. Then the transformed fraction is given by:

$$f(t) \equiv \frac{\Delta H_0 + \Delta H(t)}{\Delta H_{\text{tot}}}, \quad (3.8)$$

where ΔH_{tot} is the total crystallisation enthalpy, as determined from the DSC experiments without pre-annealing, and ΔH_0 is the enthalpy taken up during the pre-annealing stage. The value of ΔH_0 was calculated as the difference of ΔH_{tot} and $\Delta H(t_{\text{end}})$, which both are experimental values (here: ΔH_0 , $\Delta H(t_{\text{end}})$ and ΔH_{tot} are negative).

3.3.4 Fitting procedure

The kinetic parameters k_0 , Q and n were determined for a specific pre-annealing stage by fitting the kinetic model (cf. section 3.2) to the DSC curves as obtained for either the various heating rates (isochronal annealing experiments) or the various holding temperatures (isothermal annealing experiments), *simultaneously*. The fitting started with an assumed set of

values of k_0 , Q and n . Then, using Eqs.(3.1)-(3.3) (or, for the partial phase transition, Eqs.(3.2)-(3.6)) the transformed fraction f as a function of time t was calculated. The transformed fraction f_0 at the start of the main-annealing stage was known from Eq.(3.8). Then the calculated transformed fraction was used to calculate the rate of enthalpy uptake $d\Delta H/dt$ using Eq.(3.8). The least squares difference between the $d\Delta H/dt$ curves from the calculation according to the model and those from the measurements (section 3.3.2.1) was minimised using a downhill simplex fitting routine [24] by altering the kinetic parameters k_0 , Q and n .

The above described general fitting procedure had specific features for fitting isothermal and isochronal measurements. On fitting the isothermal measurements, $\Delta H(t_{\text{end}})$ was taken as a fourth fitting parameter because, at early stages of the isothermal measurement the measurement signal was affected by imbalance of the temperatures of reference and sample pans, which hindered the direct determination of $\Delta H(t_{\text{end}})$. On fitting the isochronal measurements, minimisation of the least squares difference was carried out with respect to the data for $d\Delta H/dT$ instead of $d\Delta H/dt$, because in this way measurements performed with different heating rates are given equal weight in the least squares minimisation.

3.3.5 Microscopy

The crushed alloy was embedded in a cold hardening polymer, after the crystallisation was performed in the DSC. After grinding and polishing, the specimen was etched using a mixture of 5 volume parts HNO₃ (70%) and 1 volume part HCl (37%) . Gold was sputtered on the surface to obtain an electrically conducting surface layer. The microstructure was then characterised by scanning electron microscopy (SEM) using a JEOL JSM-6400.

3.4 Results and evaluation

3.4.1 Kinetics

The isothermal measurements without pre-annealing were performed for material of batch I at temperatures of 610-630 K. The resulting DSC measurements and the corresponding fit of the kinetic model (simultaneous to all runs shown) are depicted in figure 3.2.

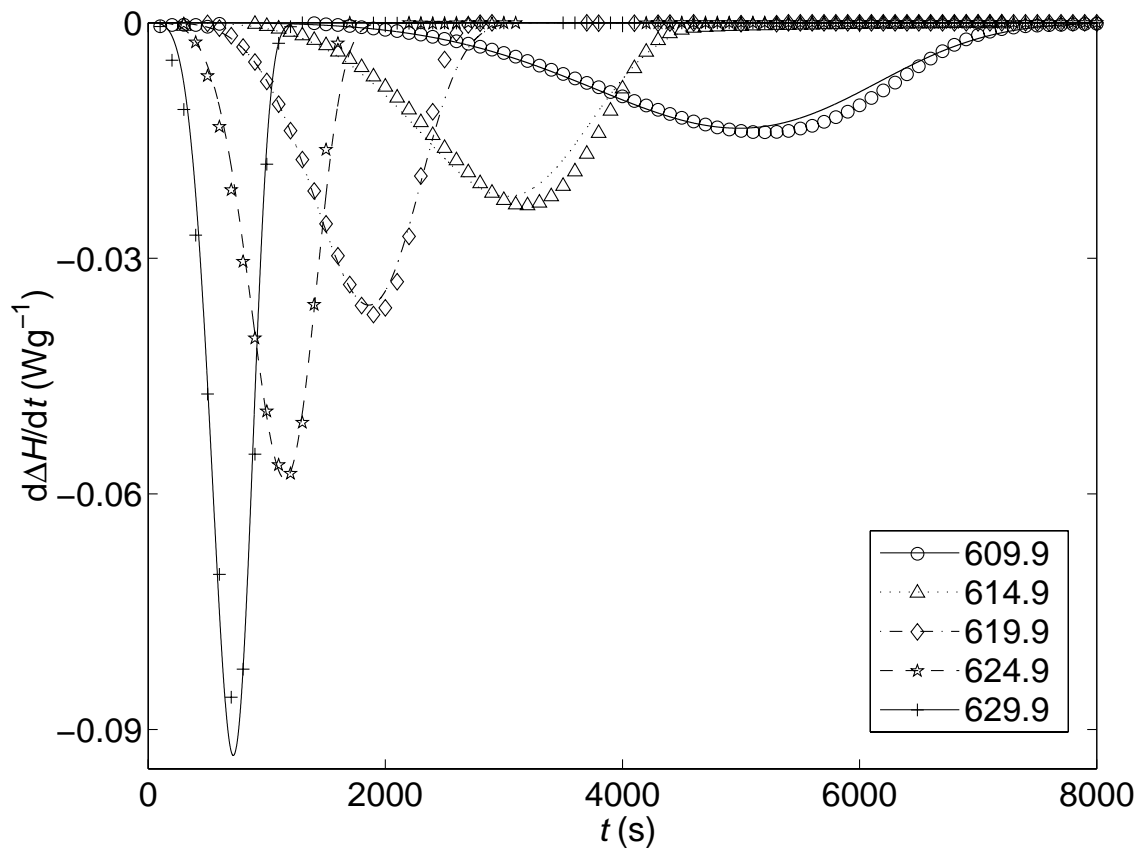


Fig.3.2: Rate of enthalpy uptake (due to crystallisation) as measured (symbols), and as fitted (lines) for isothermal annealing at temperatures 609.9, 614.9, 619.9, 624.9 and 629.9 K, for material from batch I. The fitting parameters obtained are given in Table 3.1.

Similar experimental and fit results for material of batch I after pre-annealing are shown in Fig.3.3. The specimens were pre-annealed for 600 s at 624.9 K, and then the main-isothermal annealing was performed. Clearly, the time needed to complete the crystallisation was significantly shorter after pre-annealing (cf. Figs.3.2 and 3.3).

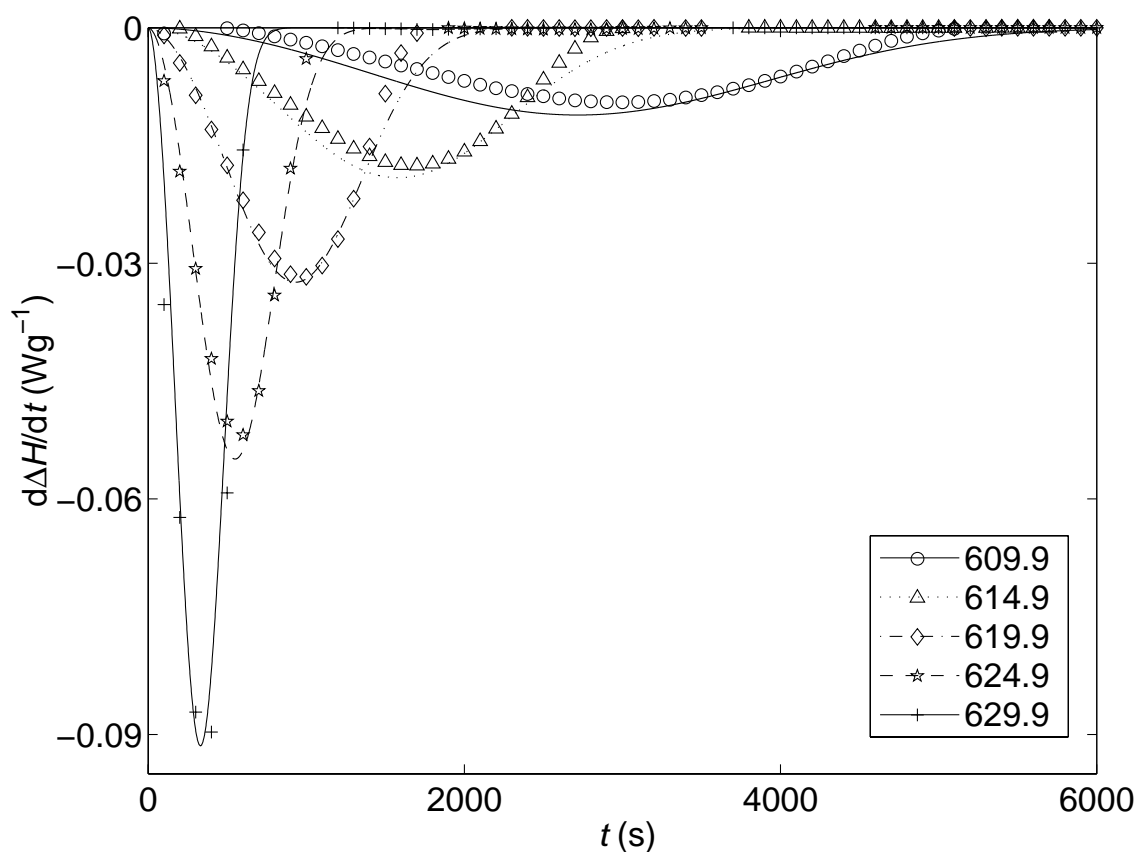


Fig.3.3: Rate of enthalpy uptake (due to crystallisation) as measured (symbols), and as fitted (lines) for isothermal annealing at temperatures 609.9, 614.9, 619.9, 624.9 and 629.9 K after pre-annealing 600 s at 624.9K, for material from batch I. The fitting parameters obtained are given in Table 3.1.

The goodness of the fit as shown in the Figs.3.2 and 3.3 was calculated as the sum of the absolute differences between the measured and the fitted $d\Delta H/dt$ values, divided by the sum of the absolute fitted $d\Delta H/dt$ values, for all isothermal holding temperatures, and for the entire measured time range. This goodness of the fit is shown in Table 3.1 as error percentage. Fits of reasonable quality have been obtained. Note that fitting of the kinetic model is performed in Figs.3.2 and 3.3 to the results of five isothermal anneals *simultaneously*; fitting of the kinetic model to the measured result for one temperatures would have led to a fit of higher quality for that temperature.

The results for the kinetic parameters obtained in the isothermal annealing experiments have been gathered in Table 3.1. The incorporation of pre-annealing in the kinetic model via the extended transformed fraction (section 3.2.1) leads to fits of the transformation kinetics of quality comparable to the fits performed in the absence of pre-annealing. Pre-annealing influences the kinetic parameters: n decreases, and Q and k_0 increase due to pre-annealing. As

follows from the $\Delta H(t_{\text{end}})$ values, crystallisation took place during the pre-annealing.

Table 3.1: Kinetic parameters n , Q and k_0 , and enthalpy change due to crystallisation $\Delta H(t_{\text{end}})$, as determined by fitting (except for $\Delta H(t_{\text{end}})$, for the isochronal annealing experiments which was determined directly; see section 3.3.4), after different pre-annealings at T_{pre} , or without pre-annealing (-).

pre-anneal T_{pre} (K)	Measurement method	n	Q (kJ/mol)	k_0 (s ⁻¹)	error (%)	$\Delta H(t_{\text{end}})$ (J/g)
-	isothermal	4.75	309	5.4e+022	9.8	-39.3*
624.9	isothermal	2.81	336	2.0e+025	15.3	-31.7*
-	isochronal	3.36	224	6.6e+015	27.6	-50.0
624.9	isochronal	2.82	258	6.9e+018	17.0	-41.4

* $\Delta H(t_{\text{end}})$ determined by fitting

The isochronal crystallisation kinetics of material of batch I was investigated as well, for the not-pre-annealed specimens, and for specimens pre-annealed for 600s at 624.9 K. The kinetic parameters as obtained by fitting the kinetic model to the measurements as described in section 3.3.4 (simultaneous fitting to all measurement runs of various heating rates) have been given in Table 3.1 as well. For the isochronal measurements the goodness of the fit was defined as the sum of absolute differences between the measured and the fitted $d\Delta H/dT$ values, divided by the sum of the absolute fitted $d\Delta H/dT$ values, for all heating rates and the entire measured temperature range.

As compared to the results obtained for isothermal transformation kinetics, the influence of the pre-annealing on the kinetic parameters is similar: $\Delta H(t_{\text{end}})$ and n decrease, and Q and k_0 increase due to pre-annealing. The quantitative differences between the values of the kinetic parameters for the isothermal and isochronal transformation kinetics are discussed in section 3.5.

Material from batch II was subjected to 8 different pre-annealing treatments, followed by isochronal main-annealing stages. The DSC scans as measured after three pre-annealing treatments (600s at 623, 626 and 629 K) and measured using five heating rates (2.5, 5, 10, 20 and 40 K/min) and the corresponding fits of the kinetic model (simultaneous to all runs after one pre-anneal) are shown in Fig 3.4.

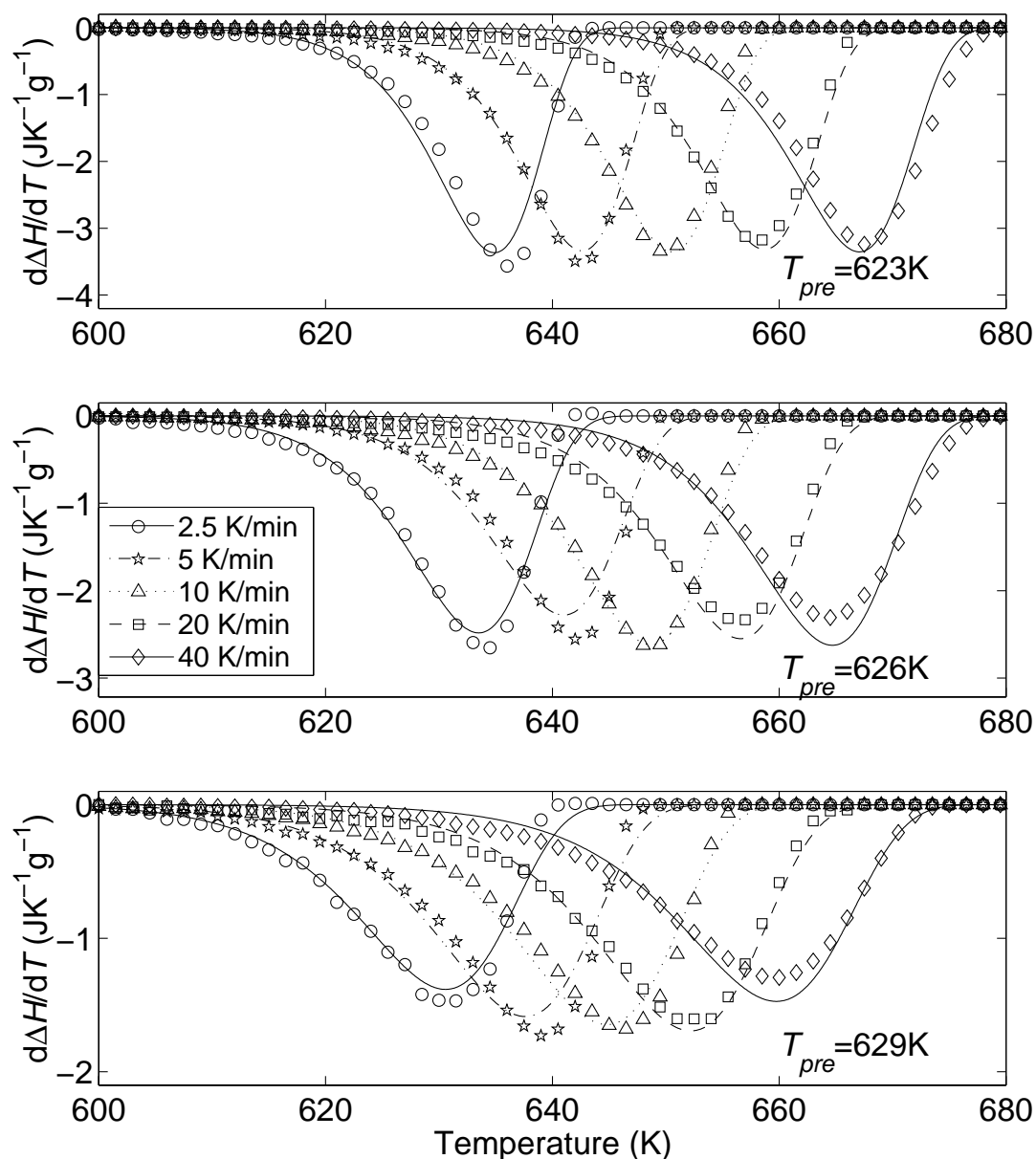


Fig.3.4 Rate of enthalpy uptake (due to crystallisation) divided by the heating rate as, measured from material from batch II (symbols), and as fitted (lines) according to section 3.3.4, after pre-annealing at 623, 626 K and 629 K. The used heating rates were 2.5, 5, 10, 20 and 40 K/min. The fitting parameters obtained are given in Table 3.2.

Similar to the above discussion (cf. discussion of the isothermal anneals of batch I), in judging the quality of the fits it should be recognised that the kinetic model is fitted to the measured data for five isochronal anneals simultaneously. Also similar to the results obtained from the isothermal anneals of batch I, and as now follows from in total eight different pre-

anneals, incorporation of the effect of pre-annealing through the extended transformed fraction leads consistently to fits of good quality (see Fig.3.4 and Table 3.2). The higher the pre-annealing temperature (T_{pre}), the lower the temperature where crystallisation started, the broader the crystallisation peak, and the smaller the value of $\Delta H(t_{end})$. The dependence of the kinetic parameters on pre-annealing (cf. Table 3.2) is discussed in section 3.5.

Table 3.2 Kinetic parameters n , Q and k_0 as determined by fitting, the error of the fit and the enthalpy change due to crystallisation $\Delta H(t_{end})$ for isochronal measurements after different pre-annealings at T_{pre} , for material from batch II.

T_{pre} (K)	n	Q (kJ/mol)	k_0 (s ⁻¹)	error (%)	$\Delta H(t_{end})$ (J/g)
620	3.05	298	9.6e21	16.60	-45.0
622	2.78	281	4.6e20	11.74	-44.4
623	2.44	292	3.9e21	13.65	-43.7
625	2.04	304	4.5e22	13.84	-41.7
626	2.01	300	2.0e22	13.71	-39.2
628	1.71	307	1.0e23	13.95	-35.4
629	1.55	317	7.8e23	12.43	-29.6

3.4.2 Microstructure

The microstructures of specimens from batch I were analysed after the following treatments:

- Isothermal holding at temperatures in the range 609.9-629.9 K.
- Pre-annealing for 600 s at 624.9 K, and subsequently isothermal main-annealings at temperatures in the range 609.9-629.9 K.
- Isochronal annealing, performed twice (see Fig.3.1) from 323 to 723 K at heating rates from 2.5 to 40 K/min.
- Pre-annealing for 600 s at 624.9 K, and subsequently isochronal main-annealings, performed twice from 323 to 723 K at heating rates from 2.5 to 40 K/min.

Characteristic results, obtained from specimens from groups (a)-(d) are shown in Fig.3.5.

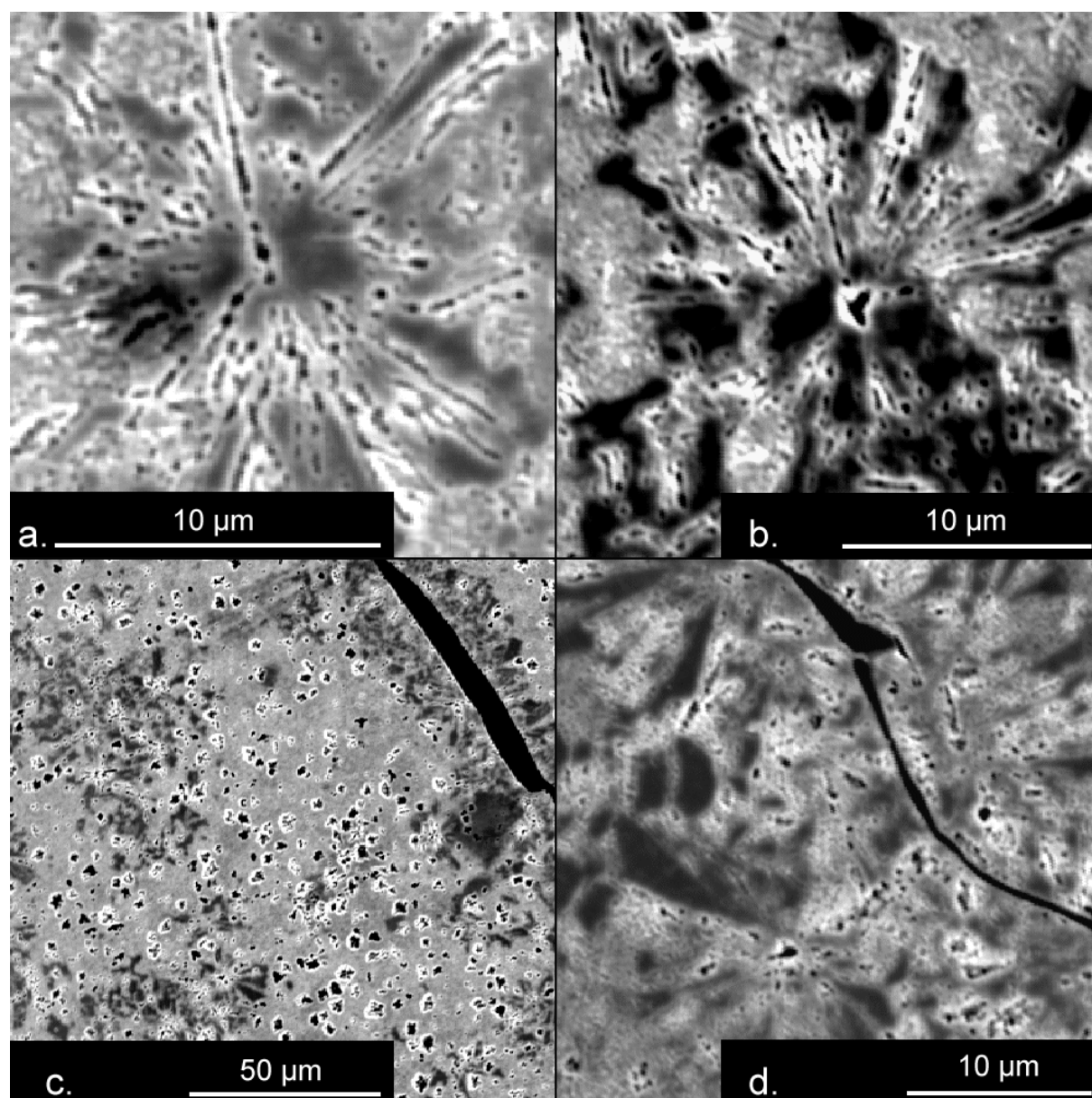


Fig.3.5 Micrographs (SEM) of four specimens of batch I, after full transformation, (a) isothermal (609.9-624.9K), (b) isothermal (609.9-624.9 K) after pre-annealing at 624.9 K, (c) isochronal (2.5-40 K/min) and (d) isochronal (2.5-40 K/min) after pre-annealing at 624.9 K.

In total four different crystalline phases should be present in the specimens depicted in Fig.3.5¹. Due to experimental difficulties in preparing a high quality specimen from the crushed specimen material, the quality of the depicted micrographs does not allow determination of the number of occurring phases. The black, more or less, equiaxed dots occurring in all four microstructures, are probably due to preferentially breaking out of one of

¹ The phases, which formed during crystallisation, were Pd₂Ni₂P, Pd₁₅P₂, Ni₃P and Cu₃P according to [36-38]. Note that the gross composition of the investigated alloy cannot be explained exactly as resulting from a mixture of these phases for the compositions as indicated.

the phases during the polishing. Further, cracks are visible, in the Figs.3.5 b and c. In particular, important information about the growth mode of the crystalline phases can be obtained from the micrographs. Evidently the crystalline particles in the isothermally crystallised specimens (a-b in Fig.3.5) have grown radially, star-like. The morphology of the crystalline products in the isochronally crystallised specimens (c-d in Fig.3.5) does not show this pronounced star-like microstructure, instead the grains appear to be more or less equiaxed. Thus the influence of the type of main-annealing on the microstructure is very strong (i.e. compare a-b with c-d in Fig.3.5; see also results in Refs.[37, 39]). The influence of pre-annealing on the microstructure is not apparent (compare a and b, and compare c and d in Fig.3.5).

3.5 General discussion

The JMA exponent derived from the isothermal crystallisation experiments is (both with and without pre-annealing) larger than the JMA exponent derived from the isochronal crystallisation experiments (see Table 3.1). Thus, the set of isothermal experiments is not isokinetic with the set of isochronal experiments. This may be understood on the basis of the observed microstructures (Fig.3.5). The morphology of the microstructure after isothermal crystallisation is ascribed to the result of eutectic growth, i.e. the various crystalline product phases have grown co-operatively outwardly, starting from a nucleus, leading to the star-like morphology. The rate limiting process then is expected to be diffusion at the growth front, and thus the growth mode will be interface controlled, resulting in a JMA exponent between 3 and 4 [2, 32]. The morphology of the microstructure after isochronal crystallisation is considered to be the result of volume diffusion controlled growth, as compatible with precipitation of a phase in a matrix differing in composition with the matrix. Rate control by volume diffusion (in the amorphous matrix) for precipitation of equiaxed particles corresponds with a JMA exponent between $3/2$ and $5/2$ [2, 32].

Differences between the ranges of measured values of the JMA exponent and the expected ones according to the above discussion (i.e. isothermal experiment: $3 < n < 4$, and isochronal experiment $1.5 < n < 2.5$) can be interpreted as the consequence of the occurrence of nucleation processes that do not (fully) comply with the considered extremes: site saturation and continuous nucleation. In cases where n is relatively large, (i.e. in cases where no pre-annealing was performed), non-steady state nucleation [26, 40] probably governed the nucleation process.

The relation between the effective activation energy, Q , and the JMA exponent, n , given

by Eq.(3.7) should hold in any case for those cases where n obeys the above indicated limits [32]. For the isochronal annealing experiments after various pre-anneals (cf. Table 3.1), the growth mode is controlled by volume diffusion in three dimensions (cf. above discussion), which leads to $m=2$ and $d=3$. (cf. Eq.(3.7)). On this basis, Eq.(3.7) can be fitted to the experimental values for n and Q , obtained from experiments after pre-annealing at 623-629K. The result is shown in Fig.3.6.

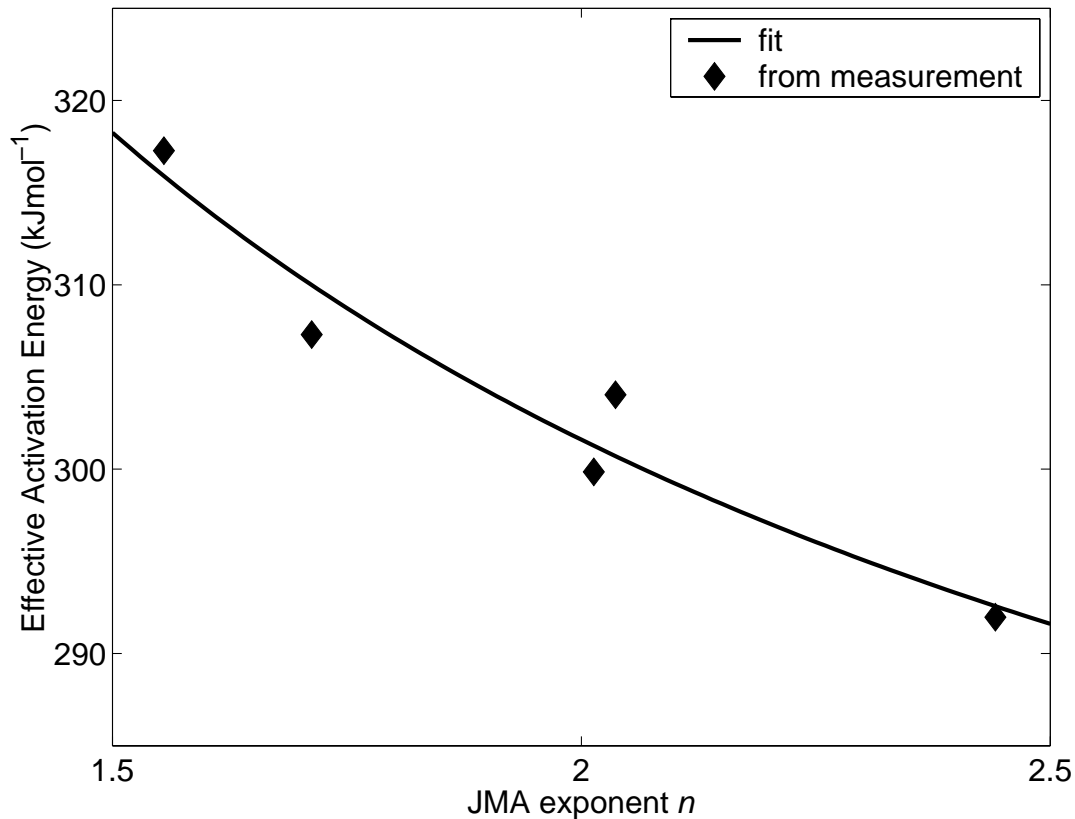


Fig.3.6. The effective overall activation energy Q as function of the JMA exponent n , as determined from fitting JMA kinetics to the phase transformation as measured, after pre-annealing at 623-629 K (◆). The full line has been obtained by fitting Eq.(3.7) to the data points.

Clearly, Eq.(3.7) describes the experimental results well. The corresponding, resulting values for the separate activation energies for nucleation and growth are: $Q_N = 252$ kJ/mol and $Q_g = 318$ kJ/mol.

For a similar glass, $Pd_{40}Ni_{40}P_{20}$, the activation energy for diffusion of Au in the amorphous phase was determined at 420 kJ/mol [27, 41]. The value of the activation energy for diffusional growth as determined here (319 kJ/mol) is lower than the activation energy for Au diffusion in amorphous $Pd_{40}Ni_{40}P_{20}$ (420 kJ/mol), but it is higher than the values for self diffusion in the crystalline pure metals: the activation energies for self diffusion are for Pd,

266 kJ/mol, for Cu 209 kJ/mol and for Ni 285 kJ/mol [28]. Therefore, the present result for Q_g is considered plausible.

The value obtained for the activation energy for nucleation (252 kJ/mol) is within the range of activation-energy values for nucleation measured for metal-metalloid glasses (Co₇₀B₃₀: 191 kJ/mol, Fe₆₅Ni₁₀B₂₅: 300 kJ/mol [26]). Therefore, the present result for Q_N is considered plausible as well.

3.6 Conclusions

1. Overlapping nucleation and growth processes in phase transformations can be characterised separately by a combination of isothermally and non-isothermally (e.g. isochronally) conducted annealing experiments.
2. Different growth modes occur upon isothermal and isochronal crystallisation of amorphous Pd₄₀Cu₃₀P₂₀Ni₁₀: isothermal crystallisation: interface controlled growth; isochronal crystallisation: volume diffusion controlled growth.
3. Only under certain conditions the crystallisation of Pd₄₀Cu₃₀P₂₀Ni₁₀ can be described according to classical Johnson-Mehl-Avrami (JMA) kinetics: pre-annealing is required to avoid non-steady state nucleation.
4. A general formulation for the interpretation of the effective, overall activation energy, not requiring that JMA kinetics should hold strictly, can be applied to determine the activation energies for the nucleation and growth processes, separately (Eq.(3.7)). Application to the isochronal crystallisation of Pd₄₀Cu₃₀P₂₀Ni₁₀ led to reasonable values for the occurring nucleation and growth processes: 252 kJ/mol and 318 kJ/mol.

4 Kinetics of consecutive, coupled phase transformations

A.T.W. Kempen, F. Sommer and E.J. Mittemeijer

Keywords: coupled phase transformations, kinetics, two-step crystallisation, Mg-Ni-La alloy

Abstract

A model has been developed for the description of consecutive, coupled phase transformations. The model has been developed explicitly in a case where it is assumed that a reaction product of a first reaction is consumed by a second reaction and that the second reaction has a thermally activated incubation time. The model has been applied to phase transformations associated with crystallisation of amorphous $\text{Mg}_{50}\text{Ni}_{30}\text{La}_{20}$. The results are interpreted in terms of specific nucleation and growth processes.

4.1 Introduction

Consecutive phase transformations often occur. A common example is the austenite to ferrite transformation upon cooling in a hypo-eutectoid Fe-C alloy: the first reaction involves precipitation of ferrite, in combination with carbon enrichment of the remaining austenite, and the second reaction is the eutectoid pearlite formation. These reactions occur consecutively and, also, the second reaction consumes a product of the first reaction, and thereby coupling of two consecutive reactions is realised. In this project, a kinetic model for (two) coupled reactions is developed and applied to phase transformations occurring upon crystallisation of Mg₅₀Ni₃₀La₂₀ melt spun alloy.

4.2 Kinetic model

Consider two consecutive, coupled reactions, as follows:



The kinetics of the first reaction is described using the differential form of a Johnson-Mehl-Avrami (JMA) equation:

$$\frac{dx^{\beta+\gamma}}{dt} = x^\alpha \frac{d\left(\left(\int_0^t k_1 dt\right)^{n_1}\right)}{dt}, \quad (4.2a)$$

where $x^{\beta+\gamma}$ denotes the fraction reaction product of the first reaction (incorporating the part of β that already transformed to γ), t is the time, k_1 follows an Arrhenius temperature dependence and incorporates an effective activation energy accounting for both nucleation and growth and n_1 is the so called JMA exponent [2, 9].

The kinetics of the second reaction is developed in a manner related to the derivation of Eq.(4.2a). A virtual parameter called the extended volume of product phase γ is calculated first. The extended volume differs in two ways from the actual volume of phase γ : it implies virtual nucleation in the already transformed volume (i.e. phase γ) and also, the transformed volume can hypothetically grow into already transformed material. The treatment runs as follows. The number of γ phase nuclei formed during a time lapse $d\tau$ in a volume $V^{\beta+\gamma}$ ($\equiv V^\beta + V^\gamma$; the specific volume changes are ignored) can be given by ${}^v I_2 V^{\beta+\gamma} d\tau$ with ${}^v I_2$ as the nucleation frequency per unit volume. The growth of the volume of a transformed region that nucleated at time τ is given by $(4\pi((t-\tau)Y_2)^3/3)$ with Y_2 as the isotropic growth rate and t as

the time. Hence, the transformed extended volume of phase γ due to nucleation and growth is given by:

$$V_e^\gamma = \int_0^t V^{\beta+\gamma} \frac{4\pi}{3} ((t-\tau)Y_2)^3 {}^v I_2 d\tau, \quad (4.3)$$

recognising that $V^{\beta+\gamma}$ and ${}^v I_2$ depend on time, and that in case of diffusional growth, Y_2 depends on $(t-\tau)$. To calculate the increase of actual volume of the phase γ , dV^γ , it is plausible to suppose that the fraction of the change in extended volume as large as the ratio of the untransformed volume V^β and the total *available* volume $V^{\beta+\gamma}$ equals the change in actual volume of phase γ .

$$dV^\gamma = \frac{V^\beta}{V^{\beta+\gamma}} dV_e^\gamma. \quad (4.4)$$

Then, dividing the left- and right-hand sides of Eq.(4) by dt and substituting Eq.(3), and simultaneously replacing the volumes by fractions transformed (i.e. $x^i \equiv V^i/V^{\alpha+\beta+\gamma}$ with i being α , β , γ or combinations of these phases) one obtains:

$$\frac{dx^\gamma}{dt} = x^\beta \frac{d\left(\int_0^t \frac{4\pi}{3} ((t-\tau)Y_2)^3 {}^v I_2 d\tau\right)}{dt}. \quad (4.2b)$$

This equation has the same form as Eq.(4.2a) but note that x^β is not only determined by the intrinsic kinetic behaviour of the second reaction, but also depends on the kinetics of the first reaction. Therefore, integration of Eq.(4.2b) will lead to a JMA-like equation.

It will be supposed that, without adopting specific temperature-time dependencies, the integral on the right hand side of Eq.(4.2b) can be written as [9].

$$\left(\int_0^t k_2 dt\right)^{n_2} = \int_0^t \frac{4\pi}{3} ((t-\tau)Y_2)^3 {}^v I_2 d\tau. \quad (4.5)$$

In specific cases, the left hand side of Eq.(4.5) can be written as $(kt)^n$. This can hold for isothermal transformations, where k is independent of time. A well known example is the site saturation case in which all the nuclei are present at the beginning of the transformation, before growth occurs. Then the expected JMA-like exponent equals 3 for three dimensional interface controlled growth (Y_2 independent of time), and 3/2 for three dimensional diffusion controlled growth ($Y_2 \propto (t-\tau)^{-3/2}$). In case of non-isothermal transformations, similar interpretations are not straightforward. However, for a limited range of transformation temperatures, it may be assumed that the time dependence of Y_2 is much stronger than the temperature dependence, and n_2 could be interpreted as above.

The second reaction may have an additional incubation range (not only in time, as for isothermal annealing, but also in temperature in the case of non-isothermal annealing). The implementation of such an incubation range does not change anything in Eq.(4.2b), only the boundary conditions for the integration of Eq.(4.2b), to calculate x^y , change.

4.3 Experimental procedures and data evaluation

Firstly, a Ni₃₀La₂₀ alloy was produced by melting Ni and La in an arc furnace. Secondly, this pre-alloy and pure magnesium were melted in an induction furnace, both under argon atmosphere. Thirdly, the resulting alloy was melt spun under a helium atmosphere. The rate of the studied transformations was determined by Differential Scanning Calorimetry (DSC) using a Perkin Elmer DSC II. The DSC was calibrated by the melting of indium, tin and zinc. The transformations were studied applying isochronal annealing using 2.5, 5, 10, 20 and 40 K/min, both without pre-annealing and with isothermal pre-annealing at temperatures above the glass-transition temperature. The base-line construction under the measured peaks was performed iteratively by assuming the height of the baseline to be proportional to the total transformed fraction (which is defined as $x_{tot} \equiv (x_1 \Delta H_1 + x_2 \Delta H_2) / \Delta H_{tot}$ with ΔH_i and x_i being the corresponding reaction enthalpy and transformed fraction).

Qualitative phase analysis was performed by making Guinier X-ray diffraction photographs using copper $K\alpha_1$ radiation at different stages of transformation.

The differential Eqs.(4.2) were numerically integrated using an Euler's [24] and using the mentioned $(kt)^n$ approach, with $k \equiv k_0 \exp(-E/RT)$. The incubation range for the second peak was implemented by supposing the second reaction to start at a fixed fraction transformed of the first reaction x_1^{2start} . The initial value of the fit parameter activation energy E_i was obtained from an activation energy against transformed fraction plot, determined by applying a Kissinger like analysis as a function of the total fraction transformed [9]. From the sharp bend in the same plot, the initial value for x_1^{2start} was determined. The initial values of n_i , pre-exponential factor k_{0i} and $\Delta H_i / \Delta H_{tot}$ were obtained through a visual fit. The calculated total transformed fraction rates (dx_{tot}/dT) were fitted to the measurements for five heating rates simultaneously using a downhill simplex algorithm [24].

4.4 Results and Discussion

The reaction induced upon crystallisation invokes the occurrence of a double peak in a DSC scan. X-ray diffraction analysis did not show any difference between the phase produced in reaction 1 and the phase produced in reaction 2: diffraction patterns recorded from specimens

heated up till the first peak (followed by quenching) did not differ visibly from those recorded from specimens heated till completion of the entire transformation (followed by quenching). The crystal structure of the product phases could not be determined from the diffraction patterns definitively until now.

Two series of isochronal DSC scans are presented in Figs.4.1 and 4.2: crystallisation at heating rates 2.5 and 20 K/min for both the not pre-annealed condition (Fig.4.1) and the condition after pre-annealing at 483 K for 600 s (Fig.4.2). The measured total reaction enthalpy (ΔH_{tot}) is obtained by integration of the measurement signal. The fits of the present kinetic model Eqs(4.2) (using the $(kt)^n$ approach) to the measured data are also shown in Figs.4.1 and 4.2. The simultaneous fits for five different heating rates led to values of the fit parameters shown in Table 4.1. The calculations do not show the second peak becoming sufficiently sharper at low heating rates, as prescribed by the measurements. Possibly, the assumption of the $x_1^{2\text{start}}$ to be constant for all heating rates is not correct. Further, a tail on the right-hand side of the peaks is measured, that is not provided by the calculations. This may be due to soft impingement (of diffusion fields) in a late stage of the transformation. Because of this systematic misfit the measured total reaction enthalpy is somewhat larger than the sum of the calculated partial reaction enthalpies.

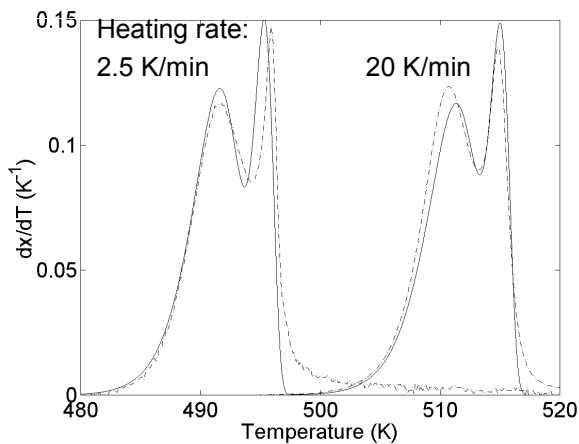


Fig.4.1 Measured (dotted lines) and fitted (full lines) transformed fraction rate against temperature for isochronal crystallisation of $\text{Mg}_{50}\text{Ni}_{30}\text{La}_{20}$ at heating rates of 2.5 and 20 K/min recorded from not pre-annealed specimens

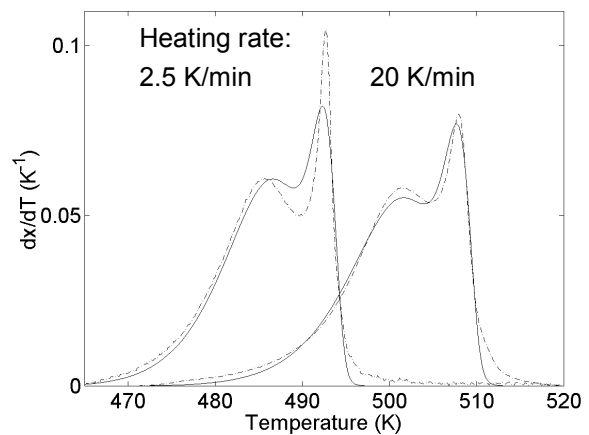


Fig.4.2 Measured (dotted lines) and fitted (full lines) transformed fraction rate against temperature for isochronal crystallisation of $\text{Mg}_{50}\text{Ni}_{30}\text{La}_{20}$ at heating rates of 2.5 and 20 K/min recorded after isothermal pre-annealing at 483 K for 600 s.

In general, discrepancies between fit and measurements can also be due to non-validity of the $(kt)^n$ approach.

Table 4.1: Kinetic parameters obtained for both reactions from fitting the kinetic model to DSC-measurements without pre-annealing, and with pre-annealing at 477K, 480K and 483K for 600s.

		No pre-anneal		Pre-anneal 477 (K)		Pre-anneal 480 (K)		Pre-anneal 483 (K)	
ΔH_{tot}	(J/g)	83±6		77±7		75±5		67±5	
Peak (i=1,2)		1	2	1	2	1	2	1	2
E_i	(kJ/mol)	222	224	245	290	242	269	253	270
k_{0i}	(s ⁻¹)	6.7•10 ²⁰	3.6•10 ²¹	2.2•10 ²³	2.8•10 ²⁸	1.2•10 ²³	1.8•10 ²⁶	2.6•10 ²⁴	1.8•10 ²⁶
n_i		3.4	3.1	2.4	2.5	1.8	2.9	1.4	3.1
ΔH_i	(J/g)	52	27	51	23	56	16	48	17
x_1^{2start}		0.82		0.73		0.65		0.55	

The misfit, defined as the sum of the absolute differences between fitted and measured points divided by the sum of all data points, equals ~0.15.

As it is unlikely that pre-annealing changes the dimensionality of the growth or the growth mode, the decrease of the JMA exponent of the first reaction through pre-annealing is ascribed to a change of nucleation rate. If for the first reaction, in the pre-annealed case (483 K), site saturation holds (all nuclei present at $t=0$ s) then the JMA exponent is due to growth only. Then, for three-dimensional diffusional growth, the JMA exponent is predicted as $n_1=3/2$. Indeed in the most pronouncedly pre-annealed case ($T=483$ K), $n_1=1.4$. For cases of less pronounced pre-annealing, some nucleation may occur in the beginning of the first reaction, leading to larger values of n_1 (Table 4.1).

Obviously, for the second reaction, pre-annealing should not influence the kinetics. Indeed the JMA-like exponent n_2 is independent of pre-annealing. The observed value of n_2 may be explained as follows: site saturation at x_1^{2start} , with three-dimensional non-diffusional growth for all pre-annealing cases, leading to $n_2=3$.

4.5 Conclusions

1. Consecutive coupled solid-state phase transformations can be described by a Johnson-Mehl-Avrami treatment for the first reaction, whereas for the following reaction(s), a related treatment is possible, but recognising that the transformed fraction of such a reaction depends on the transformed fraction of the preceding reaction(s).
2. Crystallisation of amorphous Mg₅₀Ni₃₀La₂₀ appears to consist of two consecutive reactions, where the first reaction is a three dimensional diffusional growth process,

from pre-existing nuclei due to pre-annealing. The second reaction is independent of pre-annealing, and may be interpreted as a three dimensional non-diffusional growth process with site saturation at $x_1^{2\text{start}}$.

5 Crystallisation kinetics of amorphous magnesium-rich magnesium-copper and magnesium-nickel alloys

A.T.W. Kempen, H. Nitsche, F. Sommer and E.J. Mittemeijer

Keywords: kinetics, crystallisation, metastable phase, rapid solidification

Abstract

Amorphous magnesium-rich alloys Mg_yX_{1-y} ($X = Ni, Cu$ and $0.82 < y < 0.89$) have been produced by melt spinning. The crystallisation kinetics of these alloys has been determined by in-situ X-ray diffraction and isothermal and isochronal Differential Scanning Calorimetry combined with ex-situ X-ray diffraction. Microstructure analysis has been performed by means of Transmission Electron Microscopy and Electron Energy Loss Spectroscopy.

Crystallisation of the Mg-Cu alloys at high temperature takes place in two steps: primary crystallisation of Mg, followed by simultaneous crystallisation of the amorphous rest phase to Mg and Mg_2Cu . Crystallisation of the Mg-Cu alloys at low temperatures takes place in one step: eutectic crystallisation of Mg and Mg_2Cu . Crystallisation of the Mg-Ni alloys for a Mg content $y > 0.85$ takes place in two steps: primary crystallisation of Mg and of a metastable phase ($Mg_{\sim 0.5}Ni$, with Mg content $y = 0.85$), followed by the decomposition of $Mg_{\sim 0.5}Ni$. Crystallisation of the Mg-Ni alloys for a Mg content $y < 0.85$ predominantly takes place in one step: eutectic crystallisation of Mg and Mg_2Ni . Within the experimental window applied (i.e. $356 K < T < 520 K$ and $0.82 < y < 0.89$), composition dependence of the crystallisation sequence in the Mg-Cu alloys and temperature dependence of the crystallisation sequence in the Mg-Ni alloys, has not been observed.

5.1 Introduction

Solid state phase transformations are important means for the adjustment of the microstructure, and thus the tuning of the properties of materials. In order to exploit this tool to full extent, much effort is spent on the modelling of phase transformations. A general phase transformation model is presented in Ref.[32]. This model was shown to describe the crystallisation of a *quaternary* metal-metalloid glass very well [25]. As another, possibly less complicated, model system, crystallisation of *binary* metal-metal glasses has been studied in the present project.

The considered model systems are Mg_yX_{1-y} alloys ($X= Ni, Cu$ and $0.82 < y < 0.89$), which can be made amorphous around the Mg-rich eutectic composition [42, 43]. The availability of thermodynamic [42, 44-46] and crystallographic [47-49] data is helpful for the modelling of the crystallisation of the alloys. The thermodynamic stable phases in the studied systems are Mg and Mg_2X , which are crystallographically similar [47]. However, during the crystallisation of Mg-Ni, an unknown metastable phase is formed, which is not the case in the Mg-Cu system [42, 43].

5.2 Theoretical background

5.2.1 Crystallisation

The crystallisation of an amorphous alloy takes place in a polymorphous, primary or eutectic fashion [50]. Upon polymorphous crystallisation, the compositions of the crystalline product phase and the amorphous parent phase are equal; no volume diffusion takes place. Upon primary crystallisation, one crystalline product phase of composition different from the overall alloy composition precipitates from the parent amorphous matrix. Long range material transport is needed during primary crystallisation. Further, at least one subsequent process (for crystallisation of the remaining amorphous matrix) is needed to arrive at the thermodynamic stable state. Upon eutectic crystallisation, crystalline product phases of different composition form simultaneously. Depending on the temperature gradient in the material and on the growth velocity of the new phases, the microstructure becomes lamellar or fibrous (absence of long range diffusion), or globular (occurrence of long range diffusion) [51].

Apart from the inherent occurrence of two steps during a primary crystallisation process [52, 53], another reason for two steps in a crystallisation process is the precipitation of a

metastable phase, followed by transformation of the metastable phase to a phase of higher stability [50].

5.2.2 Phase transformation kinetics

In general, the progress of a phase transformation, defined as the fraction transformed f , depends on a path variable β . This variable β is given by the integral of the temperature (T) dependent reaction rate constant, k , over time (t) [9, 32]:

$$\beta = \int k(T(t)) dt. \quad (5.1)$$

Hence the rate constant is considered not to depend on t other than through $T(t)$. The exact dependence of f on β , implying also the dependence of k on T , is prescribed by the specific kinetic model that is applied. For crystallisation of (metallic) glasses, Johnson-Mehl-Avrami (JMA) kinetics may provide a good description [25]. Then, the fraction transformed, f , depends on the path variable β through:

$$f = 1 - \exp(-\beta^n), \quad (5.2)$$

with n as the JMA exponent and the reaction rate constant is then given by:

$$k(T(t)) = k_0 \exp\left(-\frac{Q}{RT(t)}\right). \quad (5.3)$$

where k_0 is the pre-exponential factor, Q the effective activation energy and R is the gas constant.

The parameter β^n is also called the extended transformed fraction [6-8, 32], x_e . This is the sum of the volumes of all (hypothetical) grains, divided by the total specimen volume, assuming that the grains never stop growing and that new grains hypothetically nucleate also in the transformed material [33] (i.e. for determination of x_e , 'hard impingement' is ignored; note that Eq.(5.2) does take the effect of 'hard impingement' into account [2]).

The formulation of the kinetic model as given in Eqs.(5.1)-(5.3) is valid for both isothermal and isochronal transformations, and, as long as the transformation can be considered isokinetic [2, 34] the obtained JMA kinetic parameters k_0 , n and Q are independent of the temperature-time program.

Strictly speaking, the JMA kinetic parameters can only have certain values, pertaining to specific growth and nucleation models [32]. Mixtures of the specific nucleation models are not considered in the original derivation of JMA kinetics [5-8]. However, it can be proven (numerically) for such mixtures of nucleation models that, although the JMA description does not hold exactly, a very good approximation to the observed kinetics can still be given by the

formulation of the JMA model as given in Eqs.(5.1)-(5.3) [32]. Thus, also intermediate values of the JMA kinetics parameters then are possible [32].

5.3 Experimental

5.3.1 Alloy production

Production of the Mg-X alloys was complicated by the high vapour pressure of Mg at the melting temperature of the alloying element X. To counteract this problem high purity thinly rolled sheets of Ni (99.98%) or Cu (99.999%) were put into the Mg (99.95%) melt. The Ni or Cu sheet dissolved in the Mg melt without increasing the temperature of the melt much above the melting temperature of Mg. This procedure was performed in an induction furnace where evaporation of Mg was further suppressed by melting under argon pressure. The alloyed melt was cast in a copper die. Two compositions for each system were produced: alloys with eutectic composition, Mg_{85.5}Cu_{14.5} (A) and Mg_{88.7}Ni_{11.3} (C), and alloys with off-eutectic composition Mg_{82.7}Cu_{17.3} (B) and Mg_{82.0}Ni_{18.0} (D) (see Fig.5.1).

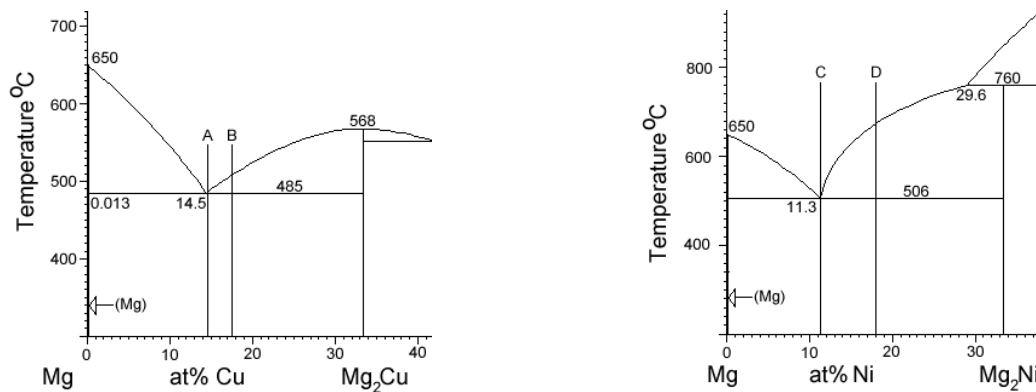


Fig.5.1 Partial phase diagrams of a. Mg-Cu and b. Mg-Ni [54]. The composition of the studied alloys, indicated by A-D, has been indicated in the diagrams.

5.3.2 Melt spinning

The cast alloy was molten under helium atmosphere, and was ejected through an orifice onto the surface of a rapidly rotating copper disc. The surface speed of the wheel was 35 m/s. The thickness of the resulting ribbons was between 25 and 27 μm for the Mg-Cu alloys and about 35 μm for the Mg-Ni alloys. A more detailed description of the equipment used is given in Ref.[55].

Directly after the melt spinning, the specimens were stored in argon atmosphere at liquid nitrogen temperature. This was needed to avoid crystallisation possibly taking place at

room temperature. For all measurements described in the following it was made sure that crystallisation at room temperature did not influence the results obtained by keeping the time between the removal of the specimens from the liquid nitrogen dewar and the measurement short (typically one day).

The ribbons produced were shown to be amorphous by Guinier X-ray diffraction: no crystal reflections were visible. The composition of the ribbons was determined by chemical analysis (inductive coupled plasma optical emission spectrometry); the results of this determination were in agreement with the initially weighed amounts of the components.

5.3.3 Differential Scanning Calorimetry

The differential scanning calorimeter (DSC) measurements were carried out using power compensated Perkin Elmer DSC's: a DSC-7 and a Pyris-1. As a function of time, the difference between the heating powers to keep the reference and sample at the same temperature was recorded, upon subjecting reference and sample to a certain temperature-time program. The temperature-time programs in this work involved both isothermal and isochronal (i.e. at constant heating rate) anneals. The applied heating rates for the isochronal experiments were 2.5, 5, 10, 20 and 40 K/min. Sample and reference pan were made of aluminium. The sample pan was filled with cut alloy ribbons, and sealed with an aluminium cover. The reference pan was provided with two aluminium covers, in order to obtain a heat capacity of the reference comparable to that of the sample. A protective gas atmosphere of pure argon was employed. Per sample, two DSC runs were performed; the second run (then with the specimen in its crystalline state) served as an in situ recording of the baseline.

The temperature and the heat flow were calibrated by measuring the melting temperatures and the heats of fusion of pure In, Sn and Zn.

5.3.3.1 Baseline correction

In the *isothermal* annealing experiments, a baseline drift was observed over a very long time range. The baseline was determined by fitting an exponential decay function to the measured signal outside the time range where the crystallisation occurred.

In the *isochronal* annealing experiments, two baseline corrections were performed. The first correction is apparatus specific, and the second correction is specimen specific. Per sample, two identical DSC runs were made successively. The second run, then with the specimen in its crystalline state, served as an in situ recording of the baseline. Subtraction of this baseline from the first run realised the correction for the apparatus specific baseline shift, and as a result, the measurement curve was obtained.

During the crystallisation (in the first run), the state of the specimen changed from undercooled melt to crystalline. Hence, in the first run the specific heat of the specimen changed gradually from the specific heat of the undercooled melt to the specific heat of the crystalline compound(s). It was supposed that the overall specific heat of the specimen is given by the linear interpolation of the specific heats of the undercooled melt and the crystalline compound(s), and thus the overall specific heat is proportional to the fraction crystallised. Then, recognising that the specimen specific baseline is proportional to the specific heat, the second baseline correction is established iteratively:

- (i) An initial linear baseline was determined from the measurement curve in a start and an end point.
- (ii) Integration of the difference between the measurement curve and the baseline gave a signal proportional to the transformed fraction as function of temperature.
- (iii) A new baseline was estimated, by weighted averaging the values of the measurement curve in the start and the end point (see step(i)), using the transformed fraction resulting from step (ii) as weighing factor.
- (iv) Steps (ii) and (iii) were repeated until the difference between the baselines of two subsequent iteration steps was neglectably small.

The fully corrected DSC signal, i.e. after the baseline corrections as explained above, represents the rate of enthalpy uptake by the specimen due to the crystallisation: $d\Delta H/dt$, where ΔH is the enthalpy difference (ΔH is negative for crystallisation, i.e. heat is released).

5.3.4 Data evaluation

The $d\Delta H/dt$ curves as obtained after the full baseline correction procedure (cf. section 5.3.3.1) were integrated, leading to values for the cumulative crystallisation enthalpy $\Delta H(t)$ during the annealing stage. Then the transformed fraction is given by:

$$f(t) \equiv \frac{\Delta H(t)}{\Delta H_{\text{tot}}}, \quad (5.4)$$

where ΔH_{tot} is the total crystallisation enthalpy, as determined from the DSC experiments (ΔH_{tot} and $\Delta H(t)$ are negative here).

5.3.5 Fitting procedure

The kinetic parameters k_0 , Q and n were determined for a specific pre-annealing stage by fitting the kinetic model (cf. section 5.2.2) to the DSC curves as obtained for either the various heating rates (isochronal annealing experiments) or the various holding temperatures

(isothermal annealing experiments), *simultaneously*. The fitting started with an assumed set of values of k_0 , Q and n . Then, using Eqs.(5.1)-(5.3) the transformed fraction f as a function of time t was calculated. The calculated transformed fraction was used to calculate the rate of enthalpy uptake $d\Delta H/dt$ using Eq.(5.4). The least squares difference between the $d\Delta H/dt$ curves from the calculation according to the model and those from the measurements was minimised using a downhill simplex fitting routine [24] by altering the kinetic parameters k_0 , Q and n .

The above described general fitting procedure had specific features for fitting isothermal and isochronal measurements. On fitting the isothermal measurements, ΔH_{tot} was taken as a fourth fitting parameter, because at early stages of the isothermal measurement the measurement signal was affected by imbalance of the temperatures of reference and sample pans, which hindered the direct determination of ΔH_{tot} . Therefore, ΔH_{tot} could only be determined if fitting of the kinetic model was possible, except for measurements at extremely low isothermal holding temperatures, where the crystallisation started after the balance of the temperatures of reference and sample pans had been reached. On fitting the isochronal measurements, minimisation of the least squares difference was carried out with respect to the data for $d\Delta H/dT$ instead of $d\Delta H/dt$, because in this way measurements performed with different heating rates are given equal weight in the least squares minimisation. In cases where overlap of two DSC peaks hindered the determination of ΔH_{tot} for one peak, ΔH_{tot} was taken as a fourth fitting parameter.

5.3.6 X-Ray Diffraction

Isothermal X-ray diffraction (XRD) experiments were performed at elevated temperatures, to record the formation of the crystalline phases in situ. A Philips X'Pert θ - θ diffractometer was used, employing $\text{CuK}\alpha$ radiation. The diffracted beam was detected using a position sensitive detector, which recorded the X-ray intensity within the range of the diffraction angle 2θ from 32° to 44° with a resolution of $\Delta 2\theta=0.015^\circ$ and counting times between 180 and 400 s. The sample ribbons were positioned on the upper side of a tantalum heating filament, with heat conducting paste serving as adhesive and as heat conducting medium. The irradiated area was about 20 mm^2 . The thermocouple for temperature control and measurement was positioned at the bottom side of the tantalum filament, opposite to the specimen.

The fraction of phase α in the specimen, f_{α} , was determined from the peak area of the reflections (numbered 1 to i) of phase α .

$$f_{\alpha}(t, T) = a \sum_i \left(\int_{2\theta_0(i)}^{2\theta_1(i)} I(t, T, 2\theta) d2\theta - \int_{2\theta_0(i)}^{2\theta_1(i)} I(t_0, T_0, 2\theta) d2\theta \right), \quad (5.5)$$

where a is a proportionality factor, $2\theta_0(i)$ and $2\theta_1(i)$ define the range of reflection i , $I(t, T, 2\theta)$ is the measured intensity, and the subscript “0” refers to the specimen in the amorphous state. The proportionality factor a was determined for the equilibrium phases from the known value of f_{α} after completed crystallisation and the corresponding, measured intensities; for determination of a in case of a temporarily present metastable phase, see section 5.4.2. Note that this procedure does not account for texture changes during the course of crystallisation.

For identification of crystalline phases in the ribbons, which were (partly) crystallised during annealing in the DSC equipment, and for confirmation of the ribbons being amorphous after the melt spinning, Guinier (camera) X-ray diffraction experiments using $\text{CuK}\alpha 1$ or $\text{MoK}\alpha 1$ radiation were performed. The identification of an unknown metastable Mg-Ni phase was performed by an ex-situ X-ray diffraction experiment, employing a Siemens D-5005 diffractometer equipped with a parallel beam optic system, and operating with $\text{CuK}\alpha$ radiation.

5.3.7 Transmission Electron Microscopy

Transmission Electron Microscopy (TEM) was performed to investigate the microstructure of the samples at different stages of crystallisation. Electron transparent foils were prepared by directly argon ion milling the sample ribbons. During milling, liquid nitrogen cooling was applied, but, nonetheless, the samples heated up to about 350 K (as assessed from the stage of crystallisation of the Mg-Cu alloys after milling). Crystallisation of the Mg-Cu alloys thus took place during the ion milling. The Mg-Ni alloys were crystallised in the DSC prior to ion milling.

The TEM measurements were carried out using a Zeiss EM 912 Omega transmission electron microscope. Electron Energy Loss Spectra were recorded for two-dimensional (qualitative) elemental mapping of the micrographs.

5.4 Results and evaluation

5.4.1 Differential Scanning Calorimetry

5.4.1.1 Isochronal DSC

Isochronal DSC scans pertaining to the crystallisation of all alloys investigated (Fig.5.2) show that in all cases the crystallisation took place in two stages (the least distinct for the

Mg_{82.0}Ni_{18.0} alloy). This contrasts with the expectations for, in particular, the eutectic alloys where one may expect that both product phases, expected to be Mg and Mg₂X (see Fig.5.1), crystallise simultaneously in one step. Further, the two Mg-Ni alloys, in contrast with the two Mg-Cu alloys, show a striking difference in the corresponding DSC curves, although the difference in alloy composition is only small.

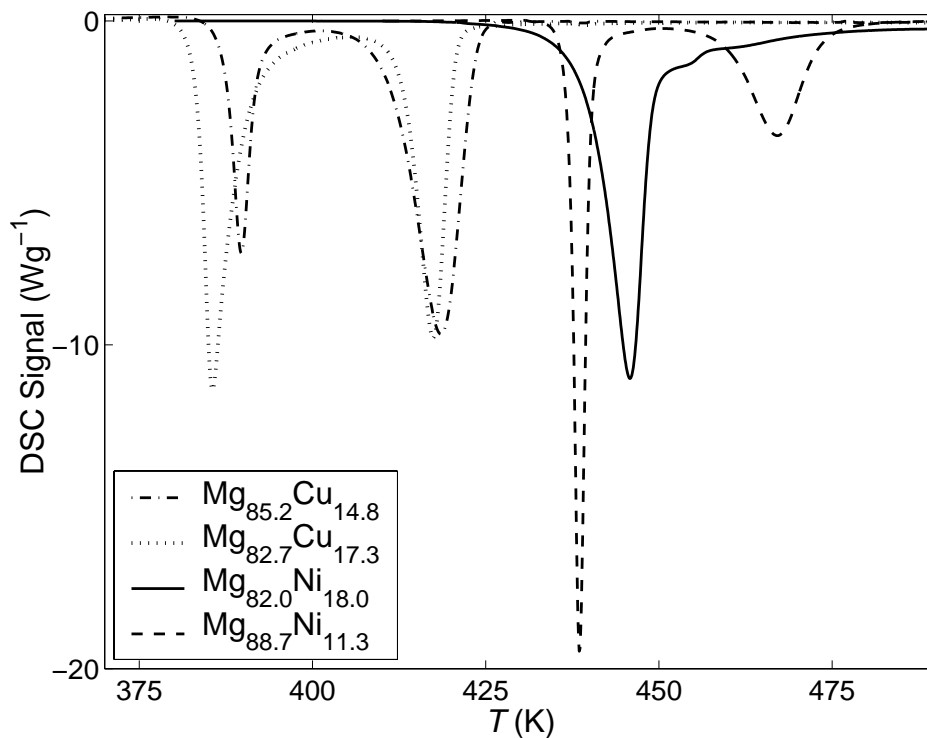


Fig.5.2 Isochronal DSC measurements recorded with a heating rate of 20 K/min for all alloys investigated. For this figure, the only baseline correction applied, is subtraction of the second scan (with the fully crystallised specimen) from the first measurement scan (i.e. the crystallisation scan; cf. section 5.3.3.1).

In order to identify the peaks observed in the DSC scans, XRD-Guinier measurements were performed, after (partially) completed crystallisation. If a large enough volume of crystalline phase is present (say >1-5 vol.%), and the individual particles of this phase are large enough (no very strong diffraction line broadening), the phase can be detected by the occurrence of peaks in the diffraction patterns. For the above DSC scans, the phases detected after completed crystallisation were the Mg and the Mg₂X (X=Cu or Ni) compounds.

At a stage of crystallisation corresponding to immediately after recording the first DSC peak of the (eutectic) Mg_{85.5}Cu_{14.5} alloy, only the Mg-phase was detected. A similar result was *not* obtained for the (off-eutectic) Mg_{82.7}Cu_{17.3} alloy: directly after recording the first DSC peak both phases Mg and Mg₂Cu were present.

At a stage of crystallisation corresponding to immediately after recording the first DSC peak of the (eutectic) $\text{Mg}_{88.7}\text{Ni}_{11.3}$ alloy, the Mg-phase and a metastable phase (identified in this project as $\text{Mg}_{-5.5}\text{Ni}$, cf. section 5.4.2) were detected. The (off-eutectic) $\text{Mg}_{82.0}\text{Ni}_{18.0}$ alloy crystallised mainly in one step (cf. Fig.5.2). Immediately after recording the first DSC peak, but before the second, very small DSC peak occurred, both stable phases and a very small amount of the metastable $\text{Mg}_{-5.5}\text{Ni}$ phase were present.

Fitting of the kinetic model (cf. section 5.2.2) to the first peak in the isochronal scans was impossible for all alloys investigated. This can be ascribed to the occurrence of a type of nucleation incompatible with JMA kinetics (e.g. non steady state nucleation [25]). Further, the first peak recorded upon isochronal annealing for various heating rates may not be representative for an isokinetic transformation: the isothermal anneals (see section 5.4.1.2) exhibit a transformation mechanism at low temperatures that is different from the one at high temperatures. For the $\text{Mg}_{82.7}\text{Cu}_{11.3}$ alloy, the second peak in the isochronal scans could be fitted with the kinetic model, (see Table 5.1); for discussion see section 5.5.

5.4.1.2 Isothermal DSC

Isothermal anneals performed for the Mg-Cu alloys revealed that the two crystallisation peaks (see above discussion of the isochronal anneals) gradually became one broad peak at low temperature (Figs.5.3 and 5.4). Clearly, the transformation mechanism depends on the temperature.

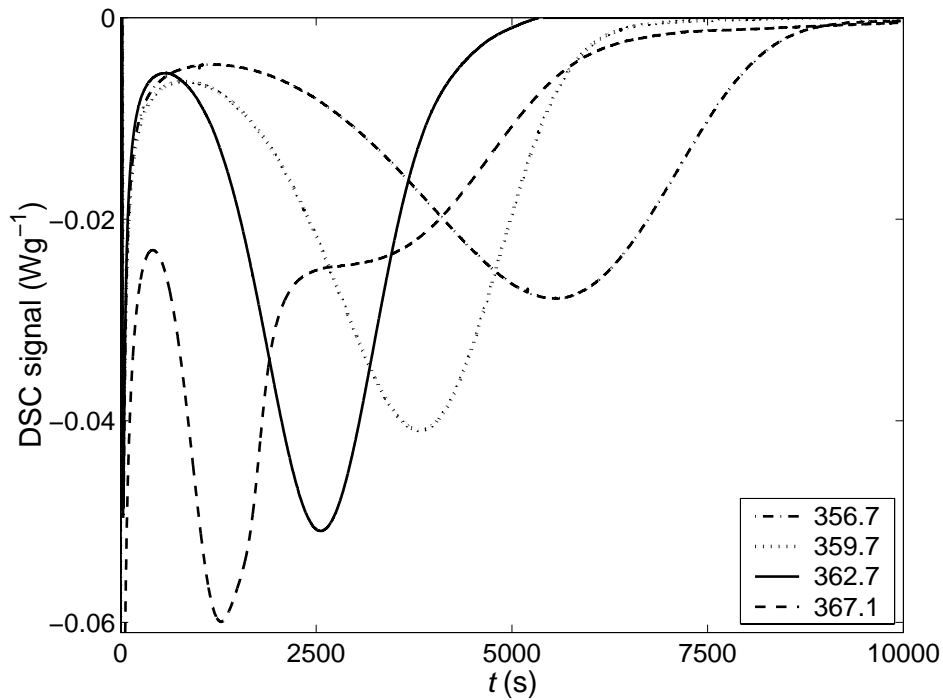


Fig.5.3 Isothermal DSC scans of alloy $\text{Mg}_{82.7}\text{Cu}_{17.3}$ at the temperatures indicated. No baseline correction was applied. The DSC signal (i.e. the ordinate in the figure) was shifted for each scan such that after the crystallisation was completed, the DSC signal equals zero.

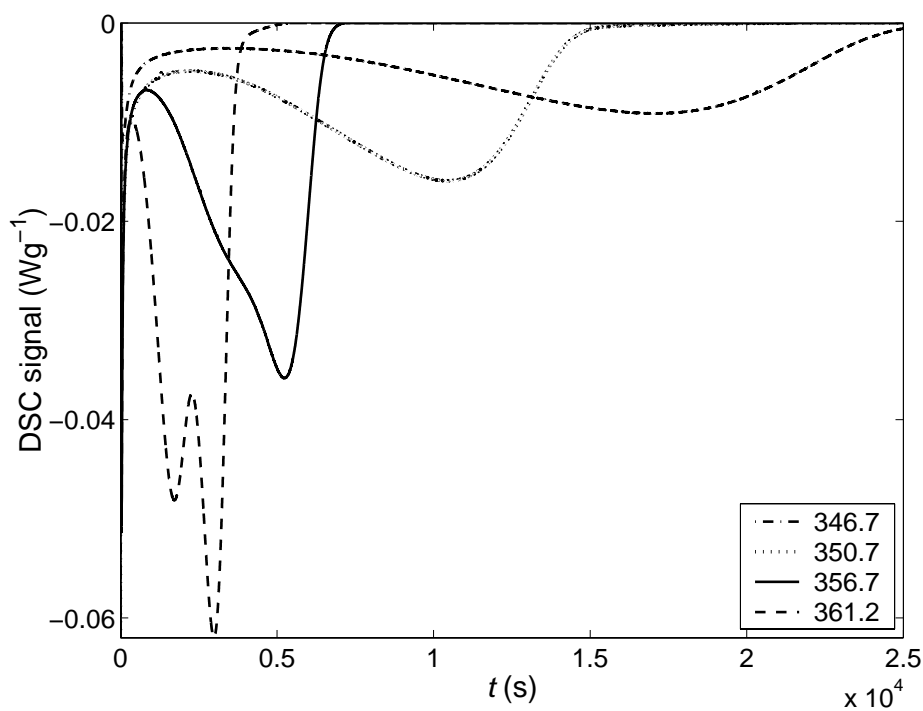


Fig.5.4 Isothermal DSC scans of alloy $\text{Mg}_{85.5}\text{Cu}_{14.5}$ at the temperatures indicated. No baseline correction was applied. The DSC signal (i.e. the ordinate in the figure) was shifted for each scan such that after the crystallisation was completed, the DSC signal equals zero.

Therefore, measurements at temperatures that differ much cannot be considered as isokinetic. If only measurements in the lower temperature range are considered, where only one transformation peak is observed, the transformation may be considered as isokinetic in that temperature range. For these measurements the kinetic model (cf. Eqs.(5.1),(5.2)and (5.3)) could be fitted well to the peaks (see Fig.5.5).

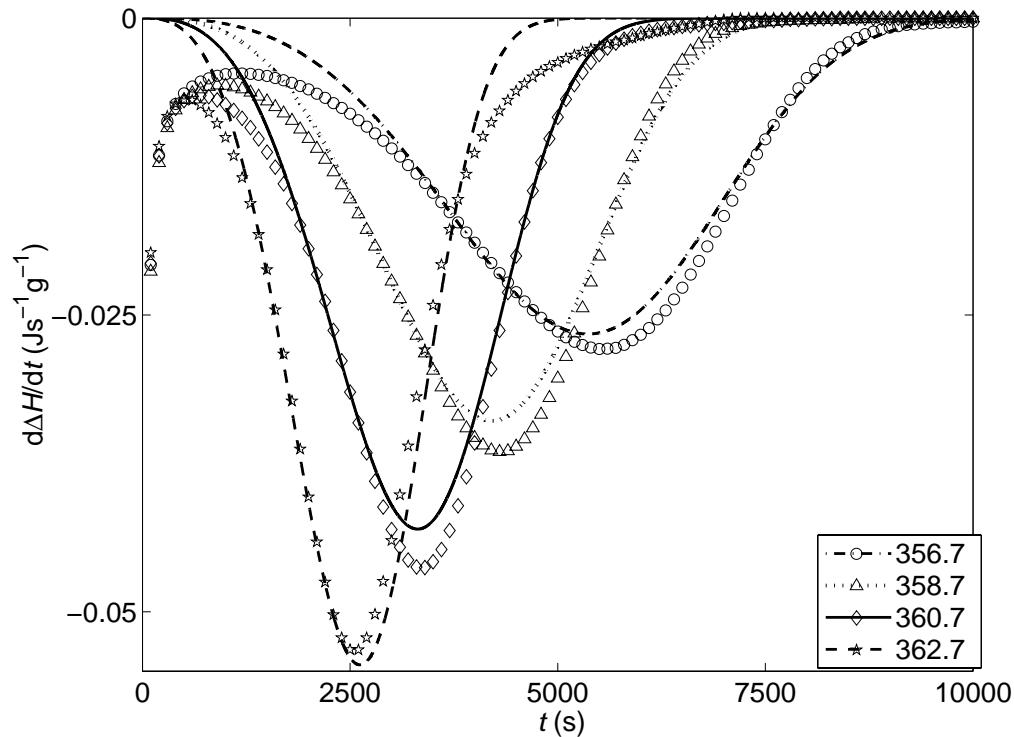


Fig.5.5 Isothermal DSC scans of $Mg_{82.7}Cu_{17.3}$ at the indicated temperatures, as measured (symbols) and as fitted (lines). For the fit, the initial part of the measurement has not been taken into account, i.e. the first 1500 s.

The kinetic parameters (i.e. k_0 , Q , and n) for both Mg-Cu alloys were determined by fitting (cf. section 5.3.5) the kinetic model to all considered isothermal measurements for one alloy *simultaneously*. The results have been gathered in Table 5.1.

The enthalpy uptake due to completed crystallisation of the Mg-Cu alloys (= area under the DSC curves) did not change significantly as function of temperature and was equal to the corresponding value observed upon isochronal annealing of the same alloy (see Table 5.1).

Table 5.1 Kinetic parameters n , Q and k_0 as determined by fitting the kinetic model (Eqs.(5.1)-(5.3)). The kinetic parameters have only been given if good fits were possible. Further, the enthalpy uptake due to full crystallisation, ΔH_{tot} has been given for all cases.

Alloy	experiment	k_0 (s^{-1})	Q (kJ mol^{-1})	n	ΔH_{tot} (J g^{-1})
Mg _{82.7} Cu _{17.3}	isothermal 356-363K	$1.37 \cdot 10^{15}$	129	3.8	-106*
	isothermal 373-378K	-	-	-	-111
	isochronal, just second peak	$1.07 \cdot 10^{14}$	125	3.5	-85*
	isochronal, both peaks	-	-	-	-112
Mg _{85.5} Cu _{14.5}	isothermal 346-351K	$1.83 \cdot 10^{15}$	130	4.0	-108*
	isothermal 363-375K	-	-	-	-120
	isochronal both peaks	-	-	-	-120
Mg _{82.0} Ni _{18.0}	isothermal 401-410K	$9.33 \cdot 10^{15}$	150	4.1	-86*
	isochronal	-	-	-	-110
	isochronal second peak after isothermal first peak	-	-	-	-1
Mg _{88.7} Ni _{11.3}	isochronal	-	-	-	-108
	isothermal 404-423K	-	-	-	-65
	isothermal 433-448K	-	-	-	-
	isochronal second peak after isothermal first peak	$3.55 \cdot 10^{15}$	157	1.5	-25

*determined by fitting (see section 5.3.5).

The crystallisation of the alloy Mg_{82.0}Ni_{18.0} has also been measured isothermally. Fitting of the kinetic model was possible (Fig.5.6).

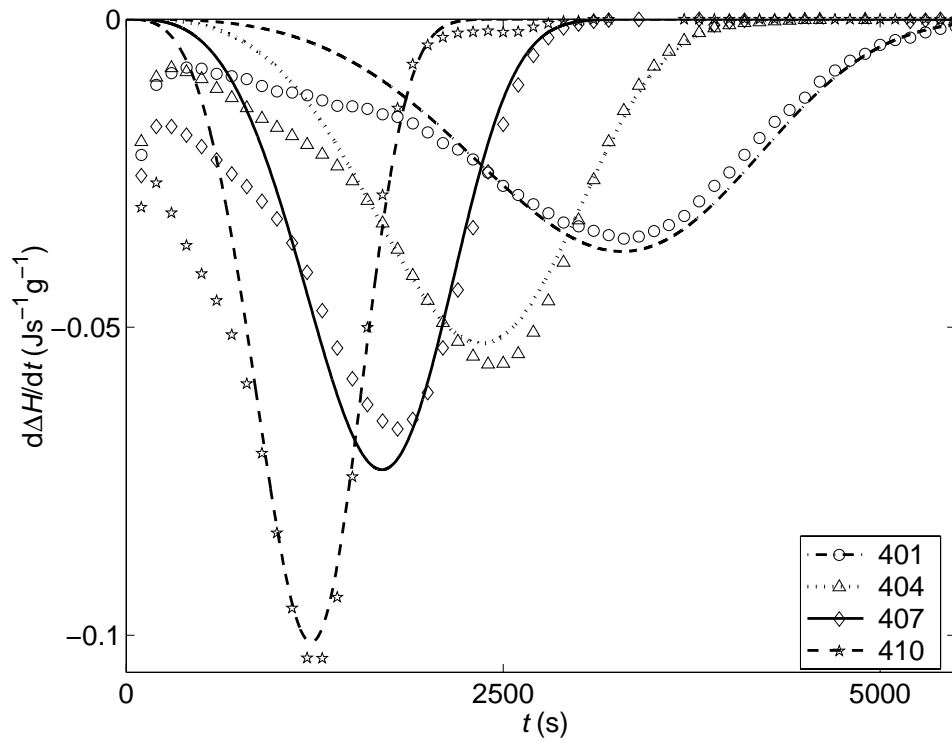


Fig.5.6 Isothermal DSC scans of $\text{Mg}_{82.0}\text{Ni}_{18.0}$ at the indicated temperatures, as measured (symbols) and as fitted (lines). For the fit, the initial part of the measurement has not been taken into account, i.e. the first 1600, 900, 500 and 400 s for the temperatures 401, 404, 407 and 410 K, respectively.

The resulting values of the fitting parameters have been given in Table 5.1.

During isothermal annealing of the eutectic alloy $\text{Mg}_{88.7}\text{Ni}_{11.3}$ at 433-448 K, two crystallisation peaks appear. At temperatures between 404 and 423 K, isothermal annealing of the alloy $\text{Mg}_{88.7}\text{Ni}_{11.3}$ resulted in only one crystallisation peak. In the latter case, XRD-measurements of the specimen after completed isothermal annealing showed that crystalline Mg and a metastable phase (of composition $\text{Mg}_{-5.5}\text{Ni}$, as determined in this project, cf. section 5.4.2) were present (see Fig.5.7)

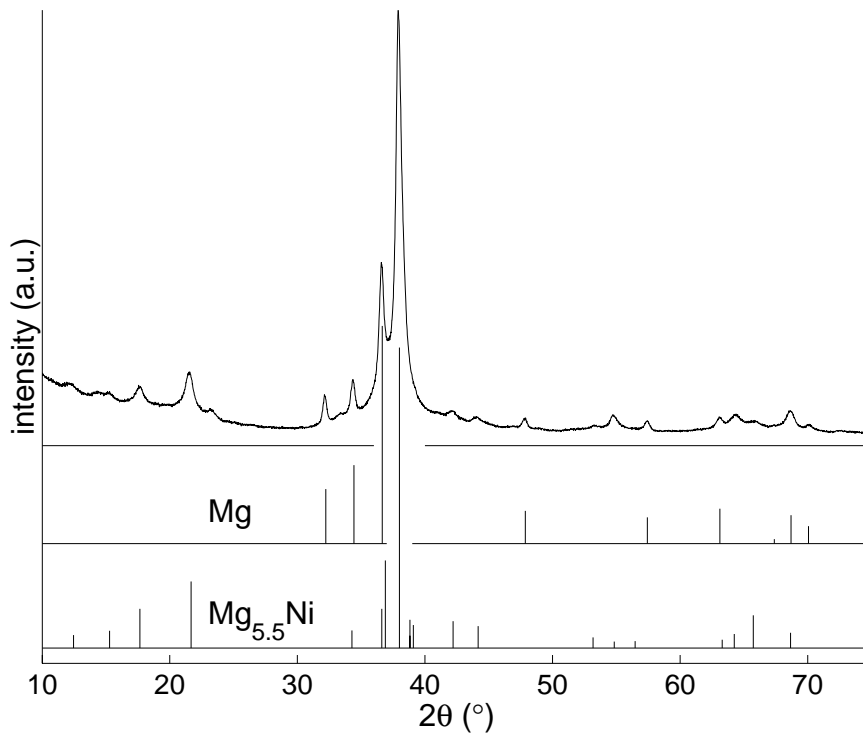


Fig.5.7 X-ray diffractogram (Cu $K\alpha$ radiation) of the $Mg_{88.7}Ni_{11.3}$ alloy after completed isothermal crystallisation at 423K. Depicted are the measured scan (upper part) and the peak positions and relative intensities of Mg (Ref.[56]) and $Mg_{5.5}Ni$ (calculated adopting the Mg_6Pd structure type and a lattice constant of 20.09 Å).

The observed diffraction pattern of the additional phase shows strong similarities with diffraction patterns simulated in this work, using the program LAZY PULVERIX [57], that were obtained for $Mg_{5.5}Ni$ (hypothetically) crystallising in the structure types of Mg_6Pd , $Mg_{44}Rh_7$, $Fe_{11}Zn_{39}$ and Na_6Ti [58]. These structure types exhibit considerable structural similarities [59, 60], as expressed by a common cubic space group symmetry $F\bar{4}3m$ and similar lattice constants of about 20 Å. As an example a simulated pattern for Mg_6Ni with Mg_6Pd type structure is shown in Fig.5.7, giving a reasonable lattice constant of 20.09 Å (Mg_6Pd : 20.108 Å [58]) and relative reflection intensities that agree rather well with the measured diffractogram (especially note the very strong reflection at $2\theta=38^\circ$; this reflection has been observed before during crystallisation of Mg-Ni alloys [43]). However, due to specimen inherent, significant, (also asymmetric) diffraction line broadening of the reflections of the $Mg_{5.5}Ni$ -phase, it is not possible to choose between the mentioned structure types.

5.4.1.3 Combined isothermal/isochronal measurements

As remarked in section 5.4.1.2, completed isothermal annealing of the alloy $Mg_{88.7}Ni_{11.3}$ at temperatures of 404-423 K resulted in a large amount of the metastable $Mg_{5.5}Ni$ phase. The

subsequent transformation of the metastable phase to the stable phases was realised by subsequent isochronal DSC anneals (Fig.5.8), as confirmed by XRD-Guinier measurements.

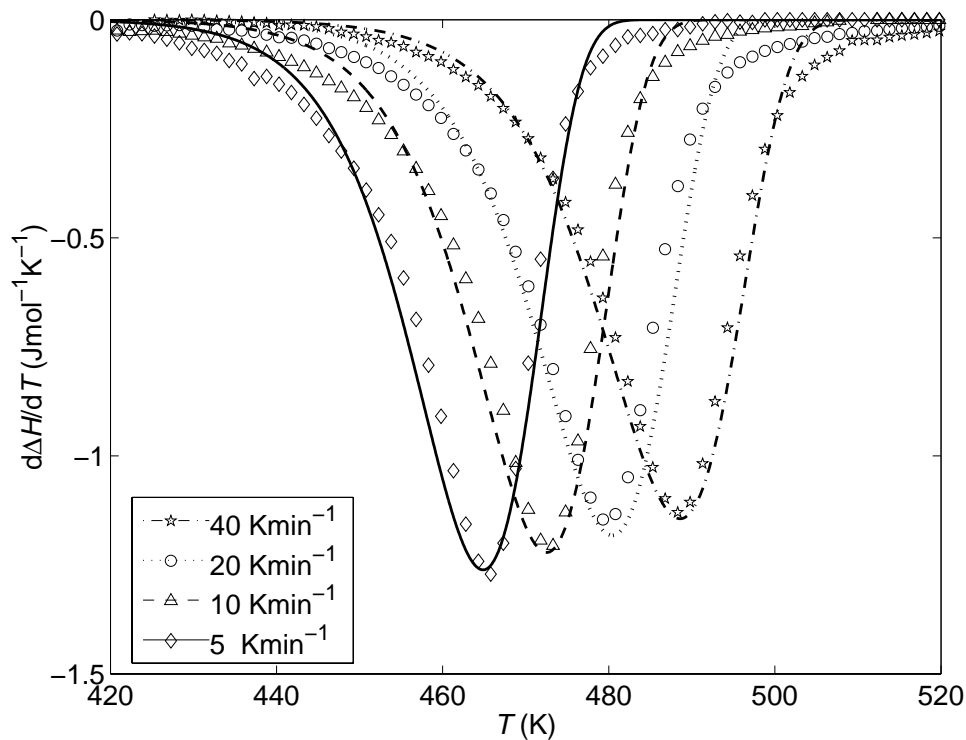


Fig.5.8 Rate of enthalpy uptake (due to crystallisation) divided by the heating rate of the isochronal DSC scans as measured for $Mg_{88.7}Ni_{11.3}$ using the indicated heating rates after an isothermal anneal of 3600 s at 423 K; as measured (symbols) and as fitted using the kinetic model (lines).

The kinetic model (Eqs.(5.1)-(5.3)) could be fitted very well, simultaneously, to the isochronal measurements for various heating rates, leading to values for the fitting parameters as given in Table 5.1.

5.4.2 In situ XRD

The course of the formation of the separate phases was directly established using isothermal, in-situ diffractometer measurements for the four amorphous alloys investigated in this study. The result of such experiments is a sequence of diffractograms, which have been recorded subsequently, revealing the formation of crystalline phases in the specimen. As an example, see the diffractograms recorded for the alloy $Mg_{88.7}Ni_{11.3}$ in Fig.5.9. In this particular case a temperature-time programme was applied that involved a cumulative series of isothermal anneals, as indicated in Fig.5.13. Such diffractograms were recorded for all four alloys, and were evaluated quantitatively as described in section 5.3.6.

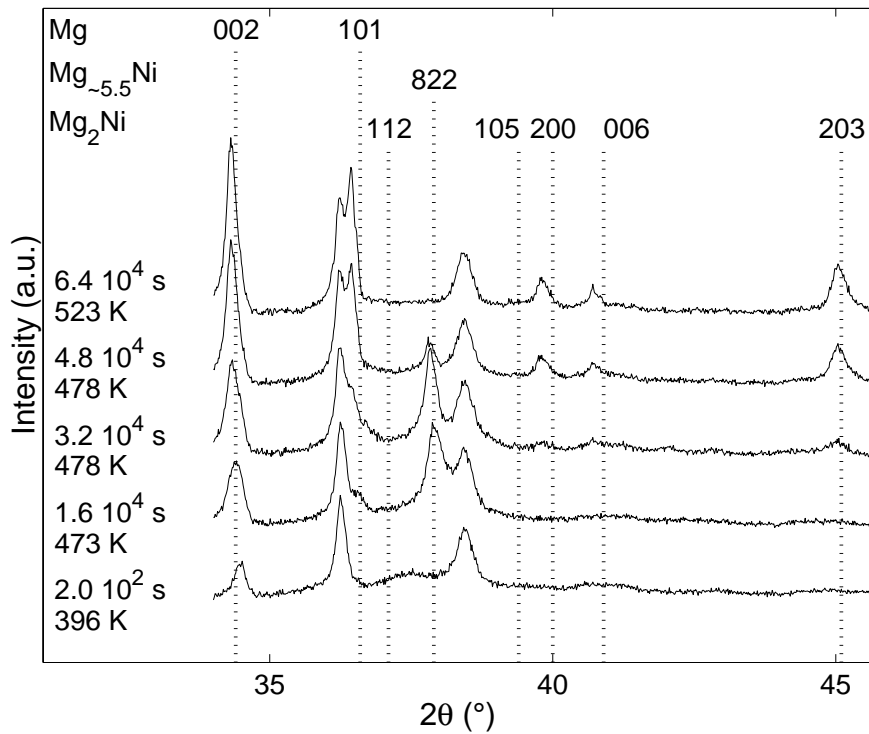


Fig.5.9 Diffractograms ($CuK\alpha$ radiation) of the alloy $Mg_{88.7}Ni_{11.3}$ recorded in-situ in a series of cumulative isothermal anneals, during crystallisation at instantaneous temperatures as indicated. The positions of the reflections of the various phases have been indicated by the vertical lines; peaks unidentified in the figure could be ascribed to the heat conducting paste (peaks at 34.4 and $36.4^{\circ}2\theta$) and to the Ta filament (peak at $38.5^{\circ}2\theta$).

In the first scan in Fig.5.9 (i.e. after 200 s), some reflections are visible which cannot be due to crystalline product phases at this stage: by comparing with measurements of the bare tantalum filament and the filament covered with the heat conducting paste, it became clear that the first two peaks (at 34.4 and $36.4^{\circ}2\theta$) are due to the heat conducting paste and that the third peak at $38.5^{\circ}2\theta$ is a 110 Ta reflection coming from the filament. The very broad humps at $37^{\circ}2\theta$ and $41^{\circ}2\theta$ are reflections from amorphous material, i.e. they originate from the specimen and/or from the heat conducting paste.

Using Eq.(5.5), the amounts of Mg and Mg_2Cu phases developing in the Mg-Cu alloys were calculated from the measured diffractograms as a function of time (and temperature): see Figs.5.10 and 5.11. For the calculation, the 002 and 101 reflections of the Mg phase and 080 and 440 reflections of the Mg_2Cu phase were used. The atomic fraction of the phases has been defined as the number of atoms present in a phase divided by the total number of atoms in the specimen. The equilibrium atomic fractions (end values) of the phases were calculated using the overall composition and the composition of the two equilibrium phases, and have been

indicated in the figures.

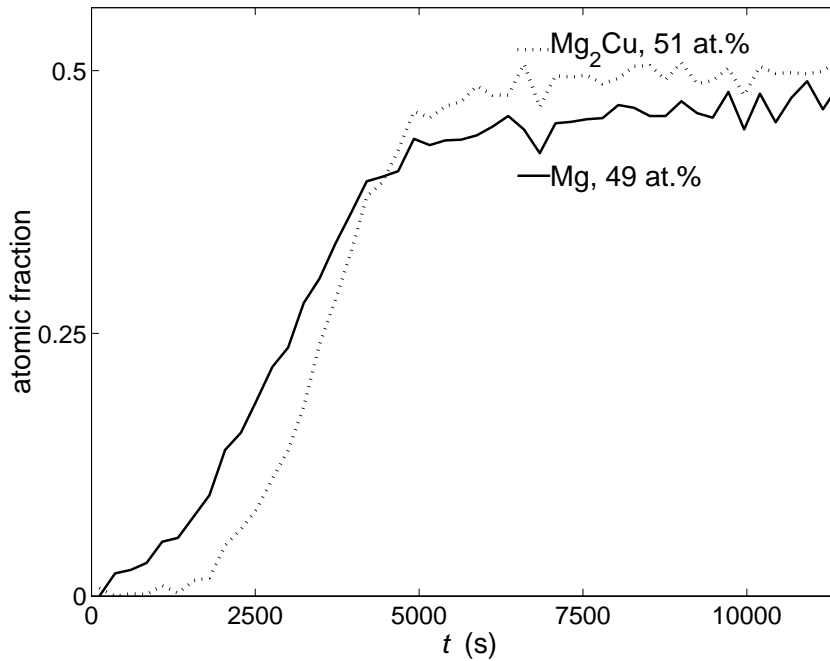


Fig.5.10 The atomic fractions of crystalline Mg and crystalline Mg₂Cu developing as a function of time at 359 K in the initially amorphous alloy Mg₈₃Cu₁₇. Results obtained from in situ XRD. The equilibrium atomic fractions (end values) of the phases have been indicated in the figure.

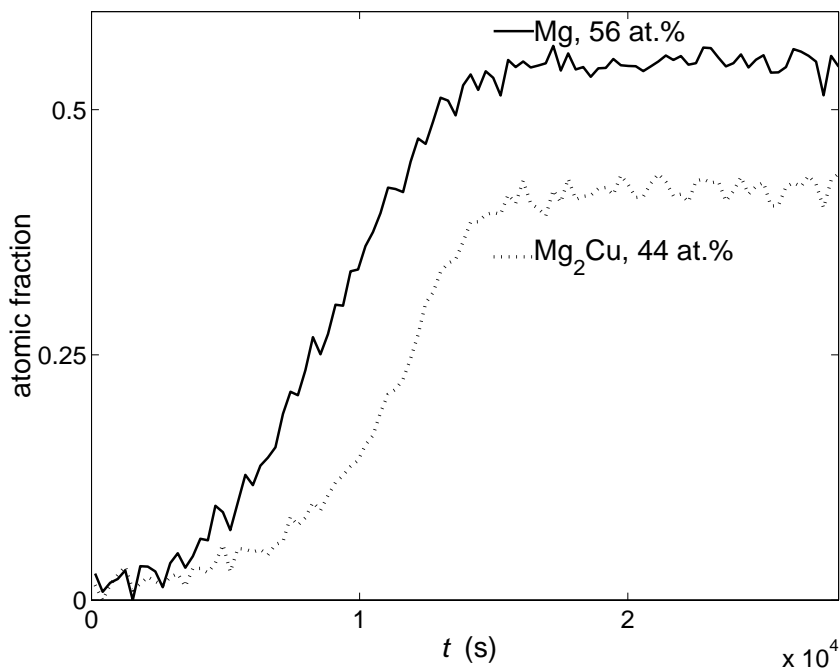


Fig.5.11 The atomic fractions of crystalline Mg and crystalline Mg₂Cu developing as a function of time at 351 K in the initially amorphous alloy Mg_{85.5}Cu_{14.5}. Results obtained from in situ XRD. The equilibrium atomic fractions (end values) of the phases have been indicated in the figure.

It clearly follows from Figs.5.10 and 5.11 that in the initially amorphous Mg-Cu alloys both crystalline product phases, Mg and Mg₂Cu, formed simultaneously during the crystallisation.

Similarly, the amounts of the Mg, Mg₂Ni and Mg_{-5.5}Ni phases developing in the Mg-Ni alloys during crystallisation were calculated as function of time (and temperature); see Figs.5.12 and 5.13. For the calculation, the 002 and 101 reflections of the Mg phase, the 200 and 203 reflections of the Mg₂Ni phase, and the 822 reflection of the Mg_{-5.5}Ni phase (indexed as Mg₆Pd structure type) were used.

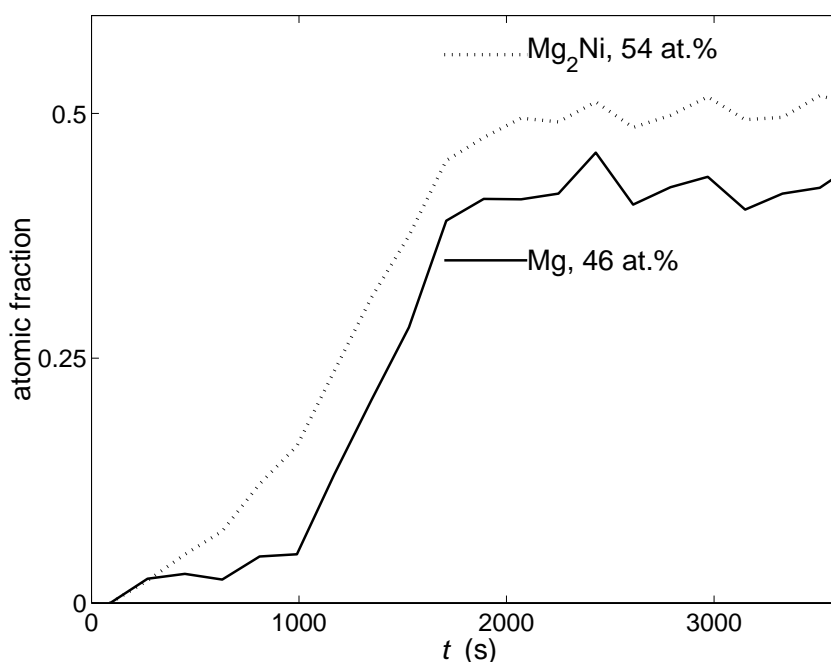


Fig.5.12 The atomic fraction of crystalline Mg and Mg₂Ni as a function of time at 400 K in the initially amorphous alloy Mg_{82.0}Ni_{18.0}. Results obtained from in situ XRD measurements. The equilibrium atomic fractions (end values) of the phases have been indicated in the figure.

It clearly follows from Fig.5.12 that in the Mg_{82.0}Ni_{18.0} alloy, both crystalline product phases, Mg and Mg₂Ni, formed simultaneously during the crystallisation at 400 K; formation of the metastable phase Mg_{-5.5}Ni was not observed during the in-situ XRD measurement.

The alloy Mg_{88.7}Ni_{11.3} (Fig.5.13) was subjected to a cumulative series of isothermal anneals; the subsequent holding temperatures and the corresponding time ranges have been indicated in Fig.5.13. In addition to the two stable product phases, in this alloy, the metastable phase, Mg_{-5.5}Ni, developed, as illustrated by the occurrence of a strong diffraction peak at 37.9 °2θ (CuKα radiation, cf. Fig.5.9). Recognising that in the end stage only the two equilibrium phases, Mg and Mg₂Ni occur, and that therefore their equilibrium atomic fractions are known (see above), independent of the occurrence of a metastable phase, the

atomic fractions of crystalline Mg and Mg_2Ni were calculated according to Eq.(5.5). Then the composition of the metastable phase was determined as $\text{Mg}_{\sim 5.5}\text{Ni}$, supposing that beyond $1.2 \cdot 10^4$ s the specimen does not contain the amorphous phase any more and, thus, the specimen of known overall composition is then composed only of Mg, Mg_2Ni and if present, the metastable phase. On this same basis, the value of a for the metastable phase (cf. Eq.(5.5)) was determined. Justification for the supposition that no amorphous phase was present beyond $1.2 \cdot 10^4$ s, was obtained from comparison of the values for the atomic fraction $\text{Mg}_{\sim 5.5}\text{Ni}$ calculated in two ways, (i) according to Eq.(5.5) and (ii) according to $f_{\text{Mg}_{\sim 5.5}\text{Ni}} = 1 - f_{\text{Mg}} - f_{\text{Mg}_2\text{Ni}}$; these values are practically equal from $t = 1.2 \cdot 10^4$ s on.

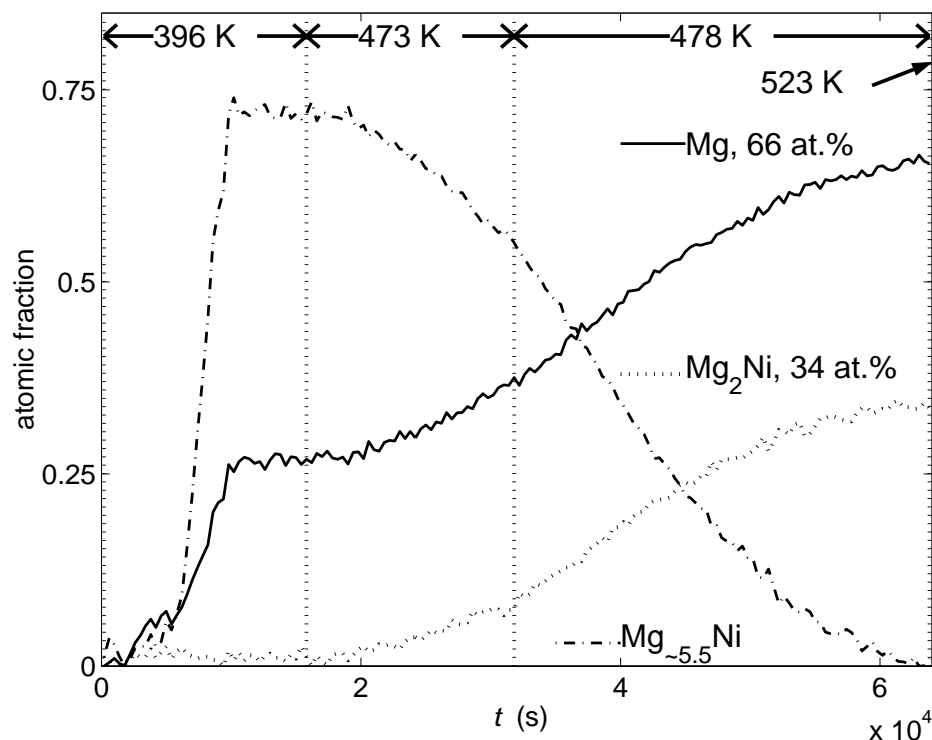


Fig.5.13 The atomic fractions of the crystalline phases Mg, Mg_2Ni and $\text{Mg}_{\sim 5.5}\text{Ni}$, developing as a function of time during a cumulative series of isothermal anneals at instantaneous temperatures as indicated in the figure, in the initially amorphous alloy $\text{Mg}_{88.7}\text{Ni}_{11.3}$. Results obtained from in situ XRD. The equilibrium atomic fractions (end values) of the thermodynamic stable phases have been indicated in the figure.

5.4.3 TEM

The microstructure of the crystallised alloys was examined by TEM. The $\text{Mg}_{83.0}\text{Cu}_{17.0}$ alloy crystallised during the ion-milling, by unavoidable, milling induced annealing, although liquid nitrogen cooling was applied (cf. section 5.3.7). Different annealing temperatures were effectively realised by using different acceleration voltages of the argon sputter ions used in

the ion milling. After crystallisation at the lower temperature (corresponding to 3.5 kV acceleration voltage) had taken place, an extremely fine lamellar structure was observed (Fig.5.14a). The lamellae thickness equals 10-15 nm. If the crystallisation temperature is increased (corresponding to 5-6 kV acceleration voltage), the structure is coarser and less lamellar (Fig.5.14b). The microstructure in 5.14b can best be described as a mixture of equiaxed and lamellar eutectic morphologies. In the EELS composition maps, on the right-hand side of the Figs.5.14 the relative amounts of Cu (upper part) and of Mg (lower part) are illustrated: a light area corresponds to a relatively high concentration. As only two product phases occur in the Mg-Cu system, the phase with relatively high concentration of Cu must be Mg_2Cu .

The alloy $Mg_{85.5}Cu_{14.5}$ crystallised at the higher temperature (corresponding to 5-6 kV acceleration voltage), resulting in about the same microstructure (Fig.5.15) as observed for the $Mg_{82.7}Cu_{17.3}$ alloy that crystallised at about the same temperature(Fig.5.14b).

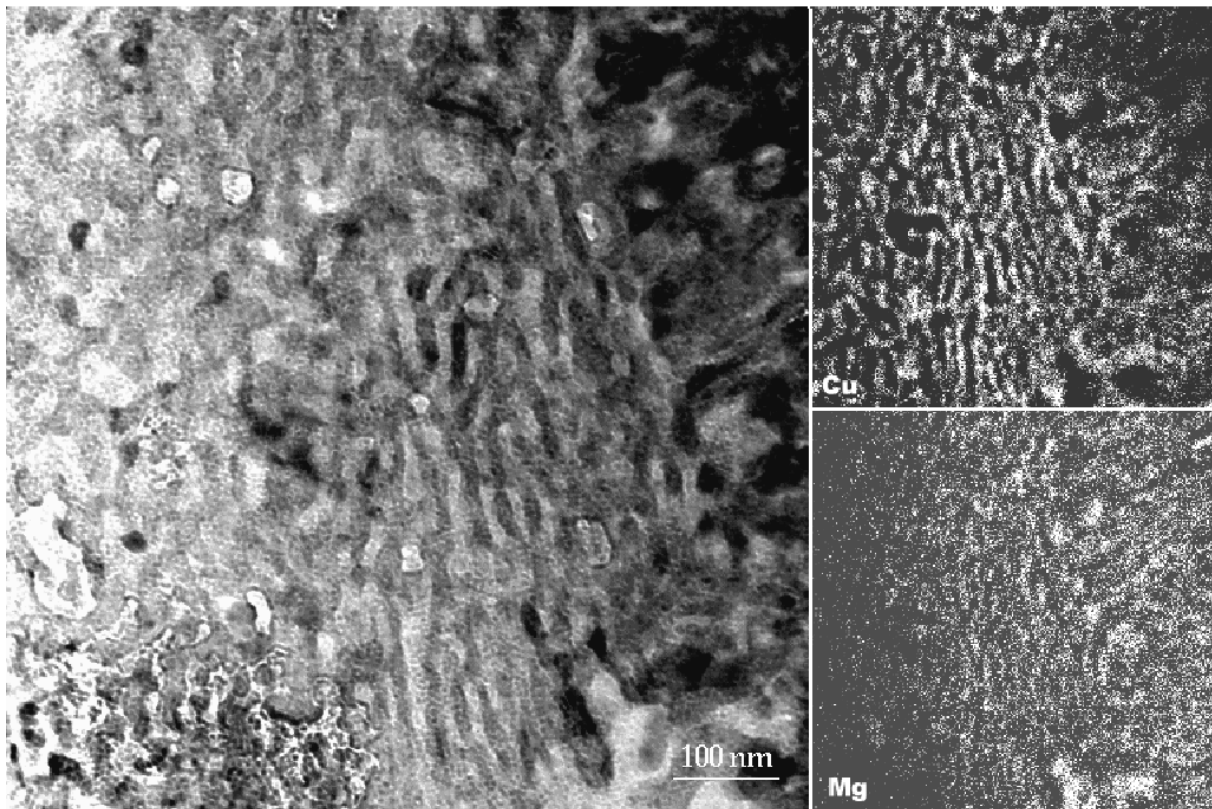


Fig.5.14a Bright field electron micrograph and EELS elemental maps (Cu and Mg) of the $Mg_{82.7}Cu_{17.3}$ alloy after ion milling with 3.5 kV argon ions.

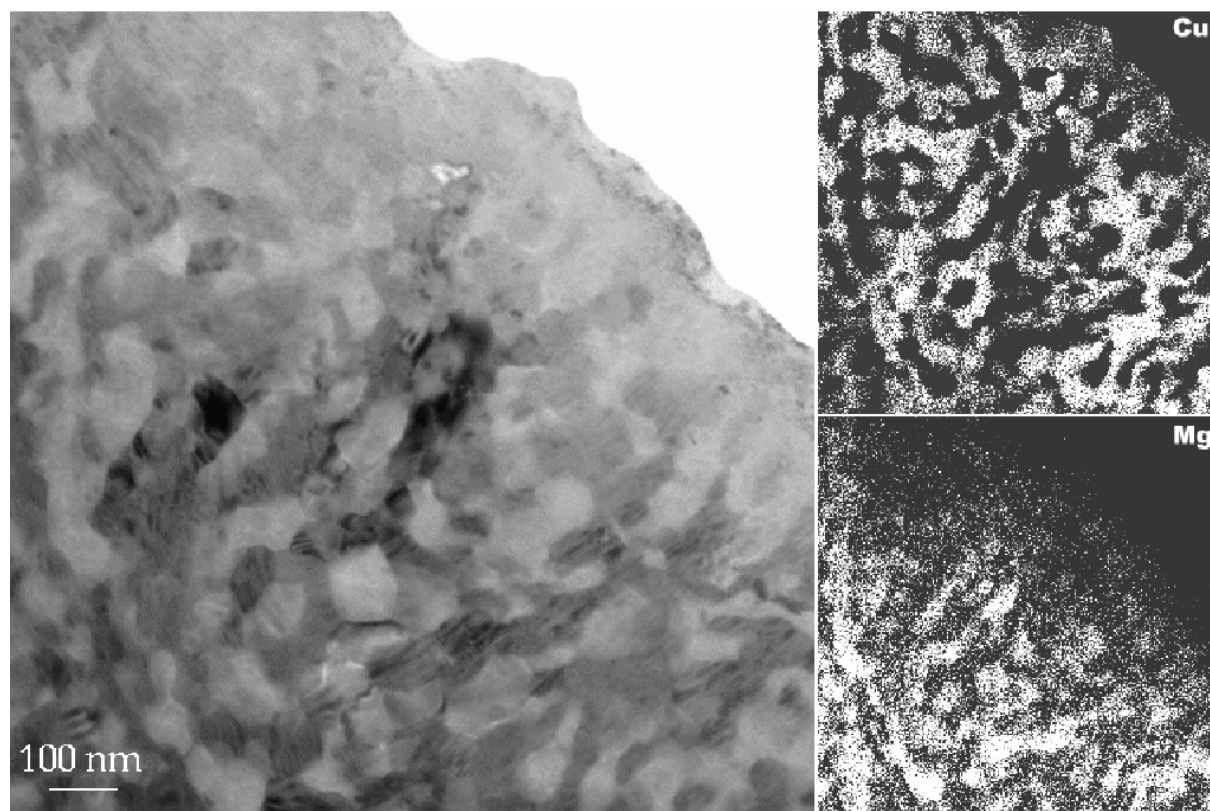


Fig.5.14b Bright field electron micrograph and EELS elemental maps (Cu and Mg) of the $Mg_{82.7}Cu_{17.3}$ alloy after ion milling with 5-6 kV argon ions.

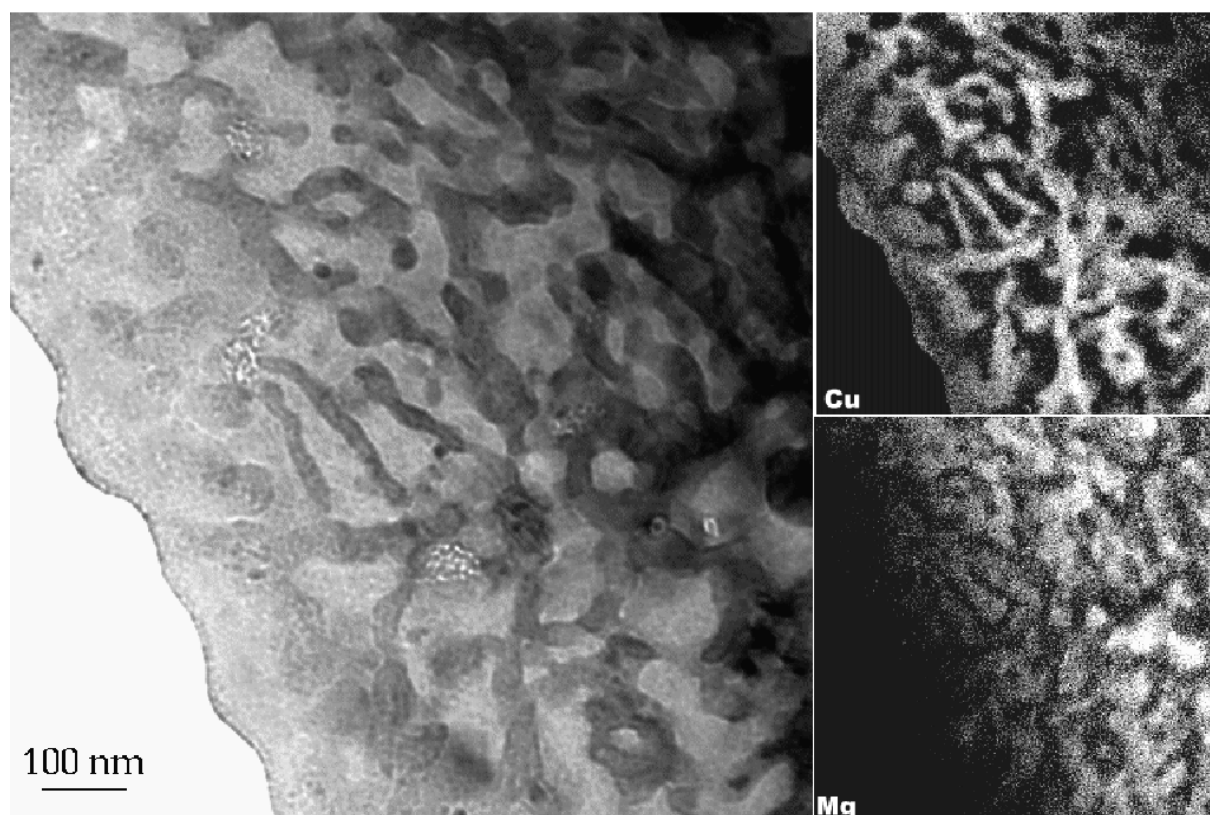


Fig.5.15 Bright field electron micrograph and EELS elemental maps (Cu and Mg) of the $Mg_{85.5}Cu_{14.5}$ alloy after ion milling with 5-6 kV argon ions.

TEM specimens of the alloy $\text{Mg}_{82.0}\text{Ni}_{18.0}$ were prepared by crystallising isothermally in the DSC at 401 K and 448 K, and consecutive ion milling under liquid nitrogen cooling with an acceleration voltage of 5 kV; see Figs.5.16.

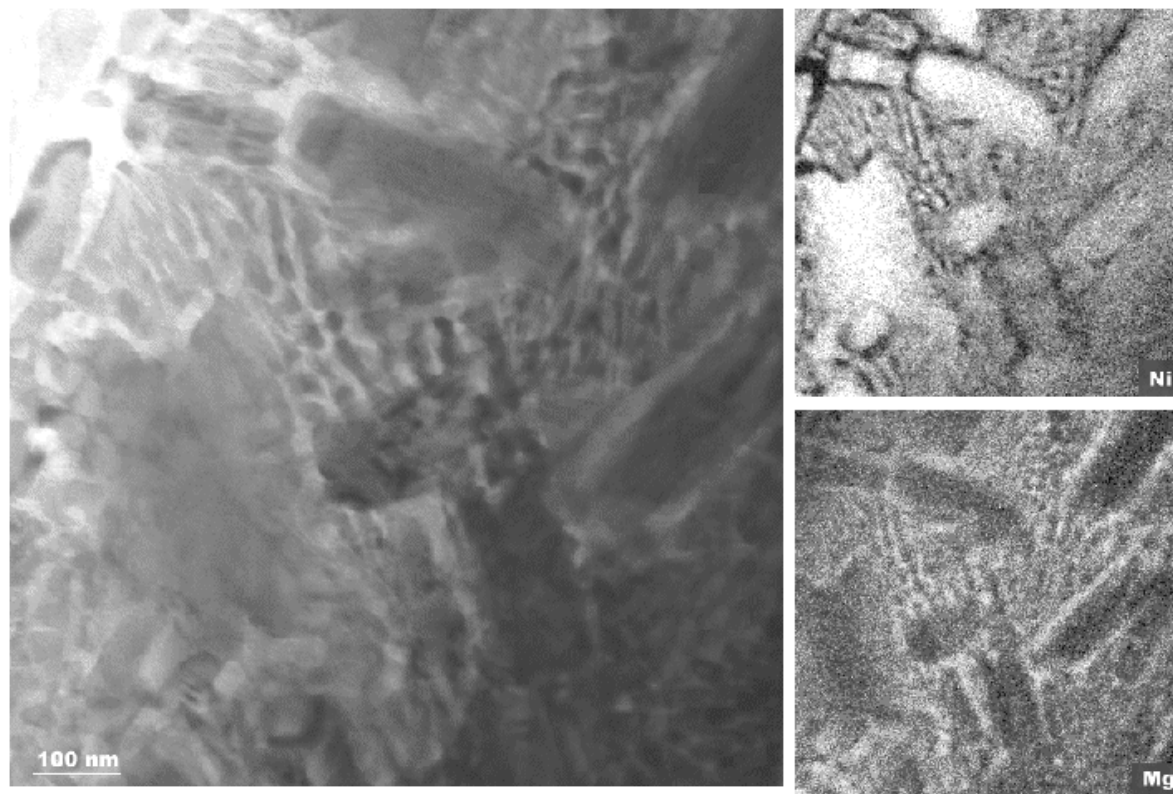


Fig.5.16a Bright field electron micrographs and EELS elemental maps (Ni and Mg) of the $\text{Mg}_{82.0}\text{Ni}_{18.0}$ alloy after annealing at 401 K.

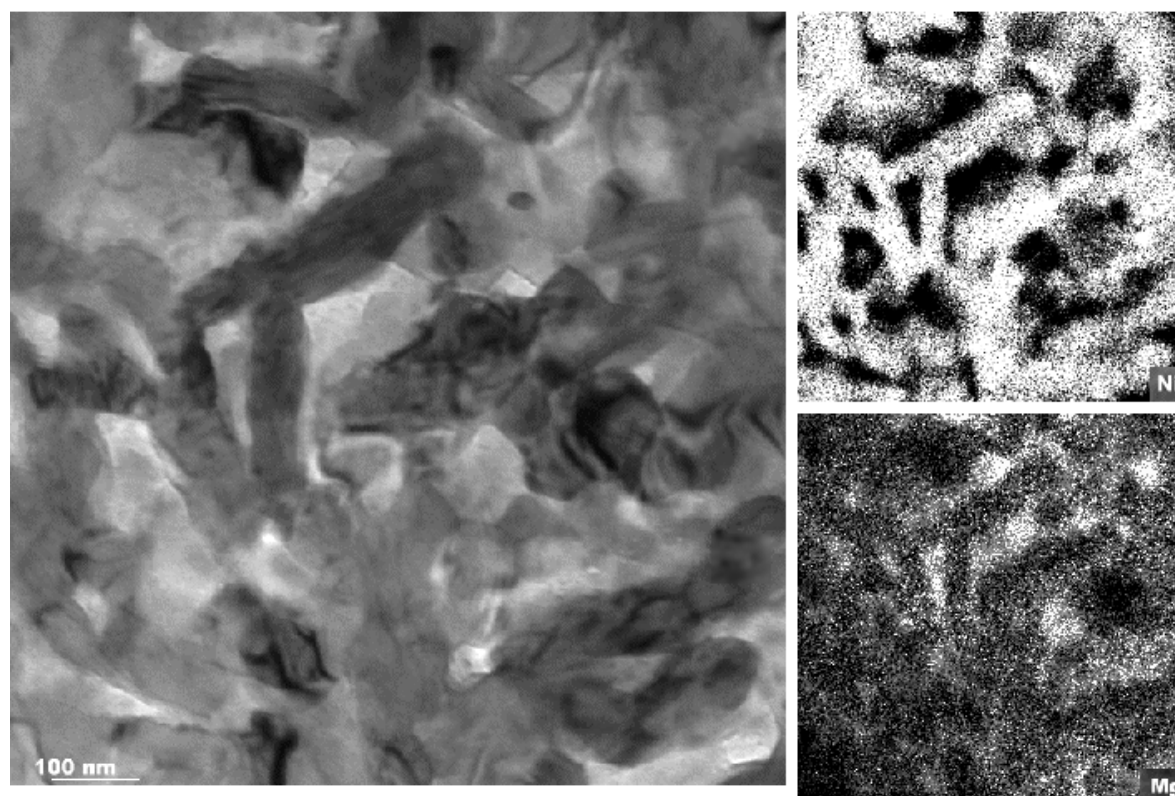


Fig.5.16b Bright field electron micrographs and EELS elemental maps (Ni and Mg) of the $Mg_{82.0}Ni_{18.0}$ alloy after annealing at 448 K.

As shown by the results discussed in section 5.4.1.1, the crystallisation of the Mg-Ni alloys takes place in two steps. The second step involves the decomposition of the intermediate phase $Mg_{-5.5}Ni$. In the case of the $Mg_{82.0}Ni_{18.0}$ alloy, very little $Mg_{-5.5}Ni$ is present after the first step (as evidenced by a very small second DSC peak and the very weak X-ray reflections, cf. section 5.4.1.1). Thus, the Mg-rich part of the microstructure as detected by EELS is considered to be Mg, and the Ni rich part of the microstructure is considered to be Mg_2Ni .

After crystallising at low temperature (Fig.5.16a), coarse Mg_2Ni particles are observed (sizes in the range of about 100-400 nm). Between these particles, a relatively fine lamellar Mg_2Ni/Mg microstructure occurs, with a lamellae thickness of about 20 nm. Upon crystallisation at high temperature (Fig.5.16b), again fairly coarse Mg_2Ni particles were formed (sizes in the range of 100-400 nm). Now, in between these particles, Mg is present.

5.5 Concluding discussion

- Mg-Cu alloys

The isothermal DSC measurements of the Mg-Cu alloys showed that the crystallisation mechanism depends on the temperature (Figs.5.3 and 5.4).

At lower temperatures, a single crystallisation process dominates. The kinetics could be

well described adopting the JMA approach with a JMA exponent of about 4 (3.8 and 4.0, cf. Fig.5.5 and Table 5.1). This result can be interpreted as indicative for interface controlled growth combined with continuous nucleation [2, 32]. This interpretation is compatible with the lamellar product microstructure as observed by TEM (Fig.5.14a) which suggests the occurrence of a eutectic, co-operative growth process of the two product phases [2]. Further, the in-situ crystallisation traced by X-Ray diffractometry confirmed that the two product phases Mg and Mg₂Cu develop simultaneously (Figs.5.10 and 5.11).

In the higher temperature regime, the crystallisation process in the Mg-Cu alloys takes place in two distinct stages. The first process involves the primary crystallisation of Mg (XRD Guinier data for alloy Mg_{85.5}Cu_{14.5}; cf. section 5.4.1.1), after which in the second process the remaining amorphous matrix crystallises in a lamellar eutectic fashion (TEM, Figs.5.14b and 5.15). Hence, the process behind the second peak in the isochronal DSC scans is similar to the one represented by the single peak observed in the isothermal DSC scan at low temperature. Thus it can be understood that fitting of the JMA model to the second peak (in the isochronal anneals) leads to about the same value for the JMA exponent ($n=3.5$; cf. Table 5.1) as obtained from the DSC data at low temperature.

As a final remark, it is noted that the process leading to the lamellar Mg/Mg₂Cu microstructure (the single peak for the isothermal anneals at low temperature; the second peak in the isochronal anneals) occurs at a relatively high temperature in the isochronal anneals. At the high temperature, a less distinct, less fine lamellar microstructure develops than at low temperatures (cf. TEM micrographs: Figs.5.14). It might then be understood that the JMA exponent derived for the isochronal anneals is somewhat lower than derived for the isothermal anneals at low temperatures, because of a (minor, but not negligible) contribution of volume diffusion to the growth rate determining process, at the high temperatures [2, 32].

- *Mg-Ni alloys*

The two Mg-Ni alloys show different crystallisation behaviour with respect to each other. This is related to the emergence of the metastable phase Mg_{-5.5}Ni in practically only one of the studied alloys. The overall composition of the studied alloys (i.e. Mg_{88.7}Ni_{11.3} and Mg_{82.0}Ni_{18.0}) is Mg-richer, and Mg-poorer, respectively, than the metastable phase Mg_{-5.5}Ni (Mg_{84.6}Ni_{15.4}). Therefore, it is conceivable that according to the (unknown; depending on the quench rate during alloy production) metastable phase diagram different (amounts of) metastable phase develop upon annealing of both amorphous alloys.

Annealing of the Mg_{82.0}Ni_{18.0} alloy leads to the development of Mg₂Ni particles in a Mg-rich (Mg/Mg₂Ni lamellar) matrix (Fig.5.16a). The JMA exponent determined equals

about 4 (4.1; cf. Fig.5.6 and Table 5.1), which suggests that the crystallisation is interface controlled in combination with continuous nucleation [2, 32].

Annealing of the $\text{Mg}_{88.7}\text{Ni}_{11.3}$ alloy leads to the intermediate development of a large amount of $\text{Mg}_{-5.5}\text{Ni}$ (cf. Fig.5.13). The subsequent kinetics of the decomposition of $\text{Mg}_{-5.5}\text{Ni}$ as investigated at higher temperatures, exhibits a JMA exponent of about 3/2 (1.5; cf. Fig.5.8 and Table 5.1) which is ascribed to rate control by volume diffusion [32].

5.6 Conclusions

1. The Johnson-Mehl-Avrami (JMA) formalism has been successfully fitted to various crystallisation processes occurring in initially amorphous Mg-Cu and Mg-Ni alloys, occurring both isothermally and isochronally. In particular, if a single step crystallisation occurs, the JMA approach can well describe the observed kinetics. However, if clearly separated processes occur successively, the JMA approach is not generally applicable.
2. To a certain extent, the crystallisation processes occurring in initially amorphous Mg-Cu and Mg-Ni alloys are similar, as expected from the similar phase diagrams for those systems. However, the occurrence of a metastable intermetallic crystalline phase for only the Mg-Ni alloys causes a striking difference in crystallisation behaviour as well.
3. The crystallisation behaviours of $\text{Mg}_{82.7}\text{Cu}_{17.3}$ and $\text{Mg}_{85.5}\text{Cu}_{14.5}$ are very similar:
 - At low temperatures, the thermodynamic stable phases Mg and Mg_2Cu precipitate cooperatively, in a nano-lamellar fashion.
 - At high temperatures, the Mg-phase precipitates primarily, after which the cooperative crystallisation of the remaining amorphous matrix takes place.
 - The JMA kinetic model can only describe the crystallisation, co-operative growth process at low temperature: the process kinetics is interface controlled combined with continuous nucleation.
4. The crystallisation behaviours of $\text{Mg}_{82.0}\text{Ni}_{18.0}$ and $\text{Mg}_{88.7}\text{Ni}_{11.3}$ are very different which is due to the emergence of the metastable $\text{Mg}_{-5.5}\text{Ni}$ phase as a transition phase in particular for the $\text{Mg}_{88.7}\text{Ni}_{11.3}$ alloy.
 - Crystallisation of amorphous $\text{Mg}_{82.0}\text{Ni}_{18.0}$ leads to Mg and Mg_2Ni (and very little $\text{Mg}_{-5.5}\text{Ni}$) in a first crystallisation step. Kinetic analysis revealed that the crystallisation is interface controlled combined with continuous nucleation. The (marginal) second crystallisation step involves the decomposition of the small amount of $\text{Mg}_{-5.5}\text{Ni}$ in Mg_2Ni and Mg.

- Crystallisation of amorphous $\text{Mg}_{88.7}\text{Ni}_{11.3}$ leads to Mg and $\text{Mg}_{\sim 5.5}\text{Ni}$. During a second annealing step at higher temperature, the $\text{Mg}_{\sim 5.5}\text{Ni}$ decomposes in Mg and Mg_2Ni .
- The metastable $\text{Mg}_{\sim 5.5}\text{Ni}$ phase most probably has a structure similar to the Mg_6Pd structure type, with a space group symmetry $F\bar{4}3m$.
- The decomposition of the $\text{Mg}_{\sim 5.5}\text{Ni}$ in the alloy $\text{Mg}_{88.7}\text{Ni}_{11.3}$ can be well described by JMA kinetics compatible with a volume diffusion rate controlled process.

5.7 Acknowledgement

One of the authors (AK) would like to express thanks to Dr A. Leineweber for useful discussions.

6 Calibration and Desmearing of a Differential Thermal Analysis measurement signal upon heating and cooling

A.T.W. Kempen, F. Sommer and E.J. Mittemeijer

Keywords: DTA, calibration, desmearing, cooling, Curie-temperature

Abstract

A new calibration and desmearing method for a Differential Thermal Analyser (DTA) upon heating and cooling is proposed. The method is based on a heat flux model of the DTA. The parameters in this model represent the DTA *independent of heating and cooling rate*, and can be determined by measuring two calibration materials. One of these should exhibit a specific heat that varies strongly, possibly non-monotonically, with temperature. Here the ferro- to paramagnetic transition (Curie point) of iron has been used. Upon application of the proposed method, the values obtained for the heat capacity of iron around the Curie temperature were found to be independent of heating or cooling rate, and in agreement with literature data.

6.1 Introduction

Calorimetric techniques, such as Differential Scanning Calorimetry (DSC) and Differential Thermal analysis (DTA) are often applied for the determination of reaction kinetics. Reaction kinetics is usually studied isothermally or isochronally upon heating (e.g. crystallisation of amorphous alloys). Phase transitions occurring upon cooling can be of great interest as well, e.g. the austenite to ferrite transformation in steels, which is of enormous technological importance.

The well-known techniques for temperature calibration on heating [61-63] are not suitable for the temperature calibration on cooling due to the lack of appropriate calibration phase transformations in a wide temperature range. Further, smearing of the measurement signal over time occurs if the detection is slow in comparison to the occurring heat effect (thermal lag). In this paper, a simple DTA calibration *and* desmearing method is proposed for heating *and* cooling experiments. To this end, measurements on calibration materials are performed. One of these materials should exhibit a specific heat that varies strongly, possibly non-monotonically, with temperature. Here the ferro- to paramagnetic transition (Curie point) of iron has been used.

In the following, the term DSC is exclusively reserved for power compensated DSC, i.e. when a difference in heating power is measured. The term DTA is adopted when heat flux DSC, or DTA is meant, i.e. when a temperature difference is measured.

6.2 Calibration and desmearing methods for DTA

6.2.1 Heat capacity calibration

A very common method of heat capacity calibration in non-isothermal DTA is to calculate the value of the apparent heat capacity of a sample ($C_{p,s}^{\text{app}}$) assuming that the measured temperature difference is proportional to the heat capacity of the specimen [64]:

$$C_{p,s}^{\text{app}} = C_{p,\text{cal}} \frac{\Delta T_{t,s}}{\Delta T_{t,\text{cal}}}, \quad (6.1)$$

with $C_{p,\text{cal}}$ as the heat capacity of the calibration material (which equals the product of the number of moles of the calibration material and the literature value for the molar heat capacity of the calibration material), $\Delta T_{t,\text{cal}}$ and $\Delta T_{t,s}$ are the measurement signals from the DTA measurements on the calibration material and on the sample, respectively. The thus determined value for the heat capacity is an *apparent* heat capacity because the influence of

smearing over time (i.e. temperature) is neglected.

6.2.2 Temperature calibration

Standard techniques are available for temperature calibration of a scanning calorimeter in heating experiments [61-63]. The most widely used method is based on the melting of pure substances: by comparison of the measured and the literature values of the melting temperatures, a temperature correction is determined. Actually, this temperature calibration depends not only on temperature but also on heating rate, thus, for each heating rate to be used, a separate temperature calibration has to be performed [65-67].

For cooling experiments at low temperatures, specific transformations are used for temperature calibration: phase transitions in liquid crystals [68, 69], solidification of specific metals that show reproducible undercooling [69], and some specific solid state phase transformation in salts or organic compounds [70].

6.2.3 Desmearing

A vast number of publications deal with the desmearing of DSC and DTA signals. Usually, an empirical temperature filter is used, where the values of the filter parameters do not have a physical meaning [71-73]. In those cases where the geometry and the operating mode of the apparatus have been incorporated, extremely complex desmearing procedures have been proposed (e.g.[74]), that furthermore can only be applied in cases of isochronal heating only. A third kind of desmearing methods is based on electrical heating pulses: through comparison of the electrical heating pulse and the detected effect, the smearing function can be established [75-77]. This last approach requires availability of an electrical heating device for the determination of the parameters of the model description of the smearing.

6.2.4 Combined calibration and desmearing

In the present work, a procedure for the simultaneous (heat capacity and temperature) calibration and desmearing of a measured DTA signal upon heating and cooling is presented, based on a heat flux model of the DTA. The procedure proposed can be used for the whole temperature range. It is proposed to employ at least two calibration materials that show different behaviours for the heat capacity as function of temperature. One of these should exhibit a very strong (preferably non-monotonically) dependence of the heat capacity on temperature. Here, pure iron is applied, that shows the ferro- to paramagnetic phase transition.

The Curie temperature corresponding to the ferro- to paramagnetic phase transition shows no temperature hysteresis [78, 79], in contrast to structural transformations, because it

involves a transformation during which no material transport takes place. The process that governs the transformation, i.e. the change in the relative orientation of electron spins is, at a temperature far above absolute zero, extremely fast, and thus the Curie temperature is not heating- or cooling rate dependent. Experimental work on the determination of the Curie temperature of Gd with different heating- and cooling rates (spanning a range of five decades in heating- and cooling rate) indeed did not reveal any heating- and cooling rate dependence of the Curie temperature [80].

Due to the sharp increase of the heat capacity to infinity (cf. section 6.4.2) at the Curie temperature, the associated DTA measurement signal is strongly smeared. Thereby, iron is very suitable as a reference material for the application of a *combined* calibration and desmearing procedure for DTA.

6.3 DTA heat flux model

A DTA apparatus measures the temperature difference between a sample (to be investigated) and a reference. Sample and reference are positioned symmetrically with respect to each other in a furnace. The configuration of the sample and its surroundings in the DTA apparatus is depicted in Fig.6.1:

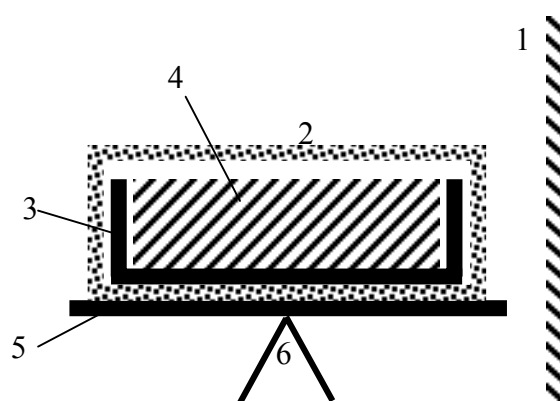


Fig.6.1 Schematic presentation of the DTA apparatus: the sample measurement cell (2-6) and furnace wall (1), where (2) is the outer sample pan with lid, (3) is the inner sample pan, (4) is the specimen, (5) is the pan holder, and (6) is the thermocouple.

The construction of the measurement cell is such that the heat capacity of the components 2,3,5 and 6 together is small in comparison to the heat capacity of the specimen, in order to enhance the sensitivity and accuracy of the measurement. The reference cell comprises an empty sample pan, but is for the rest identical to the sample measurement cell.

Heat is transported from the furnace wall (1) to each of the other, depicted components, and, depending on the heat capacities of the individual components and the thermal

resistances between them, heat transport occurs between (neighbouring) components. Most of the corresponding heat resistances are small, because most of the materials, from which the DTA measurement cells are built up, are metallic, and thus they have a small inner heat resistance. The sample and reference pan are often provided with ceramic liners, to prevent reaction between sample and the metallic sample pan, and thus they have a relatively large heat resistance.

Small thermal resistances can be neglected with respect to large thermal resistances in a serial circuit. Therefore, the measurement cell as depicted in Fig.6.1 can be modelled by using a very limited number of heat resistances and heat capacities; see Fig.6.2.

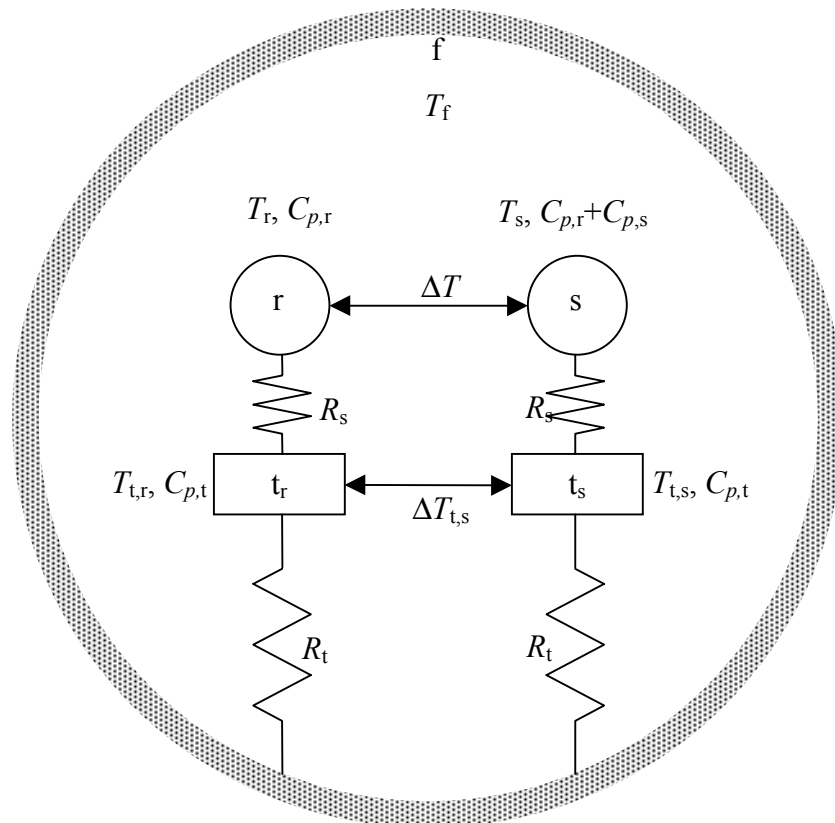


Fig.6.2 Schematic presentation of a DTA apparatus. The sample and its direct surroundings (s) are coupled to the thermocouple and its surroundings (t_s) through thermal resistance R_s . This thermocouple is coupled to the furnace (f) through heat resistance R_t . The reference side (left) is identical to the sample side (right), apart from the sample. The measurement signals are: $T_{t,r}$, $\Delta T_{t,s}$ and time t .

The DTA has a symmetric configuration, with, as only difference, the sample cell, which has the heat capacity $C_{p,r}+C_{p,s}$, vs. the reference cell, which has the heat capacity $C_{p,r}$. The heat transport to the elements t_r, r, t_s and s is given by:

$$\frac{dq_{t,r}}{dt} = \frac{(T_f - T_{t,r})}{R_t} - \frac{(T_{t,r} - T_r)}{R_s} = (C_{p,t}) \frac{dT_{t,r}}{dt}, \quad (6.2a)$$

$$\frac{dq_r}{dt} = \frac{(T_{t,r} - T_r)}{R_s} = C_{p,r} \frac{dT_r}{dt}, \quad (6.2b)$$

$$\frac{dq_{t,s}}{dt} = \frac{(T_f - T_{t,s})}{R_t} - \frac{(T_{t,s} - T_s)}{R_s} = (C_{p,t}) \frac{dT_{t,s}}{dt}, \quad (6.2c)$$

$$\frac{dq_s}{dt} = \frac{(T_{t,s} - T_s)}{R_s} = (C_{p,s} + C_{p,r}) \frac{dT_s}{dt}, \quad (6.2d)$$

where T_f is the temperature of the furnace wall, T_s and T_r denote the temperatures of the sample and reference cells, and $T_{t,s}$ and $T_{t,r}$ are the temperatures of the thermocouples for sample cell and reference cell, respectively, $C_{p,s}$ is the heat capacity of the sample, $C_{p,r}$ is the heat capacity of the direct surroundings of the sample (i.e. the heat capacity of the reference cell), $C_{p,t}$ is the heat capacity of the thermocouple and its direct surroundings, and t is the time. The measurement signals are $\Delta T_{t,s} = T_{t,s} - T_{t,r}$, $T_{t,r}$.

The thermocouple for the absolute temperature determination (i.e. t_r) is not calibrated, and therefore a, temperature and heating rate independent, temperature shift of the thermocouple must be recognised as well: ΔT_{tc} .

Thus, the DTA apparatus can be represented by five (heating and cooling rate independent) parameters, further called the DTA parameters: (i) the heat resistance between the furnace wall and the thermocouples, R_t , (ii) the heat capacity of the thermocouple and its direct surroundings, $C_{p,t}$, (iii) the heat capacity of the direct surroundings of the specimen, $C_{p,r}$, (iv) the heat resistance R_s between sample and thermocouple (identical to the heat resistance between reference and thermocouple), and (v) the thermocouple temperature shift ΔT_{tc} .

The value of R_t is determined as a function of temperature according to the procedure described in section 6.4.1. The values of $C_{p,r}$, $C_{p,t}$ and R_s are in principle not independent of temperature, but for a not too large temperature range, they can be taken as constants. Otherwise, the possible temperature dependence of $C_{p,r}$, $C_{p,t}$ and R_s can be accounted for by performing the in this project described calibration and desmearing procedure at different temperatures (involving application of different calibration materials).

The above model of a DTA apparatus has been validated here, and the DTA parameters have been determined accordingly, by measuring the heat capacity of pure iron around the Curie temperature. The validation criterions comprise the comparison of the determined $C_{p,Fe}$ values with literature values, and the comparison with each other of the $C_{p,Fe}$ curves determined for the different heating and cooling rates.

6.4 Data evaluation

6.4.1 Determination of DTA parameters

The values of the five DTA parameters can be determined by DTA measurements on substances of known C_p . In this project, the values of the parameters were determined by measuring subsequently sapphire and iron, using, in both cases, four heating rates and four cooling rates. Sapphire has a molar heat capacity that smoothly changes with temperature, and iron exhibits a (heating rate independent) strongly varying molar heat capacity around the Curie temperature.

The DTA parameters $C_{p,t}$, $C_{p,r}$, and R_s can be determined by fitting as described below; the DTA parameters R_t and ΔT_{tc} follow by straightforward calculus, the parameter R_t is calculated in each iteration step and the value of ΔT_{tc} is determined after completion of the fitting process. The successive steps of the fitting procedure are as follows:

(i) Initial values of the fitting parameters $C_{p,t}$, $C_{p,r}$, and R_s are prescribed. Then, using the values of $T_{t,r}$, given as function of time by the temperature program, the sapphire measurement signal ($\Delta T_{t,sap} = T_{t,sap} - T_{t,r}$) and the value for the heat capacity of sapphire ($C_{p,sap}$, c.f. section 6.5), T_r , T_f , R_t and T_{sap} are calculated for each measurement curve (each measurement curve corresponds to one heating or cooling rate) as a function of temperature, $T_{t,r}$, from the four Eqs.(6.2a)-(6.2d). The value of R_t must be independent of heating and cooling rate, and thus the average of R_t over all measurement curves is used in the further evaluation.

(ii) The thus determined values of R_t , and T_f are used for the calculation of $C_{p,Fe}$ and the temperature $T_{s,Fe}$ from the DTA iron measurement curve (i.e. $T_{t,r}$ and $\Delta T_{t,Fe}$ as function of time t), using the two Eqs.(6.2c) and (6.2d). The determined results for $C_{p,Fe}$ as function of $T_{s,Fe}$ should be equal *for all heating and cooling rates*. Hence, the fit criterion is that the difference in $C_{p,Fe}$ as function of $T_{s,Fe}$, as determined at different heating and cooling rates, is small. The difference considered is defined as the product of (1) the average standard deviation for $C_{p,Fe}(T_{s,Fe})$ obtained by, firstly, determining the standard deviation in $C_{p,Fe}$ at each $T_{s,Fe}$ from the curves at different heating and cooling rates, and, secondly, averaging this standard deviation over the whole temperature range, and (2) the standard deviation of the values of the Curie temperatures (defined as the temperature at which the maximum in $C_{p,Fe}(T_{s,Fe})$ occurs) as determined at different heating and cooling rates.

(iii) The fit parameters $C_{p,t}$, $C_{p,r}$, and R_s are changed according to a simplex procedure [24], and the calculation sequence (i-ii-iii) is repeated until the fit criterion described under

(ii) is satisfied.

(iv) ΔT_{tc} is obtained as the difference between the value determined for the Curie temperature (of iron) and the literature value for the Curie temperature (of iron).

Thus, by performing DTA measurements on two calibration materials, employing different heating and cooling rates, the DTA parameters R_t , $C_{p,r}$, $C_{p,t}$, R_s and ΔT_{tc} can be determined. The two calibration materials should be selected carefully. Here, sapphire is chosen as it shows a heat capacity changing smoothly with temperature, which enables determination of R_s (see above, step (i)). Further, iron is chosen for its sharply peaked behaviour of the heat capacity. Thereby the iron measurement is in particular sensitive to smearing.

Note that the first derivatives of the measurement signals ($T_{t,r}$ and $T_{t,s}=\Delta T_{t,s}+T_{t,r}$) are used in the described procedure (Eqs.(6.2a) and (6.2c)). This enhances the sensitivity for scatter in the measurements, which is suppressed by using a moving weighted-average filter [24] for the differentials of the measurement signals.

6.4.2 The C_p of iron

Many references present measured values for the molar heat capacity of iron around the Curie-temperature [81-89]. Most of these values were obtained by adiabatic calorimetry or by pulse heating techniques, which can be considered as the most accurate methods for measurement of C_p [90]. Here, an analytical description of $C_{p,Fe}$ is given that satisfies the data given in Refs.[81-89]. In Ref.[91], an analytical function for $C_{p,Fe}$ has been given previously. However, this formula does not describe the behaviour of $C_{p,Fe}$ of iron around the Curie-temperature adequately (cf. Fig.6.5 and its discussion).

For the analytical description of $C_{p,Fe}$, the non-magnetic contribution to $C_{p,Fe}$ as given in Ref.[91] was used: the first four terms in Eq.(6.3). The contribution of the magnetic ordering to $C_{p,Fe}$ is taken as given by [92, 93], but here, a supplementary exponential factor is introduced, in order to better describe the experimental data given in Refs.[81-89]. Thus, the analytical description of $C_{p,Fe}$ reads:

$$C_{p,Fe} = a + bT + cT^2 + dT^{-2} + f_i \exp(e_i T^*) (T^*)^{g_i}, \quad (6.3)$$

where, $T^* = |(T - T_c)/T_c|$, with T_c as the Curie temperature, $a=23.5143(\text{Jmol}^{-1}\text{K}^{-1})$, $b=8.79504 \cdot 10^{-3}(\text{Jmol}^{-1}\text{K}^{-2})$, $c=3.535614 \cdot 10^{-7}(\text{Jmol}^{-1}\text{K}^{-3})$, $d=154717(\text{Jmol}^{-1}\text{K})$, and e to g are parameters to be determined in this study. The label i equals 1 if $T < T_c$, and equals 2 if $T \geq T_c$.

This equation was fitted to the literature $C_{p,Fe}$ data, as given in Refs.[81-89], leading to values for the fitting parameters e_i, f_i and g_i .

6.4.3 The C_p of sapphire

The molar heat capacity of sapphire has been adopted as given in Ref.[94]:

$$C_{p,sap} = \alpha_0 + \alpha_1(T - T_0) + \alpha_2(T - T_0)^2 + \alpha_3(T - T_0)^3 + \alpha_4(T - T_0)^4 + \alpha_5(T - T_0)^5, \quad (6.4)$$

where $T_0=273.15\text{K}$, and the parameters $\alpha_0=73.10(\text{Jmol}^{-1}\text{K}^{-1})$, $\alpha_1=0.2477(\text{Jmol}^{-1}\text{K}^{-2})$, $\alpha_2=-6.321 \cdot 10^{-4}(\text{Jmol}^{-1}\text{K}^{-3})$, $\alpha_3=9.760 \cdot 10^{-7}(\text{Jmol}^{-1}\text{K}^{-4})$, $\alpha_4=-7.967 \cdot 10^{-10}(\text{Jmol}^{-1}\text{K}^{-5})$ and $\alpha_5=2.624 \cdot 10^{-13}(\text{Jmol}^{-1}\text{K}^{-6})$.

6.5 Experimental

Using a Netzsch DSC 404C (which, according to the definition in section 6.1, is a DTA), equipped with the DSC C_p sensor, a high temperature furnace (up to 1773 K), and Pt10%Rh/Pt thermocouples, three subsequent runs were performed: with an empty sample pan, with a sapphire sample (of purity 99.99 wt%) and with an iron sample (of purity 99.98 wt%). The sapphire and the iron samples were disc shaped with a diameter of about 5 mm, and a thickness of about 1.5 mm. These three measurements were performed using the same reference and sample pans, and the same temperature-time program, employing a number of heating and cooling rates.

In order to correct for small differences between the sample cell and the reference cell, the measurement signal $\Delta T_{t,s}$ for the empty run (which equals zero in the ideal case) is subtracted from the corresponding measurement curves recorded from sapphire and iron. The resulting values are considered to represent the true measurement signal, $\Delta T_{t,s}$.

The data analysis is performed as described in section 6.4.1, using as input data the Curie temperature of iron, $T_c=1043\text{ K}$ (Ref.[91]), and the (molar) heat capacity of sapphire (cf. section 6.4.3).

6.6 Results and Discussion

From the measurements as described in section 6.5, the *apparent* molar heat capacity of iron was calculated, using Eq.(6.1), taking the measurement with sapphire as the calibration measurement.

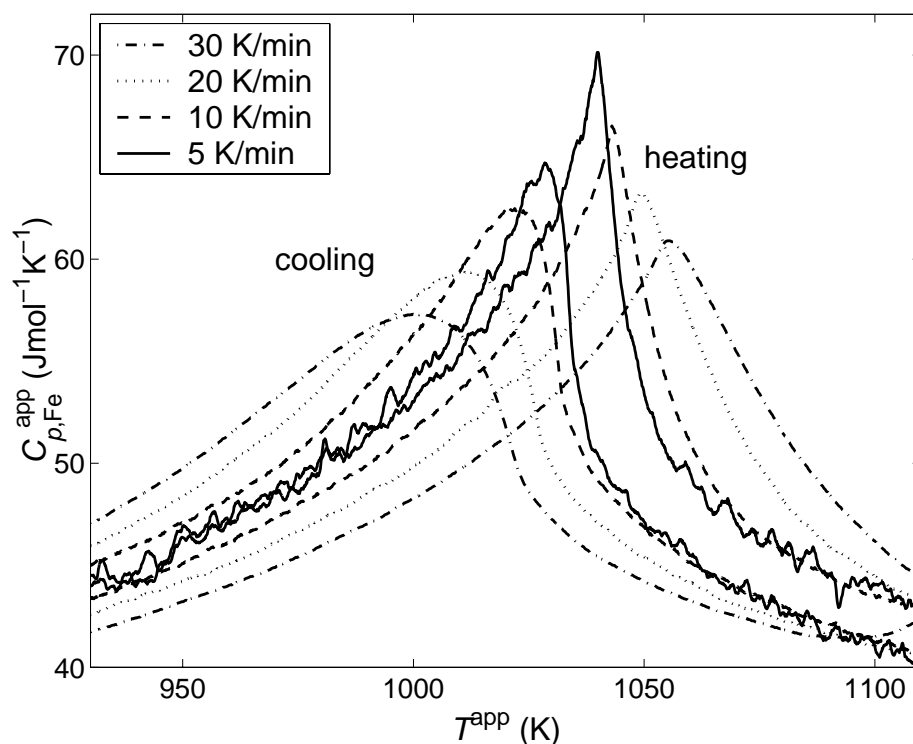


Fig.6.3 Apparent molar heat capacity (cf. Eq.(6.1)) of pure iron as determined from the DTA measurements at various heating and cooling rates, using sapphire as calibration material.

Crudely speaking, the presented $C_{p,Fe}^{app}$ (Fig.6.3) is proportional to the measured signal ($\Delta T_{t,Fe}$) divided by the heating or cooling rate (cf. Eq.(6.2a)). It is clear from Fig.6.3 that the apparent molar heat capacity as determined using Eq.(6.1), strongly depends on the heating or cooling rate. The real heat capacity is independent of heating rate (cf. section 6.2.2). The erroneous heating rate dependence of $C_{p,Fe}^{app}$ exhibited in Fig.6.3 is caused by the smearing and the temperature shift inherent to the DTA apparatus. Next, the correction method for the smearing and temperature shift, as proposed in section 6.4.1, was applied to the measured data.

6.6.1 The C_p of iron

Application of the correction method for smearing and temperature shift to the measured data, $\Delta T_{t,sap}$ and $\Delta T_{t,Fe}$ as function of $T_{t,r}$, as described in section 6.4.1, led to results for the real molar heat capacity shown in Fig.6.4, and the values for the DTA parameters given in Table 6.2.

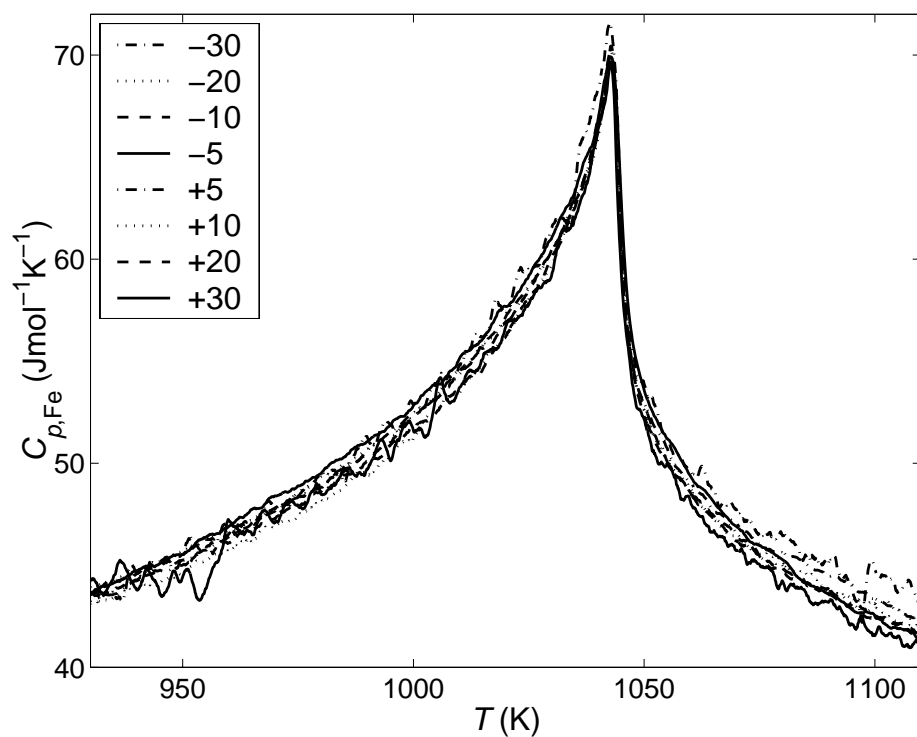


Fig.6.4 True molar heat capacity of pure iron, $C_{p,Fe}$, as obtained after application of the correction procedure for smearing and temperature shift, for various applied heating and cooling rates.

Indeed, the result for $C_{p,Fe}$ as derived from the measurements is independent of heating and cooling rate. The ordinate values of the curves presented in Fig.6.4, as averaged over the heating and cooling rate, are plotted in Fig.6.5, together with literature data of the molar heat capacity of iron [81-89], and the analytical descriptions given by Ref.[91] and Eq.(6.3).

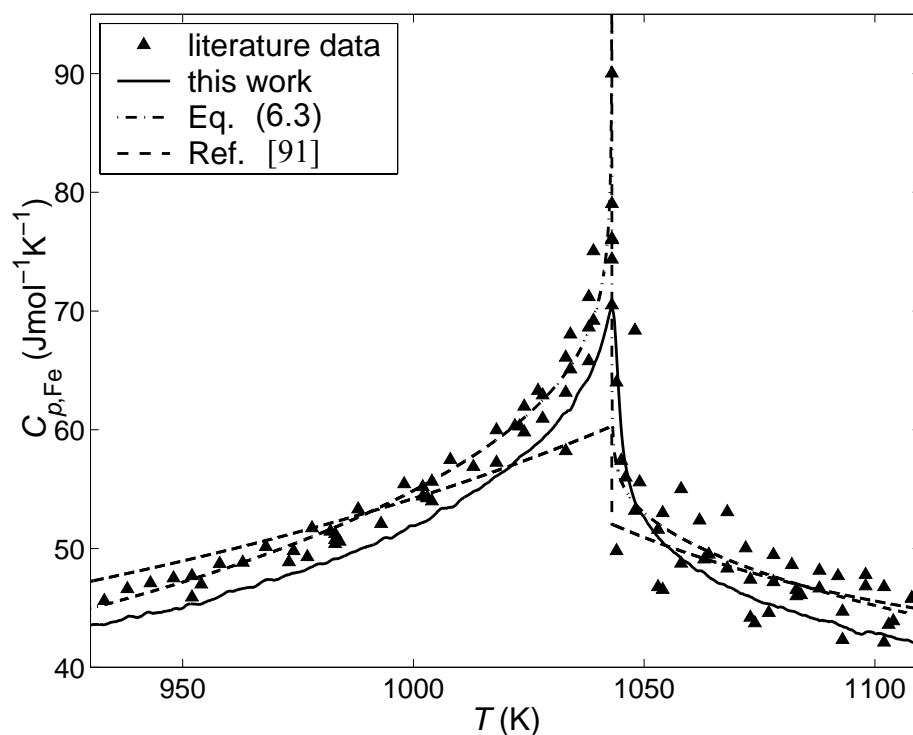


Fig.6.5 Molar heat capacity of iron as determined in this work measured (—, the average over all heating and cooling rates calculated from the plots shown in Fig.6.4); from literature [81-89] where every single data set was shifted such that $T_c=1043$ K(▲); as described by Eq.(6.3) (- -); and as given in Ref.[91] (- -).

The shape of the $C_{p,Fe}$ curve derived from the measurements agrees very well with the shape of the curve representing the literature data. The measured value for $C_{p,Fe}$ is about $2 \text{ Jmol}^{-1}\text{K}^{-1}$ lower than the literature value. This difference is within the experimental accuracy of a C_p determination by DTA in the temperature range considered; in particular it should be noted that low heating and cooling rates (i.e. 5 and 10 K/min) were included in the analysis, which normally affects the experimental accuracy. That the small discrepancy is of systematic character, might be due to the *non-metallic* nature of the calibration substance sapphire as compared to the *metallic* nature of the material (iron) investigated.

The line representing the literature data as depicted in Fig.6.5 has been obtained by fitting Eq.(6.3) to the literature data [81-89], where every single data set was shifted such that $T_c=1043$ K [91]. The values of the corresponding fit parameters are given in Table 6.1.

Table 6.1 Values of the fit parameters, e_i , f_i and g_i , obtained from fitting Eq.(6.3) to literature data [81-89] where every single data set was shifted such that $T_c=1043$ K [91]. The parameters e_1 , f_1 and g_1 hold for $T < T_c$, and e_2 , f_2 and g_2 hold for $T \geq T_c$.

e_1	-5.0323	e_2	-7.0110
f_1	15.9226	f_2	12.0728
g_1	-0.1577	g_2	-0.1123

As follows from Fig.6.5, the literature data for $C_{p,Fe}$ can be described very well by Eq.(6.3). The value of parameter g used for this description, should be between 0 and -0.16 [92]. The present result satisfies this requirement, but it should be noted that the in this work applied exponential factor incorporated in the present description (cf. Eq.(6.3)) can influence the value of g .

6.6.2 The DTA parameters

The DTA parameters as determined from the sapphire and iron measurements by the procedure described in section 6.4.1 have been given in Table 6.2

Table 6.2 DTA parameters as determined by fitting ($C_{p,t}$, $C_{p,r}$, and R_s), and by direct calculus calculation (ΔT_{tc} and R_t) (cf. section 6.4.1). Further, the heat capacities of the sapphire and the iron sample are given as determined from the number of moles ($n_{Fe}=4.2 \cdot 10^{-3}$ mol; $n_{sap}=8.2 \cdot 10^{-4}$ mol) and the molar heat capacity (i.e. Eqs.(6.3) and (6.4)). The values of R_t , $C_{p,sap}$ and $C_{p,Fe}$ are given for different temperatures.

$C_{p,t}$ (JK ⁻¹)	0.0676			
$C_{p,r}$ (JK ⁻¹)	0.0326			
R_s (sKJ ⁻¹)	61.2359			
ΔT_{tc} (K)	7.1			
T (K)	1000	1025	1050	1075
R_t (sKJ ⁻¹)	64.8526	62.2368	59.6920	57.2239
$C_{p,sap}$ (JK ⁻¹)	0.1028	0.1032	0.1035	0.1038
$C_{p,Fe}$ (JK ⁻¹)	0.2255	0.2527	0.2225	0.1993

The presented heat capacities, $C_{p,t}$ and $C_{p,r}$, are smaller than the heat capacities of the samples, $C_{p,sap}$ and $C_{p,Fe}$ which is plausible, cf. first paragraph of section 6.3. The value obtained for the thermocouple shift ΔT_{tc} is also plausible. The temperature dependent heat resistance R_t

becomes smaller with increasing temperature, which is understandable recognising that with increasing temperature, the contribution of radiation to the heat transport process increases.

6.6.3 Influence of smearing

To demonstrate the influence of the smearing, the apparent molar heat capacity of iron (as defined according to Eq.(6.1)) has been calculated from the true molar heat capacity of iron (adopting Eq.(6.3); cf. discussion in section 6.6.1), applying the smearing according to Eqs.(6.2). The calculation is performed by numerical integration (using a 4th order Runge-Kutta method [24]) of the Eqs.(6.2) and adopting the DTA parameters as given in Table 6.2. Results for the heating and cooling rates of 30 K/min are shown in Fig.6.6. The experimental $C_{p,Fe}^{app}$ (derived from the measurements using Eq.(6.1), see also Fig.6.3) is shown in Fig.6.6 as well.

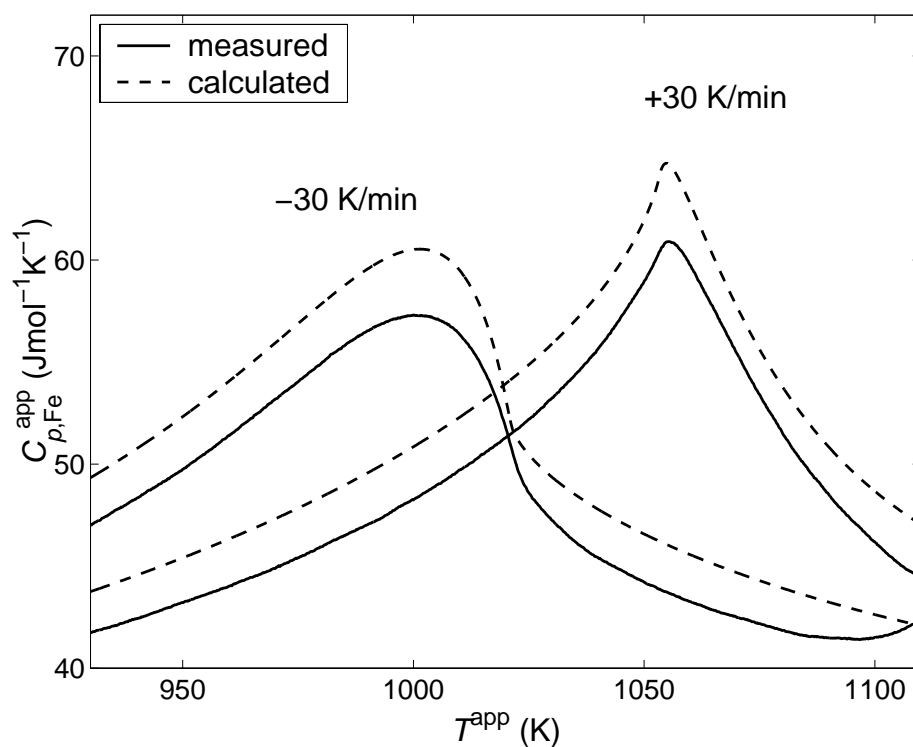


Fig.6.6 The *apparent* molar heat capacity as calculated directly from the measurement using Eq.(6.1) (—), and as calculated from the *true* molar heat capacity $C_{p,Fe}$ (section 6.6.1) applying the smearing according to Eqs.(6.2) using the DTA parameters given in Table 6.2(- -) for heating and cooling at 30 K/min.

The shape of the as calculated smeared $C_{p,Fe}^{app}$ peaks agrees very well with the shape of the experimentally determined $C_{p,Fe}^{app}$ peaks. The systematic, small difference between ordinate values has already been discussed in section 6.6.1. Hence, the DTA model presented here, can

be used both for the desmearing of experimentally smeared peaks (cf. Fig.6.4), as well as the mathematical smearing of real C_p peaks (simulation of DTA experiment).

The observed difference between $C_{p,Fe}^{app}$ peak shapes for heating and cooling is not caused by the instrumental smearing because the smearing is symmetrical with respect to the heating or cooling rate applied (cf. Eqs.(6.2)). The asymmetry in the $C_{p,Fe}$ peak in combination with smearing on cooling leads to a strong asymmetry in the apparent heat capacity peak obtained on cooling, whereas smearing upon heating counteracts the asymmetry in $C_{p,Fe}$, leading to a less distinct asymmetry in the apparent heat capacity peak obtained on heating, see Fig.6.6.

6.7 Conclusions

DTA equipment can be modelled by a heat flux model, incorporating only five parameters that are *independent* of heating or cooling rate. On this basis measured DTA curves can be, simultaneously, both calibrated with respect to heat capacity and temperature and corrected for the heating and cooling rate dependent smearing of the signal. Thus, a general procedure is available, allowing for calibration and desmearing upon heating *and* cooling.

The model parameters can be determined by measuring the heat capacity of two calibration materials: one that features a heat capacity only smoothly varying with temperature, and one that features a heat capacity strongly varying with temperature. This heat capacity variation should be independent of heating and cooling rate. Here, sapphire and iron were used as calibration materials, where the ferro- to paramagnetic transformation in iron caused the, heating- and cooling rate independent, strong variation of the heat capacity. The molar heat capacity of sapphire and the Curie temperature of iron were used as input data. Fitting of the model yielded the model parameters and the true molar heat capacity of iron as a function of temperature. The course of the true molar heat capacity curve of iron around the magnetic transition agrees well with literature data, thereby validating the proposed calibration and desmearing procedure.

7 The kinetics of the austenite–ferrite phase transformation of Fe-Mn; Differential Thermal Analysis during cooling

A.T.W. Kempen, F. Sommer and E.J. Mittemeijer

Keywords: austenite-ferrite phase transformation, kinetics, iron-alloy, DTA

Abstract

Differential thermal analysis (DTA) has been employed to study the austenite-ferrite phase transformation of Fe-1.89at% Mn upon cooling. The transformation has been shown to occur in two stages. The first stage is not thermally activated; the second stage is thermally activated. A phase transformation model, incorporating a new impingement correction, has been used for the extraction, from the DTA experiments, of data for the velocity of the austenite-ferrite interface. It followed that the interface velocity does not only depend on temperature, but also on transformed fraction. This has been interpreted as the consequence of the (non-neglectable) dissipation of energy by the volume misfit of the austenite and ferrite phases during the transformation. This misfit accommodation Gibbs energy has been assessed quantitatively; it has been shown to be of the same order of magnitude as the chemical Gibbs energy.

7.1 Introduction

Properties of steels are mainly determined by their composition and microstructure. The microstructure of the steel can be tuned by controlling the austenite (γ) to ferrite (α) phase transformation. In practice, the transformation is typically executed by combined deformation and annealing treatments, e.g. as in a hot rolling process.

To acquire basic understanding of the γ - α transformation, Fe-Mn [73, 95, 96] and Fe-Mn-C [97-100] alloys are often considered as model systems. In this work, very accurate data for the γ - α transformation kinetics in Fe-1.89 at% Mn, as a function of temperature, have been obtained by means of Differential Thermal Analysis (DTA), in combination with a recently developed procedure for the desmearing and calibration of DTA measurements, *also upon cooling* [101]. This new procedure for DTA evaluation [101] allows very accurate determination of transformation kinetics, because the true shape (i.e. unaffected by instrumental aberrations) of the DTA transformation peak is retrieved.

In contrast with earlier work [73, 95] on the $\gamma \rightarrow \alpha$ phase transformation kinetics, in this work the role of the interface energy and of the misfit accommodation energy between the austenite and ferrite phases has not been ignored. Here, a method has been proposed for the experimental determination of the sum of the elastic and plastic misfit accommodation energies and the interface energy between austenite and ferrite.

7.2 Phase transformation kinetics

The phase transformation $\gamma \rightarrow \alpha$ upon cooling of Fe-Mn alloys with low Mn content is not completed, in practical time-spans [102], according to the equilibrium phase diagram (Fig.7.1). This phase diagram was determined employing very long annealing times (years) in order to assure that equilibrium was reached [102].

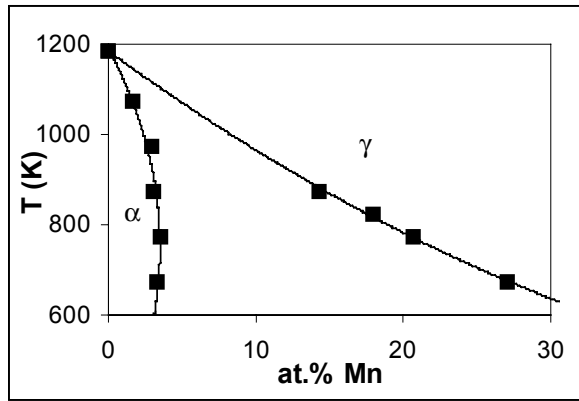


Fig.7.1 Partial phase diagram for the Fe-Mn system. The lines have been drawn through data points from Ref.[102].

The diffusion of manganese needed to establish the manganese enrichment of the remaining austenite matrix during growth of the manganese depleted ferrite particles is very slow, such that the transformation practically does not take place. At large undercooling, e.g. upon entering the α one-phase region during cooling, the γ - α transformation can take place under release of energy even if no manganese redistribution occurs. The γ - α transformation of the Fe-1.89 at% Mn alloy investigated thus takes place as a partitionless transformation, i.e. without any occurring composition difference between the parent γ -phase and the product α -phase.

A general procedure for the simulation of phase transformation kinetics on the basis of nucleation and growth mechanisms has been given in Ref.[32]. The first step of this procedure involves the calculation of the volume of all growing particles, assuming that the grains never stop growing and that new grains hypothetically nucleate also in the transformed material (i.e. at this stage, 'hard impingement' is ignored) [5-8]. This volume is called the extended volume (V_e), and the extended volume divided by the total specimen volume (V_0) is called the extended transformed fraction x_e . In a next step, the extended transformed fraction is corrected for 'hard impingement' of the growing particles, and the corresponding real transformed fraction, f , is obtained. Thus, the kinetic model is characterised by the specific models adopted for (1) the nucleation process, (2) the growth process, and (3) the hard impingement.

7.2.1 Nucleation model

It has been argued above that decomposition of austenite into α and γ does not occur significantly in the α - γ two-phase region during cooling. Yet, *nucleation* of ferrite can take place upon traversing the two-phase region [73, 103]. Thus, during subsequent decomposition

occurring at temperatures and compositions within the α one-phase region, the nucleation can be supposed to have been completed at the very start of growth, i.e. ‘site saturation’ is adopted. Hence, the transformation model adopts N particles that are able to start growing at time $t=0$ s.

7.2.2 Growth model

The extended volume of a growing particle is given by

$$V_e = g \left(\int v(T, f) dt \right)^3, \quad (7.1)$$

with g as a geometrical factor, v as the velocity of the interface between the product and parent phase which depends on the temperature, T , and the transformed fraction, f . The interface velocity is considered to be proportional with the product of the interface mobility (M) and the driving force ($\Delta G_{\alpha\gamma}$) (see e.g. Ref.[104]):

$$\begin{aligned} v(T, f) &= M(T) \left[-\Delta G_{\alpha\gamma}(T, f) \right] \\ \Delta G_{\alpha\gamma} &= \Delta G_{\alpha\gamma}^{chem}(T) + \left[\Delta G_{\alpha\gamma}^{def}(f) + \Delta G_{\alpha\gamma}^{int}(f) \right], \end{aligned} \quad (7.2)$$

with $\Delta G_{\alpha\gamma}^{chem}$ as the molar chemical Gibbs energy difference between the ferrite and the austenite, $\Delta G_{\alpha\gamma}^{int}$ as the molar free energy of the interface between the ferrite and the austenite, and $\Delta G_{\alpha\gamma}^{def}$ as the summation of elastic and plastic molar accommodation energies resulting from misfit strains between the parent and product phases [105]. The driving force consists of a negative term $\Delta G_{\alpha\gamma}^{chem}$, which favours the transformation, and two positive terms which counteract the transformation. The interface mobility is supposed to show an Arrhenius like temperature dependence [2]. Usually, the driving force, $\Delta G_{\alpha\gamma}$, is supposed to consist only of the chemical Gibbs energy difference, and the dissipation of Gibbs energy by plastic and elastic accommodation and the formation of interface are neglected [73, 95, 106]; for an exception, see Ref.[107].

The chemical driving force depends on temperature, and not on the degree of transformation, because the transformation is partitionless. The deformation energy in general will depend on the degree of transformation and not primarily on temperature, since the amount of strain build-up in the specimen increases during transformation, thereby making continued transformation more difficult (partially compensating strain relaxation may occur; see discussion in section 7.4.7). The interface energy, per mole of transformed material, will also depend on the fraction transformed, and not primarily on temperature, because the ratio

of the γ/α interfacial area and the volume of ferrite produced changes during the transformation.

7.2.3 Impingement model

An impingement model provides the relationship between the extended transformed fraction and the real transformed fraction.

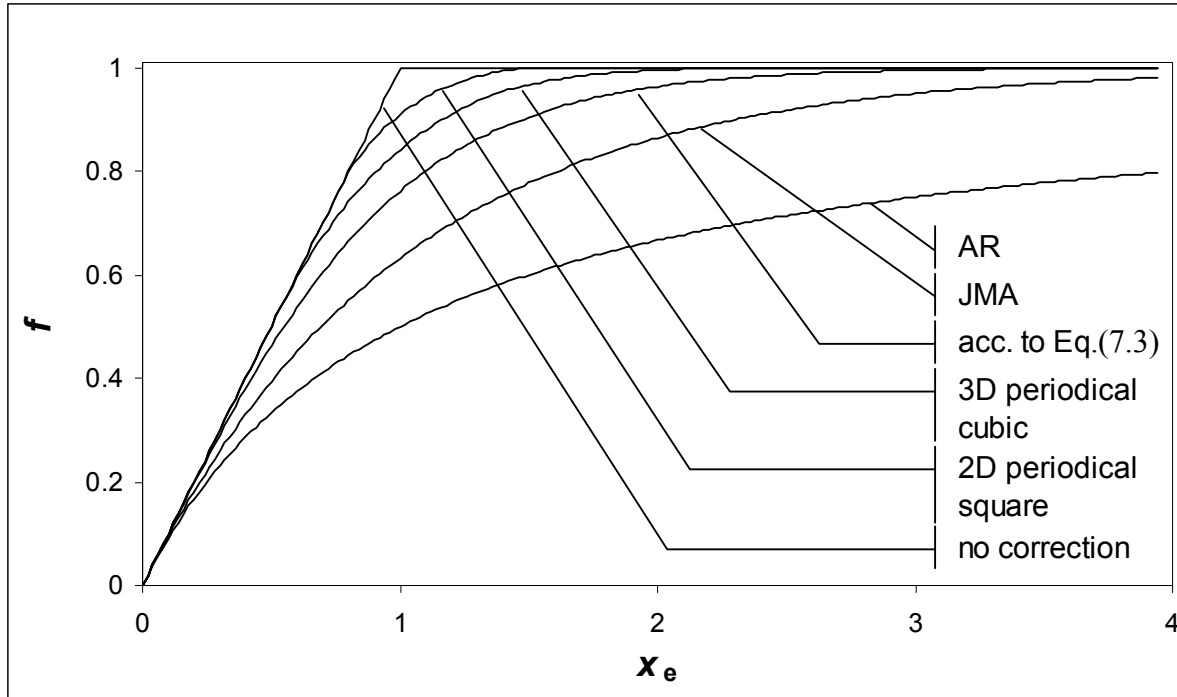


Fig.7.2 The transformed fraction, f , as function of the extended transformed fraction, x_e , for different models: Johnson-Mehl-Avrami (JMA), Austin-Rickett (AR), according to Eq.(7.3), no correction, and for periodical dispersed growing particles, on a primitive cubic (3 dimensions) or square (2 dimensions) lattice.

As a limiting case, the fraction transformed is shown in Fig.7.2 in the absence of correcting for any impingement, i.e. $f=x_e$ for $x_e \leq 1$, and $f=1$ for $x_e > 1$. For any impingement model, it is impossible that $f > x_e$, or $f > 1$. The impingement correction as incorporated in the Johnson-Mehl-Avrami (JMA) model, $f = 1 - \exp(-x_e)$, with $x_e = V_e/V_0$, is based on the assumption that the growing particles are dispersed randomly throughout the total volume [2, 32]. A more regular dispersion of the growing particles, as compared to the ideal, randomly dispersed case, would lead to a smaller influence of the impingement correction i.e., the difference between x_e and f is smaller. As examples, the impingement for the cases of two- and three dimensional periodically dispersed (on a square and cubic grid, respectively) growing particles has been calculated here, analytically (two-dimensional) and by a numerical [24] Monte-Carlo method (three-dimensional). Results are shown in Fig.7.2. The effect of 'soft impingement' i.e. the

impingement of the diffusion fields in volume diffusion controlled growth processes [108], is shown as well in Fig.7.2 by the Austin-Rickett (AR) [109] impingement correction function, $f = 1 - \frac{1}{1 + x_e}$. Note that in the present work, soft impingement does not play a role, because

the transformation occurs partitionless.

If the initial material is polycrystalline, the corners of the grains of the parent phase can act as preferred nucleation sites. This implies that the dispersion of the growing particles cannot be considered as truly ‘random’, and thus the JMA impingement correction does not hold exactly. The dispersion of the growing particles will also be not exactly periodic, corresponding to a not exactly homogeneous initial crystallite size and shape, and thus the impingement correction for ideally periodically dispersed growing particles is also incorrect. Therefore, in the present project, a simple impingement correction has been adopted which allows correction for hard impingement that is an intermediate of the cases of ideally periodically, and of ideally randomly dispersed growing particles; cf. Fig.7.2. The present impingement correction function is given by:

$$f = \tanh(x_e). \quad (7.3)^2$$

7.2.4 Resulting kinetic model

Upon combining the models for nucleation, growth and impingement as presented in sections 7.2.1-7.2.3, the transformed fraction is given by:

$$f = \tanh\left(\frac{NV_e}{V_0}\right), \quad (7.4)$$

where V_e is given by Eqs.(7.1) and (7.2).

7.3 Experimental

7.3.1 Alloy production

High purity iron and manganese (see Ref.[96] for composition data) were melted in an induction furnace and cast in a copper mould. The ingot of diameter 10 mm was hammered down to a rod of 2.3 mm diameter. In order to achieve a homogeneous manganese distribution

² Eq.(7.3) implies $\frac{df}{dx_e} = 1 - f^2$; for the JMA impingement correction $\frac{df}{dx_e} = 1 - f$ holds, and for the Austin-Rickett impingement correction it holds: $\frac{df}{dx_e} = (1 - f)^2$.

in the sample, the rod was sealed in a quartz container, filled with argon gas at $3 \cdot 10^4$ Pa and annealed at 1473 K for 100 hours. The composition of the rod was determined by Inductive Coupled Plasma-Optical Emission Spectrometry, resulting in a value for the manganese content of 1.89 at.% Mn.

7.3.2 Differential Thermal Analysis

Differential Thermal Analysis (DTA) measurements were performed on the material as prepared, in order to determine the fraction ferrite and austenite quantitatively during the course of the phase transformation austenite to ferrite upon cooling. Cylinders of 2.3 mm diameter and 1.5 mm height were cut of the alloy rod. The flat sides of the cylinders were ground (mesh 1200) to obtain a perfectly plain surface. Three of these small cylinders were enclosed in a platinum sample pan, which was covered on the inside with an Al_2O_3 liner. The cylinders were carefully placed, with the flat surface on the bottom, and as close as possible to the centre of the sample pan.

A Netzsch DSC 404 C (which is a heat-flux differential scanning calorimeter (DSC), based on measuring a temperature difference and thus can also be called DTA; cf.[101]), equipped with the DSC C_p sensor, was employed for the calorimetric measurement of the heat effect corresponding to the $\gamma \rightarrow \alpha$ phase transformation. Fresh specimens were used for each measurement, to ensure that for each measurement the specimens had the same microstructure and thermal/mechanical history. The specimens were heated from room temperature to 1223 K with 20 K/min and kept at this temperature for 30 min. Then they were cooled employing cooling rates of 5, 10, 20 and 30 K/min. The $\gamma \rightarrow \alpha$ transformation occurring upon cooling was analysed from the corresponding DTA measurement signal (see section 7.3.5). Additional measurements were performed by heating fresh specimens from room temperature to 1223 K using heating rates of 5, 10, 20 and 30 K/min, in order to determine the temperature dependence of the heat capacity around the Curie temperature.

The DTA was calibrated, and the measurement signal was corrected for smearing, according to the method and calibration measurements as described in Ref.[101].

7.3.3 Grain size determination

The ferrite grain sizes of fully transformed specimens were determined by light microscopical analysis of the DTA specimens. From each DTA specimen two metallographic samples were prepared, for acquisition of microstructural information on two different planes: parallel and perpendicular to the cylinder axis. The grain boundaries were revealed by etching, using a 5% Nital solution. The line intercept method [110, 111] was employed in three independent

directions, in order to determine the grain size and shape. The line intercept method results in a grain size value, which is an underestimate of the true grain size. The true average grain diameter of ferrite, $2\bar{r}_\alpha$, is thus assessed by multiplying the obtained intercept length by a factor 1.5 [111].

7.3.4 Heat capacity around the Curie temperature

An equation for the temperature dependence of the heat capacity around the Curie temperature of pure iron was presented in Ref.[101]. This equation was used here as well for the Fe-Mn alloy, with different numerical values for the parameters involved, as follows:

$$C_{p,\alpha} = a + bT + cT^2 + dT^{-2} + f_i \exp(e_i T^*) (T^*)^{g_i}, \quad (7.5)$$

where $T^* = |(T - T_c)/T_c|$, T_c denotes the Curie temperature, a to d are parameters representing the non-magnetic contribution to the heat capacity [91], and e_i to g_i are parameters that give the magnetic contribution to the heat capacity. The label i equals 1 if $T < T_c$, and equals 2 if $T \geq T_c$. The values of the parameters a - g could not be determined directly from the measurements on cooling due to the overlap of the magnetic transition peak and the $\gamma \rightarrow \alpha$ transformation peak. Upon heating, these peaks did not overlap due to the shift of the $\gamma \rightarrow \alpha$ transformation peak to higher temperatures. Therefore, heating experiments (cf. section 7.3.2) were used for determination of the parameters a - g (see also Ref.[101]).

7.3.5 Calculation of the fraction transformed

The measured signal recorded upon cooling can be used to calculate the experimental heat capacity as a function of temperature for all cooling rates by applying the desmearing and calibration method described in Ref.[101]. The thus calculated, experimental heat capacity, $C_{p,\text{exp}}$, is not a true heat capacity because of the occurrence of heat release by the phase transformation. Thus the calculated experimental heat capacity during the $\gamma \rightarrow \alpha$ transformation can be written as:

$$C_{p,\text{exp}} = f_\alpha C_{p,\alpha} + f_\gamma C_{p,\gamma} + \frac{df_\alpha}{dT} \Delta H_{\alpha\gamma}, \quad (7.6)$$

where f is the fraction of the phase indicated by the subscript ($f_\alpha + f_\gamma = 1$), C_p is the true heat capacity of the phase indicated by the subscript, T is the temperature and $\Delta H_{\alpha\gamma} = H_\alpha - H_\gamma$ is the enthalpy difference of both phases. The first two terms at the right hand side of Eq.(7.6) state that the heat capacity of a mixture of phases can be given as the weighted average (according to the amounts of the individual phases) of the heat capacities of the phases. The last term at

the right hand side of Eq.(7.6) gives the enthalpy-release (rate) contribution of the γ - α phase transformation to the apparent heat capacity of the entire specimen. Note that in Eq.(7.6), apart from $C_{p,\text{exp}}$, f_α and f_γ , $C_{p,\alpha}$, $C_{p,\gamma}$ and $\Delta H_{\alpha\gamma}$ depend on temperature. The values of $C_{p,\alpha}$ and $C_{p,\gamma}$ can be extracted from the measurement signal outside the temperature range where the transformation takes place. Within the range where the transformation takes place, the temperature dependence of $C_{p,\gamma}$ can be determined by extrapolation, and the temperature dependence of $C_{p,\alpha}$ can be determined as described in section 7.3.4. The temperature dependence of the enthalpy difference $\Delta H_{\alpha\gamma}$ is caused by the difference between the temperature dependencies of the true heat capacities of the separate phases [73]:

$$\Delta H_{\alpha\gamma}(T) = H_0 + \int_{T_1}^T (C_{p,\alpha}(T) - C_{p,\gamma}(T)) dT, \quad (7.7)$$

where H_0 is the (initial) value of $\Delta H_{\alpha\gamma}$ at T_1 [73], which is to be determined according to the following procedure. Comparing the measured curve for $C_{p,\text{exp}}$ with the (extrapolated) curve for $C_{p,\gamma}$ a temperature T_1 can be estimated where the γ - α transformation starts, and where $f_\gamma=1$. Similarly, T_2 is determined as the temperature where the transformation is just completed and where $f_\alpha=1$. By prescribing H_0 , $\Delta H_{\alpha\gamma}$ as a function of temperature from $T=T_1$ to $T=T_2$ can be calculated, using Eq.(7.7). These values of $\Delta H_{\alpha\gamma}$ are used as input in Eq.(7.6), where now f_α is the only unknown (as $f_\gamma=1-f_\alpha$) and thus f_α can be determined from the $C_{p,\text{exp}}$ data. The value of H_0 is adjusted (by trial and error) such that the ferrite fraction equals one at $T=T_2$.

7.3.6 Determination of interface velocity

The calculation procedure as given in section 7.3.5 yields the ferrite fraction, f_α (=transformed fraction, $f=f_\alpha$) and the transformation rate, df_α/dt (as dT/dt is known and constant). As follows from Eq.(7.4) by differentiation, the transformation rate can be given by:

$$\frac{df_\alpha}{dt} = \frac{df_\alpha}{dx_e} \frac{dx_e}{dV_e} \frac{dV_e}{dt} = \frac{3Ng}{V_0} v(1-f_\alpha^2) \left(\int v(T, f_\alpha) dt \right)^2 \quad (7.8)$$

Now, expressing $\left(\int v(T, f) dt \right)$ in terms of f using Eqs.(7.1) and (7.4), and introducing the average ferrite grain radius after completed transformation $\bar{r}_\alpha = \left(\frac{Ng}{V_0} \right)^{-\frac{1}{3}}$ (the volume of one

particle is defined as gr_{α}^{-3}), leads to:

$$\frac{df_{\alpha}}{dt} = 3 (1 - f_{\alpha}^2) \operatorname{arctanh}^{\frac{2}{3}}(f_{\alpha}) \bar{r}_{\alpha}^{-1} v(T, f). \quad (7.9)$$

Thus, using the values of transformation rate df_{α}/dt and the transformed fraction f_{α} , the interface velocity can be determined, as a function of temperature, or time, and transformed fraction for the different cooling rates applied.

7.4 Results and Discussion

7.4.1 Grain size of Fe-Mn ferrite

The ferrite grain sizes of the DTA specimens that were cooled at different cooling rates were determined as described in section 7.3.3. The grains showed an overall equi-axed morphology.

Table 7.1 Grain radius \bar{r}_{α} as a function of cooling rate, for the Fe-1.89at% Mn specimens.

cooling rate (K/min)	grain radius \bar{r}_{α} (μm)
5	54
10	42
20	57
30	43

The grain size does not depend significantly on the cooling rate, as the differences in the grain size values in Table 7.1 are smaller than the experimental scatter [111].

7.4.2 Heat capacity of Fe-Mn ferrite

As described in sections 7.3.2 and 7.3.4, the heat capacity of the ferritic Fe-Mn alloys, $C_{p,\alpha}$, was determined from $C_{p,\text{exp}}$ values measured upon heating, employing heating rates of 5-30 K/min, and after desmearing (see section 7.3.2 and Ref.[101]); $C_{p,\text{exp}}=C_{p,\alpha}$ for fully ferritic specimens; cf. Eq.(7.6).

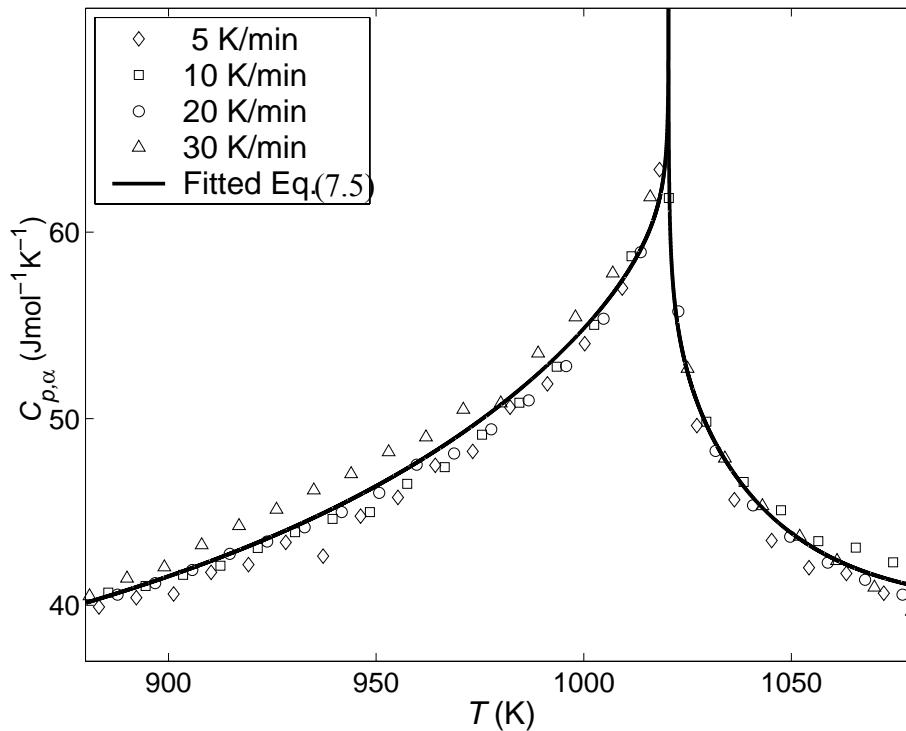


Fig.7.3 Heat capacity of Fe 1.89 at% Mn ferrite, $C_{p,\text{exp}}=C_{p,\alpha}$, as determined from the DTA measurement at different heating rates (symbols), and according to Eq.(7.5) fitted to the measured data (line).

The values of the parameters for the analytical description of $C_{p,\alpha}$ around the Curie temperature (Eq.(7.5)) were obtained from fitting Eq.(7.5) to the experimental $C_{p,\text{exp}}$. The results are given in Table 7.2 for the temperature range 700-1080 K.

Table 7.2 Values of the fit parameters, T_C and $a-g$ for the analytical description of $C_{p,\alpha}$ (Eq.(7.5)), corresponding to the fit showed in Fig.7.3

T_C	(K)		1020.4
a	(Jmol ⁻¹ K ⁻¹)		20.8418
b	(Jmol ⁻¹ K ⁻²)		0.0312
c	(Jmol ⁻¹ K ⁻³)		-1.0935·10 ⁻⁵
d	(Jmol ⁻¹ K)		-2.9487·10 ⁶
e_1	-10.8741	e_2	-32.2353
f_1 (Jmol ⁻¹ K ⁻¹)	16.1504	f_2 (Jmol ⁻¹ K ⁻¹)	8.1340
g_1	-0.0637	g_2	-0.1269

Eq.(7.5) describes the measured $C_{p,\alpha}$ curve very well. The value obtained for the Curie temperature for Fe-1.89at% Mn agrees very well with the data ($T_c=1019.2\pm 1.5$ K) given in

Ref.[96]. Further, the parameter g , should be between 0 and -0.16 [92], which holds here.

7.4.3 Heat capacity of Fe-Mn austenite

The heat capacity of austenite was measured in all experiments, i.e. upon heating and upon cooling. Due to the shift to lower temperature of the transformation peak of the $\gamma \rightarrow \alpha$ transformation upon cooling, as compared to heating, $C_{p,\gamma}$ was measured over a much larger temperature range upon cooling. A constant value for the heat capacity was observed, $C_p^\gamma = 32.9 \text{ (Jmol}^{-1}\text{K}^{-1}\text{)}$ in the temperature range 1100-1223K. This value is very slightly (about 2%) lower than the value reported in Ref.[96].

7.4.4 Enthalpy difference of γ and α

Eq.(7.7) was integrated numerically employing a 4th order Runge Kutta method [24], between $T_1=1120 \text{ K}$ and $T_2=830 \text{ K}$ on prescribing H_0 . Using the thus obtained values for $\Delta H_{\alpha\gamma}$, Eq.(7.6) was integrated from T_1 to T_2 applying a 1st order Heun method [24] with step size 0.1 K. H_0 was adjusted until $f_\alpha=1$ at $T=T_2$.

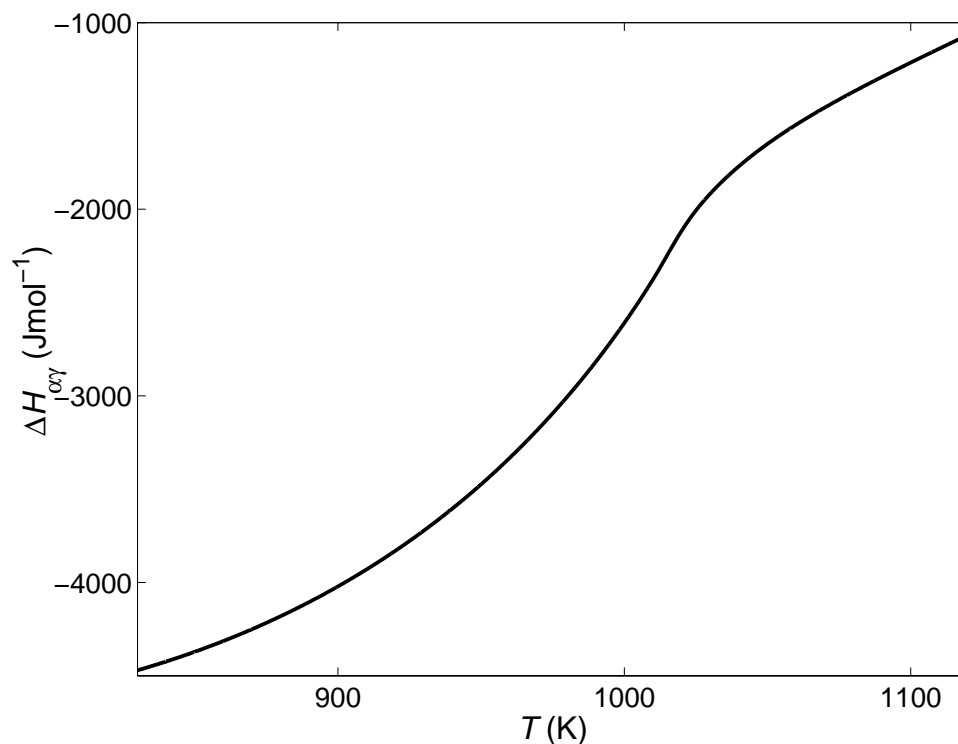


Fig.7.4 Enthalpy difference $\Delta H_{\alpha\gamma}$ as a function of temperature, as determined from the DTA measurements on cooling.

The accuracy of the determination of $\Delta H_{\alpha\gamma}$ as presented here can be estimated from the difference between the results obtained from the runs at different cooling rates; the

corresponding accuracy is about 100 kJ/mol. The values obtained for $\Delta H_{\alpha\gamma}$ (see Fig.7.4) are in good agreement with previous literature data [73, 96].

7.4.5 Transformed fraction

Applying the calculation procedure described in section 7.3.5, the ferrite fraction formed upon the $\gamma \rightarrow \alpha$ phase transition, and the transformation rate can be determined. The corresponding results obtained from the runs performed at different cooling rates are shown in Figs.7.5 and 7.6.

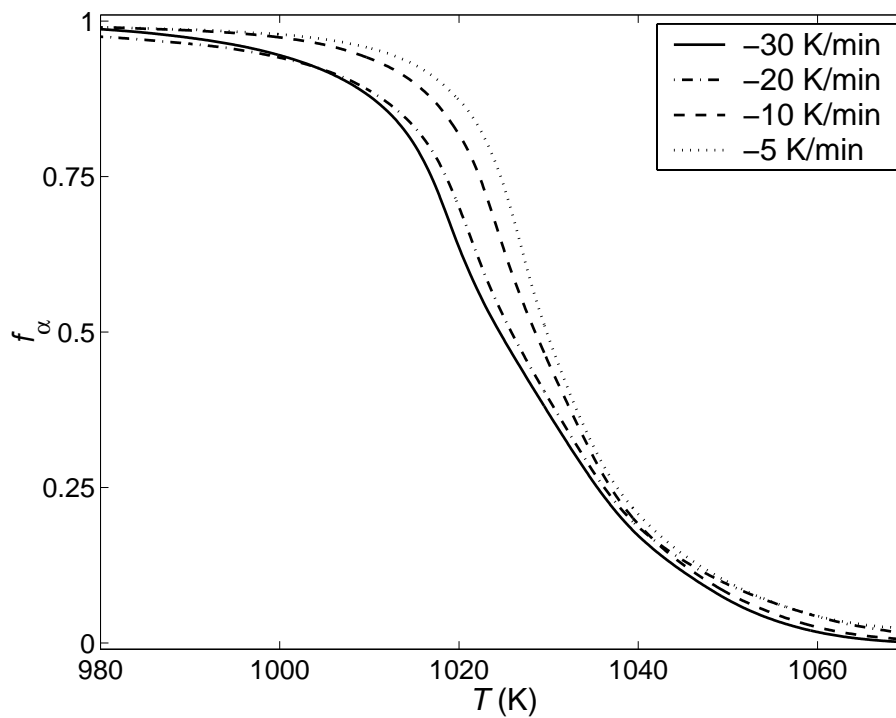


Fig.7.5 Ferrite fraction, f_α , as function of temperature, as determined from the DTA measurements performed at the cooling rates indicated.

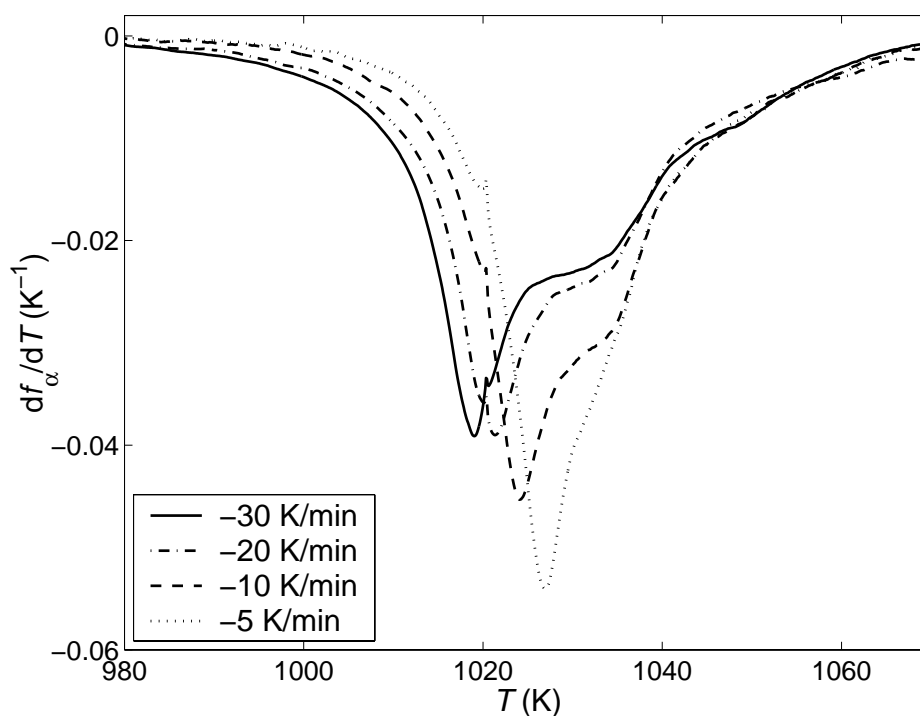


Fig.7.6 Transformation rate divided by cooling rate, df_{α}/dT , as function of temperature, as determined from the DTA measurements performed at the cooling rates indicated.

In contrast with the measurements of the transformed fraction as presented in Refs.[73, 96], the $\gamma \rightarrow \alpha$ transformation here appears to consist of two steps. The appearance of two steps is the more pronounced the higher the cooling rate. Note that the measurements in Refs.[73, 96] have been presented only as transformed fraction against temperature plots, which hinders the recognition of a possible two stage process (cf. Figs.7.5 and 7.6).

It follows from Figs.7.5 and 7.6 that the first transformation stage (i.e. above 1040 K) is much less, if at all, dependent on cooling rate than the second stage. This suggests that the first stage is not thermally activated. This can be interpreted as follows. In the first stage of transformation (at the relatively high temperatures of the cooling runs), the gain in chemical energy (per mole transformed material) is relatively small (cf. Fig. 7.4). At high temperatures, the interface mobility is large. Apparently, at the high temperatures considered, the interface velocity is that large, that the transformation upon cooling proceeds at each temperature until that fraction transformed where the gain in chemical energy is fully dissipated by the deformation and interface energies introduced by transformation. Hence, at relatively high temperatures, f_{α} depends on temperature but not on cooling rate. At lower temperatures the interface mobility is relatively small and can become rate limiting for the transformation, leading to cooling rate dependence for the second stage of transformation.

7.4.6 Interface velocity

From the experimentally determined parameters, (i) transformed fraction, f_α , (ii) transformation rate, df_α/dt and (iii) the average ferrite grain radius after completed transformation, \bar{r}_α , the interface velocity can be calculated using Eq.(7.9). The results are shown in Fig.7.7.

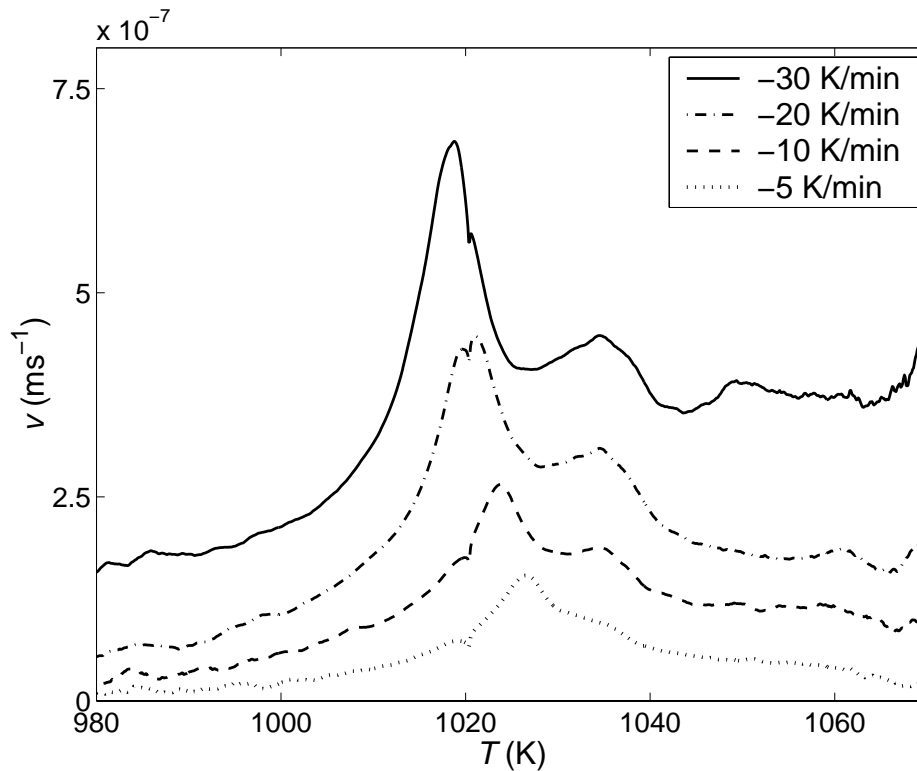


Fig.7.7 Interface velocity of growing ferrite particles in an austenite matrix, as determined for the various cooling rates indicated.

The values for the interface velocity determined close to the start and the end of the transformation are not reliable due to mathematical instability of Eq.(7.9): at $f_\alpha=0$ or at $f_\alpha=1$, the left and right hand side of Eq.(7.9) are both zero, independent of the value for the interface velocity.

If the assumption would hold that $\Delta G_{\alpha\gamma}^{def}(f)$ and $\Delta G_{\alpha\gamma}^{int}(f)$ can be neglected, then $v(T) = M(T)[- \Delta G_{\alpha\gamma}^{chem}(T)]$ (cf. Eq.(7.2)). Then, upon cooling, a maximum in the interface velocity might be expected because $- \Delta G_{\alpha\gamma}^{chem}(T)$ increases and $M(T)$ decreases for decreasing temperature. In this case (i.e. upon neglecting $\Delta G_{\alpha\gamma}^{def}(f)$ and $\Delta G_{\alpha\gamma}^{int}(f)$), the interface velocity only depends on temperature, and not on cooling rate. Apparently, this is not the

case: see Fig.7.7. Hence, $\Delta G_{\alpha\gamma}^{def}(f)$ and $\Delta G_{\alpha\gamma}^{int}(f)$ cannot be neglected. The deformation and interface energies depend on fraction transformed, and thereby the interface velocity becomes dependent on, also, the fraction transformed (cf. section 7.2.2). This explains the cooling rate dependence observed for the interface velocity (Fig.7.7).

The appearance of two maximums in the interface velocity (Fig.7.7) is related to the appearance of a two stage transformation as already shown in Fig.7.6: the first maximum occurs at about the same temperature, independent of cooling rate; the second maximum (at lower temperature) depends on cooling rate (see discussion in section 7.4.5).

7.4.7 Driving force for precipitation

The driving force for precipitation consists of three parts: $\Delta G_{\alpha\gamma}^{chem}(T)$ which depends on temperature (and not on the transformed fraction as the transformation is partitionless), and $\Delta G_{\alpha\gamma}^{def}(f)$ and $\Delta G_{\alpha\gamma}^{int}(f)$ which depend on the transformed fraction (and not directly on temperature) (cf. Eq.(7.2)). Values for the chemical driving force for the formation of one mole ferrite from one mole austenite were obtained here using the thermodynamic evaluation according to Ref.[112]; results are shown in Table 7.3.

Table 7.3 Value of the chemical driving force, $\Delta G_{\alpha\gamma}^{chem}$, for the partitionless γ - α transformation, as function of temperature for Fe-1.89at% Mn, adopting the thermodynamic evaluation according to [112]. The temperature where metastable Fe-1.89at% Mn austenite and metastable Fe-1.89at% Mn ferrite are in equilibrium is 1076 K.

T (K)	$\Delta G_{\alpha\gamma}^{chem}$ (Jmol ⁻¹)
800	-1070
850	-785
900	-530
950	-316
1000	-151
1050	-41
1100	32
1150	81
1200	114

Data for the interface mobility $M(T)$ (cf. Eq.(7.2)) are experimentally hardly available.

On the basis of knowledge of the driving force, the interface mobility can be calculated from interface velocities. Mobility data for the recrystallisation of pure iron (ferrite) have been determined [104]. In that case, no phase change take place, the chemical driving force is zero, and the accommodation energy for deformation can be neglected; the only driving force is the interface energy. Thus, the interface mobility data given in Table 7.4 were obtained.

Table 7.4: Values for the pre-exponential factor M_0 and the activation energy Q for the mobility

$$M(T) = M_0 \exp\left(-\frac{Q}{RT}\right); \text{ data from Ref. [104] for pure iron (ferrite); data from Ref. [73] for Fe-Mn;}$$

data from Ref. [95] were claimed to hold for several binary substitutional iron alloys.

Ref.	M_0 (m mol J ⁻¹ s ⁻¹)	Q (kJ/mol)
[104]	$4.9 \cdot 10^3$	147
[73]	$5.8 \cdot 10^{-2}$	140
[95]	2.4	140

In recent work on the $\gamma \rightarrow \alpha$ phase transformation [73, 95], only the chemical contribution to the driving force was considered. The energy dissipation due to interface generation and the misfit accommodation reduces the net (absolute) driving force for the transformation. Neglecting this energy dissipation as in Refs. [73] and [95] leads to an underestimation of the mobility (as assessed from interface velocity data), which, as compared to the data in Ref. [104], could explain the low values for M_0 reported in Refs. [73, 95].

Now, using the interface velocity data shown in Fig. 7.7, the data for the chemical driving force (data were numerically described as a 4th order polynomial) in Table 7.3, the mobility data of Ref. [104] given in Table 7.4, $\Delta G_{\alpha\gamma}^{def} + \Delta G_{\alpha\gamma}^{int}$ can be calculated (cf. Eq. (7.2)). The results are shown in Fig. 7.8. Results for $f_\alpha < 0.1$ and $f_\alpha > 0.9$ have not been given as the corresponding interface velocity data are unreliable (cf. section 7.4.6). In an advanced stage of transformation, the results become rather sensitive to the type of impingement correction chosen. This adds to the uncertainty in the results for $\Delta G_{\alpha\gamma}^{def} + \Delta G_{\alpha\gamma}^{int}$ in particular for large values of f_α .

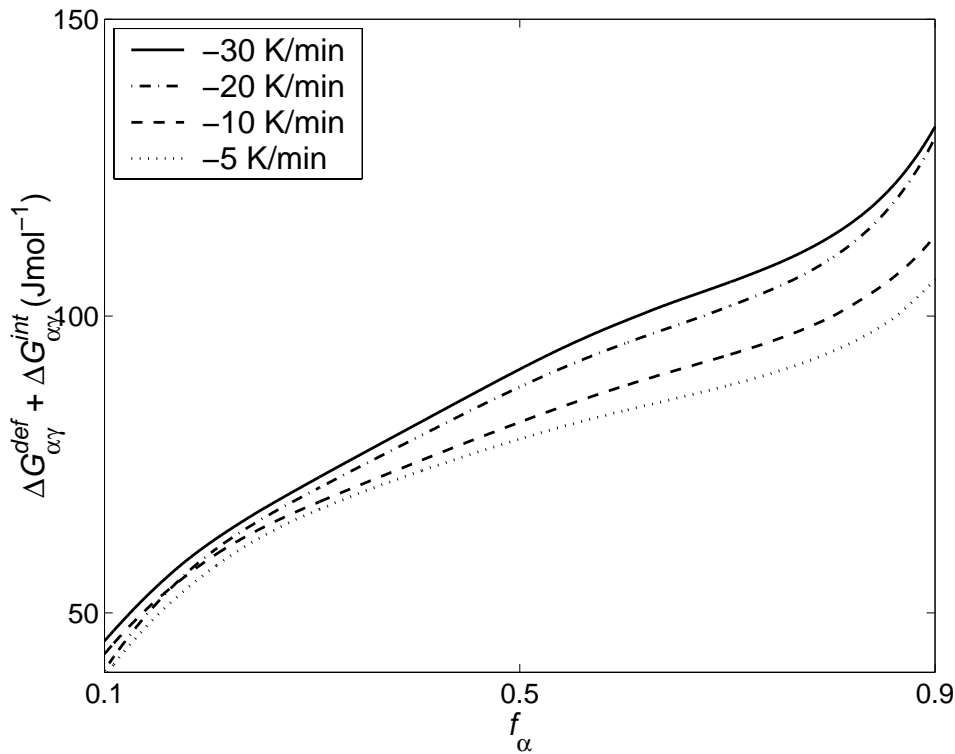


Fig.7.8 The summation of elastic and plastic misfit accommodation energies resulting from misfit strains and the interface energy (parent: γ , product: α) as function of the fraction transformed as determined for the various cooling rates indicated.

Clearly, $\Delta G_{\alpha\gamma}^{def} + \Delta G_{\alpha\gamma}^{int}$ is of the same order of magnitude as $-\Delta G_{\alpha\gamma}^{chem}$ (cf. Table 7.3 and Fig.7.8) and evidently cannot be neglected in the expression for the driving force.

Adopting an interface energy of 0.8 Jm^{-2} [113] for the α - γ interface and taking the number of growing particles as $1.4 \cdot 10^7 \text{ mol}^{-1}$ (as calculated from \bar{r}_α and the molar volume of ferrite), the energy dissipated by the formation of the interface is estimated to be 0.2 Jmol^{-1} at a stage of transformation of $f_\alpha=0.5$. Thus, $\Delta G_{\alpha\gamma}^{int}$ is neglectable in comparison to $\Delta G_{\alpha\gamma}^{def}$.

It follows that $\Delta G_{\alpha\gamma}^{def}$ increases with increasing fraction transformed, as may be expected (cf. section 7.2.2). Further it is observed that $\Delta G_{\alpha\gamma}^{def}$ becomes somewhat smaller for a smaller cooling rate (see Fig.7.8). This could be ascribed to the occurrence of a time and temperature dependent relaxation process (as creep) that causes a more noticeable decrease of the accommodation energies if the specimen is cooled at lower rate.

7.5 Conclusions

1. To take into account the non-random nature of the distribution of growing particles in a solid-solid phase transformation, a new impingement correction is proposed: $f = \tanh(x_e)$, where f is the fraction transformed and x_e is the (so-called) extended fraction transformed.
2. In contrast to earlier observations, the γ - α transformation, occurring upon cooling, proceeds in two stages. The first stage is not thermally activated.
3. On the basis of the kinetic model adopted (site saturation; interface controlled growth (partitionless transformation); impingement according to the above point 1., the interface velocity for the γ - α transformation, could be determined from DTA measurements (Eq.(7.9)).
4. From the interface velocity data, values for the driving force (Gibbs energy difference between ferrite and austenite) could be calculated. In contrast with earlier assumptions in the literature, it followed that the misfit accommodation energy *cannot* be neglected, as compared to the chemical Gibbs energy difference: they are of the same order of magnitude.
5. The heat capacity of the Fe-Mn ferrite can be well described by an analytical equation: Eq.(7.5).

8 Zusammenfassung

8.1 Einführung

Die Materialeigenschaften können durch Beherrschung der Produktionsprozesse beeinflusst werden, wobei Festkörperphasenumwandlungen eine wichtige Rolle spielen. In der Stahlindustrie werden zum Beispiel, nachdem der Stahl gegossen ist, die erhaltenen Blöcke meistens warm gewalzt, wobei die Temperatur, der Verformungsgrad und die Abkühlgeschwindigkeit die wichtigsten Parameter sind, um die erwünschten Eigenschaften des Materials zu erhalten. Für eine gezielte Einstellung von Materialeigenschaften ist es notwendig, die zugrundeliegenden Prozesse zu kennen. Viele Modelle zur Beschreibung von Phasenumwandlungen sind in der Literatur bekannt. Eines der bekanntesten Modelle ist das von Johnson, Mehl [5] und Avrami [6-8] (JMA). In dieser Arbeit wird ein allgemeines Modell vorgestellt, das die drei Teilprozesse einer Phasenumwandlung beschreibt: Keimbildung, Wachstum und das Zusammenstoßen von wachsenden Teilchen. Für jeden der einzelnen Teilprozesse stehen mehrere Modelle (teilweise innerhalb dieser Arbeit entwickelt) zur Verfügung. Die Auswahl geeigneter Modelle erfolgt auf Grund der vorliegenden Mikrostruktur. Für spezifische Fälle entspricht dieses allgemeine Modell dem bekannten JMA Modell.

8.2 Kinetisches Modell

Das allgemeine kinetische Modell beruht auf der Beschreibung der drei Teilprozesse: Keimbildung, Wachstum und Zusammenstoßen der wachsenden Teilchen. Die Beschreibung der Keimbildung ergibt die Anzahl von Teilchen pro Zeiteinheit in einem Einheitsvolumen von nicht umgewandeltem Material die wachstumsfähig werden (s. Abschnitt 8.2.1). Die Wachstumsmodelle beschreiben die Volumenänderung von einem Teilchen in einer unendlich großen Matrix als Funktion der Zeit. Kombiniert ergeben die Keimbildungs- und Wachstumsmodelle das ‚extended volume‘, wobei (virtuelle) Keimbildung auch in der umgewandelten Phase stattfindet und wobei das Zusammenstoßen der wachsende Teilchen nicht berücksichtigt wird. Die Berechnung des real umgewandelten Volumens aus dem ‚extended volume‘ erfolgt nach unterschiedlichen Modellen, die den Teilprozeß des Zusammenstoßens der wachsenden Teilchen berücksichtigen.

8.2.1 Keimbildung

Bei einer Umwandlung formt sich eine stabilere Phase aus einer instabileren Phase. Die

Bildung jedes Teilchen der stabileren Phase ist jedoch nicht mit einem Energiegewinn verbunden. Wenn ein Teilchen der neuen Phase sehr klein ist, hat es ein ungünstiges Oberflächen/Volumen Verhältnis, wodurch das Teilchen instabil ist. Die Bildung eines wachstumsfähigen Teilchens wird als Keimbildung bezeichnet. In dieser Arbeit wird der Prozeß der Keimbildung nur makroskopisch betrachtet, d.h. nicht einzelne Keime sind von Interesse, sondern die Anzahl von Keimen pro Volumeneinheit als Funktion der Zeit. Vier Keimbildungsmodelle werden in diese Arbeit betrachtet (s. Fig.8.1).

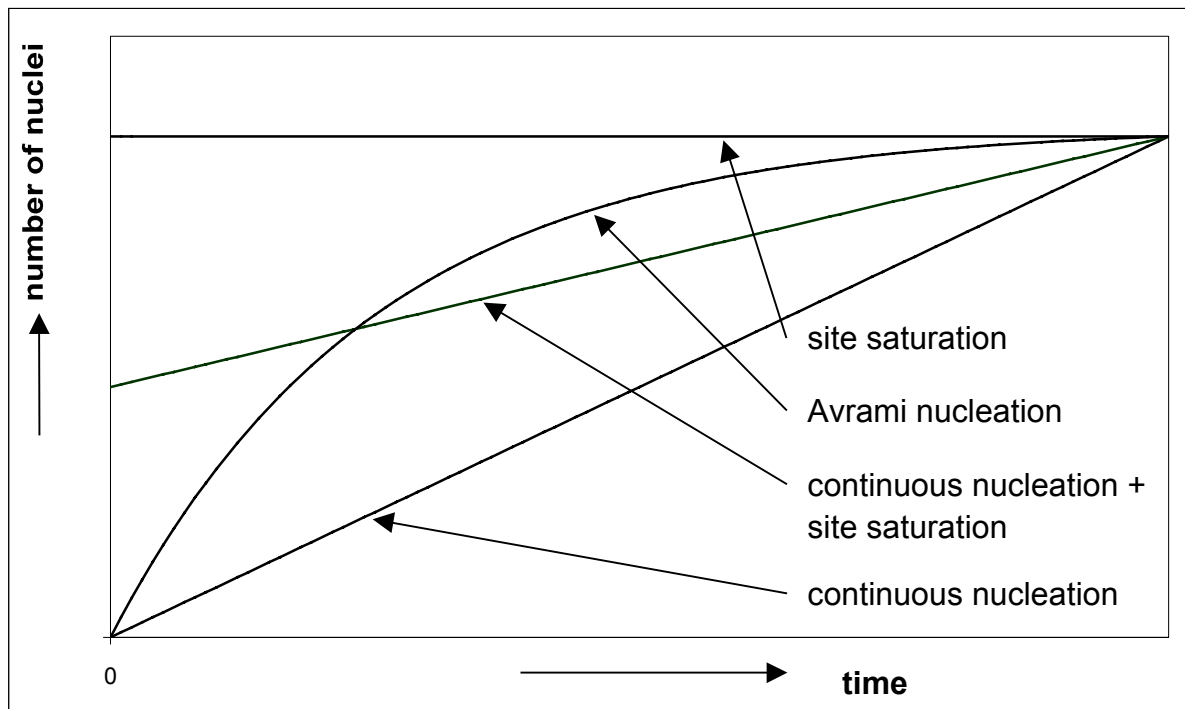


Fig.8.1 Schematische Darstellung der Anzahl der Keime als Funktion der Zeit bei konstanter Temperatur für verschiedene Keimbildungsmodelle.

Zwei Grenzfälle sind angegeben: ‚site saturation‘, wobei alle wachstumsfähigen Keime vorhanden sind bevor das Wachstum beginnt und kontinuierliche Keimbildung, wobei alle wachstumsfähigen Keime während der Umwandlung gebildet werden und die Keimbildungsrate nicht vom Verlauf des Umwandlungsprozesses abhängt.

8.2.2 Wachstum

Das Wachstum der Teilchen erfolgt durch Volumendiffusion oder Grenzflächendiffusion. Im ersten Fall bestimmt ein parabolisches Wachstumsgesetz die Grenzflächengeschwindigkeit, d.h. die Geschwindigkeit der Grenzfläche ist proportional zur Zeit im Quadrat (isothermer Fall). Bei grenzflächenkontrolliertem Wachstum ist die Geschwindigkeit der Grenzflächen entweder durch die Triebkraft für die Umwandlung oder durch die Beweglichkeit der

Grenzfläche bestimmt. Wenn nur die chemische Triebkraft betrachtet wird, ist die Triebkraft konstant, falls eine polymorphe Umwandlung isotherm stattfindet. In diesem Fall sind die Grenzflächenbeweglichkeit und auch die Grenzflächengeschwindigkeit konstant. Die Triebkraft ist jedoch nicht geschwindigkeitsbestimmend, falls die Umwandlung bei großer Unterkühlung oder Überhitzung stattfindet: hier bestimmt die Grenzflächenbeweglichkeit die Wachstumsgeschwindigkeit.

Falls die Triebkraft (teilweise) geschwindigkeitsbestimmend ist, werden auch Prozesse wichtig, die Energie verzehren, und damit die gesamte Triebkraft verringern. Bei *Festkörperphasenumwandlungen* kann der Aufbau von mechanischen Spannungen eine solche Rolle spielen.

8.2.3 Zusammenstoßen

Die Berechnung von dem real umgewandelten Volumens aus dem ‚extended volume‘ ist abhängig von mehreren Parametern. Erstens ist festzulegen ob die Teilchen beim Wachstum physisch zusammenstoßen (‚hard impingement‘) oder ob die Diffusionsfelder zusammenstoßen und damit das Wachstum nicht angehalten sondern verlangsamt wird (‚soft impingement‘). Zweitens spielt die Verteilung der Teilchen in der Matrix eine Rolle. Wenn die Teilchen homogen verteilt sind, kann ein Zusammenstoßen von wachsenden Teilchen direkt am Anfang des Wachstums stattfinden (obwohl das nicht sehr wahrscheinlich ist). Wenn die Teilchen mehr periodisch verteilt sind, findet das Zusammenstoßen der Teilchen erst später statt. Das Verhältnis zwischen dem ‚extended volume‘, x_e , und dem real umgewandelten Volumenanteil, f , wird in Fig.8.2 für verschiedene Modelle gezeigt. Als Begrenzung von möglichen Modellbeschreibungen für das Zusammenstoßen von wachsenden Teilchen, für den Fall das ein Zusammenstoßen nicht stattfindet, ergibt sich: $f=x_e$ für $x_e \leq 1$ sowie $f=1$ für $x_e > 1$ (s. Fig.8.2).

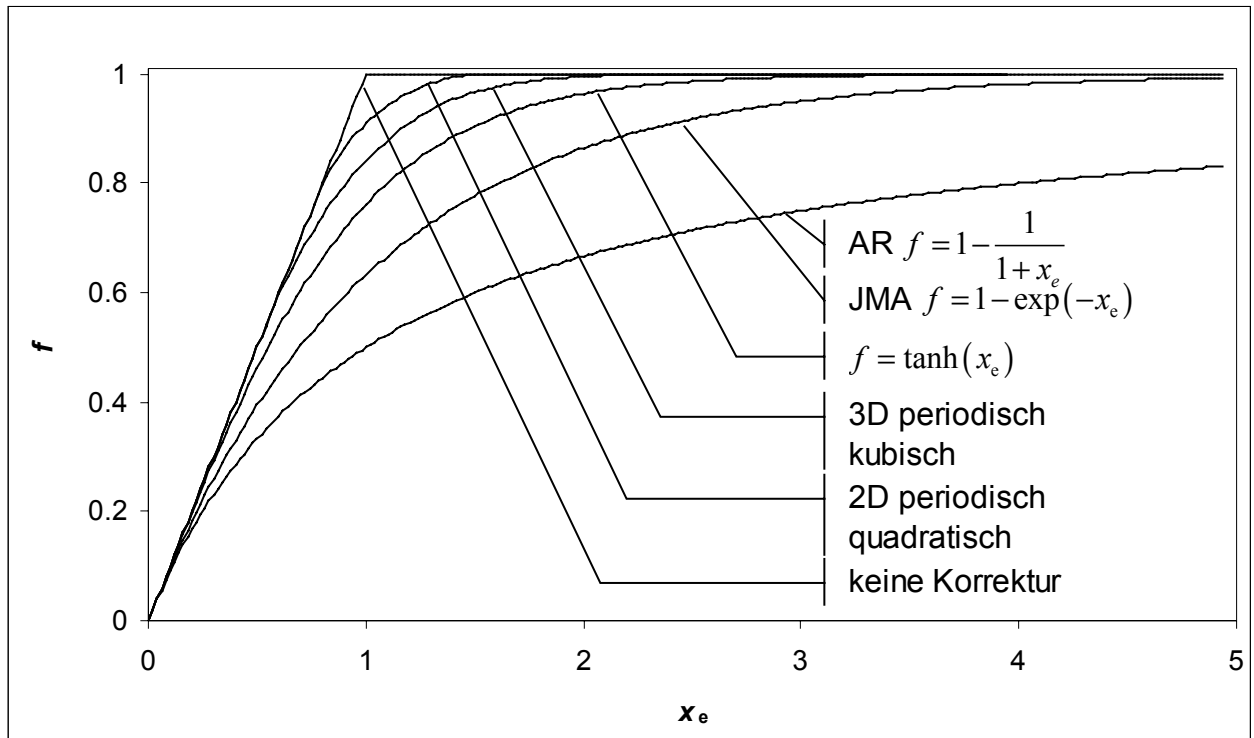


Fig.8.2 Das Verhältnis zwischen dem ‚extended volume‘, x_e , und dem real umgewandelten Volumenanteil, f , für unterschiedliche Modelle: Johnson-Mehl-Avrami (JMA), Austin-Rickett (AR), nach Gleichung $f = \tanh(x_e)$, ohne Korrektur, und für ideal periodisch verteilt wachsende Teilchen auf einem primitiv kubischem (3-dimensional), oder quadratischem (2-dimensional) Gitter.

Die Korrektur für das Zusammenstoßen nach dem Johnson-Mehl-Avrami Modell (JMA) geht von der Annahme aus, daß die wachsenden Teilchen homogen verteilt sind [2, 32]. Eine regelmäßigerere Verteilung würde zu einem kleineren Einfluß der Korrektur führen, d.h. der Unterschied zwischen x_e und f wäre kleiner. Als Beispiele werden die Korrekturen für ideal periodisch verteilte wachsende Teilchen auf einem primitiv kubischem (3-dimensional, berechnet mit einer Monte-Carlo Simulation [24]) und quadratischem (2-dimensional, analytisch berechnet) Gitter in Fig.8.2 gezeigt. Eine in dieser Arbeit entwickelte Korrekturfunktion, $f = \tanh(x_e)$, wird ebenfalls in Fig.8.2 gezeigt, die zwischen den Korrekturfunktionen für ideal periodisch verteilte und für ideal homogen verteilte Teilchen liegt. Diese Funktion ist damit für die Korrektur des Zusammenstoßens von nicht-ideal periodisch verteilten Teilchen geeignet. Der Effekt von ‚soft impingement‘, d.h. das Zusammenstoßen der Diffusionsfelder bei volumendiffusionskontrollierten Wachstumsvorgängen [108] ist auch in Fig.8.2 mit der Austin-Rickett [109] Korrekturfunktion gezeigt.

8.2.4 Numerische Modellüberprüfung

Das allgemeine kinetische Modell, das in dieser Arbeit entwickelt wurde, führt in spezifischen Fällen der Kombination von Keimbildungs- und Wachstumsmodellen zu dem viel angewandten JMA Modell. Die Kombination von Keimbildung („site saturation“ oder kontinuierliche Keimbildung) und Wachstum (kontrolliert durch Volumendiffusion oder durch Grenzflächenbeweglichkeit) ergibt die Beschreibung nach dem JMA Modell. Zwischenliegende Keimbildungsprozesse (s. Fig.8.1) führen jedoch nicht zum JMA Modell. Es konnte in dieser Arbeit aber numerisch nachgewiesen werden, daß das JMA Modell eine gute Beschreibung für eine hypothetische Phasenumwandlung ergibt, die nach dem allgemeinen kinetischen Modell mit beiden zwischenliegenden Keimbildungsmodellen (kombiniert mit Wachstum, kontrolliert entweder durch Volumendiffusion oder durch Grenzflächenbeweglichkeit und der JMA Korrektur für das Zusammenstoßen der wachsenden Teilchen) stattfindet. Die effektive (JMA) Aktivierungsenergie wird in diesem Fall gegeben durch

$$Q = \frac{\frac{d}{m}Q_g + (n - \frac{d}{m})Q_N}{n}, \quad (8.1)$$

wobei d die Anzahl der Richtungen ist, in der das Teilchen wächst, Q_N und Q_g sind jeweils die Aktivierungsenergien für Keimbildung und Wachstum, n ist der JMA-Exponent und m ist ein Parameter, der für diffusionsgesteuertes Wachstum 0.5 beträgt, und wenn das Wachstum durch die Grenzflächenbeweglichkeit kontrolliert ist, 1 beträgt. Diese Gleichung ermöglicht eine Bestimmung der Aktivierungsenergien für Keimbildung und Wachstum, wenn die effektive Aktivierungsenergie als Funktion von dem JMA-Exponenten bestimmt wird und wenn d/m bekannt ist.

8.3 Experimentelles

Die in dieser Arbeit behandelten Umwandlungen sind mit unterschiedlichen Techniken untersucht worden. Die Freisetzung von Reaktionswärme ist in dieser Arbeit bei niedrigen Temperaturen mit einem leistungs-kompensierten Differential Scanning Kalorimeter (DSC) und bei höheren Temperaturen ($T > 1000\text{K}$) mit einer Differential Thermo Analyse (DTA) untersucht worden. Aus den Meßsignalen von DTA und DSC ist die Entwicklung des umgewandelten Anteils als Funktion der Zeit (und/oder Temperatur) für unterschiedliche Heiz- oder Kühlraten zu extrahieren. Kenntnisse von dem umgewandelten Anteil als Funktion von Zeit/Temperatur und Heiz- oder Kühlrate ermöglichen die Anwendung des allgemeinen kinetischen Modells und somit Aussagen über die geschwindigkeitsbestimmenden Prozesse.

Die untersuchten Umwandlungen sind identifiziert mit Guinier Röntgenbeugungsanalyse und Röntgendiffraktometrie zur Bestimmung der auftretenden Phasen. Weiter wurden Lichtmikroskopie, Raster Elektronen Mikroskopie (REM) und Transmission Elektronen Mikroskopie (TEM), kombiniert mit Elektronen-Energieverlust-Spektroskopie (EELS) für die Charakterisierung der Mikrostruktur angewandt.

8.4 Ergebnisse

8.4.1 Kristallisation von amorphem $\text{Pd}_{40}\text{Cu}_{30}\text{P}_{20}\text{Ni}_{10}$

Die amorphe Legierung $\text{Pd}_{40}\text{Cu}_{30}\text{P}_{20}\text{Ni}_{10}$ ist hergestellt durch Abschrecken der geschmolzenen Legierung in Wasser. Die Kristallisationskinetik wurde mit der DSC-Methode untersucht und die Mikrostruktur wurde nach der Kristallisation mit REM charakterisiert. Die REM Bilder ergaben, daß nach der Kristallisation bei konstanter Heizrate eine Mikrostruktur vorlag, welche (wahrscheinlich) das Resultat von dreidimensionalem Wachstum ist: $d/m = 1.5$. Durch eine isotherme Vorauslagerung bei unterschiedlichen Temperaturen war es möglich, den Keimbildungsmodus graduell von ‚site saturation‘ zu kontinuierlicher Keimbildung zu ändern. Das ermöglicht nach Gl.(8.1) die Bestimmung der einzelnen Aktivierungsenergien für Keimbildung und Wachstum.

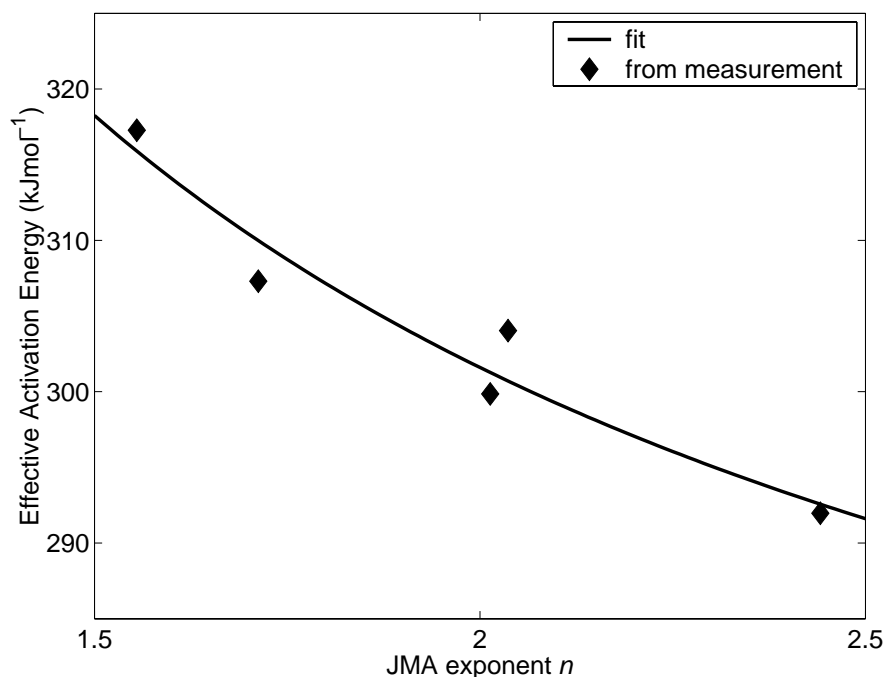


Fig.8.3 Die effektive Aktivierungsenergie als Funktion der JMA-Exponenten, wie gemessen(♦) und wie angepasst nach Gl.(8.1) (Linie) mit $d/m=3/2$.

Die Aktivierungsenergien für Keimbildung und Wachstum betragen jeweils $Q_N=252$ kJ/mol und $Q_g=318$ kJ/mol.

8.4.2 Kristallisation von amorphem $Mg_{50}Ni_{30}La_{20}$

Die amorphe Legierung $Mg_{50}Ni_{30}La_{20}$ wurde durch das Schmelzspinverfahren hergestellt. DSC Untersuchungen bei konstanter Heizrate wurden für die Bestimmung der Umwandlungskinetik durchgeführt, wobei der Einfluß von unterschiedlichen isothermen Vorauslagerungen auf die Umwandlungskinetik untersucht wurden. Die Kristallisation findet in zwei aufeinanderfolgenden, zeitlich überlappenden Umwandlungen statt. Das allgemeine Umwandlungsmodell ist angepaßt, um diese zwei Umwandlungen beschreiben zu können. Dafür ist angenommen, daß der zweite Umwandlungsspeak vom Verlauf der ersten Umwandlung abhängt: das Ausgangsmaterial für die zweite Umwandlung ist das Reaktionsprodukt der ersten Umwandlung, und der zweiten Umwandlung wird es erst erlaubt bei einem bestimmten umgewandelten Anteil der ersten Umwandlung anzufangen.

Die kinetischen Parameter der ersten Umwandlung sind abhängig von der Vorauslagerung, die der zweiten Umwandlung aber nicht und letztere deuten weiterhin auf grenzflächenbeweglichkeitskontrolliertes Wachstum in drei Richtungen hin sowie das Vorliegen von allen Keimen bevor die zweite Umwandlung anfängt.

8.4.3 Kristallisation amorpher Legierungen der Systeme Mg-Ni und Mg-Cu

Amorphe magnesium-reiche Legierungen Mg_yX_{1-y} ($X= Ni, Cu$ und $0.82 < y < 0.89$) sind durch rasche Erstarrung der flüssigen Legierung mit dem Schmelzspinverfahren hergestellt. Der Verlauf der Kristallisation wurde mit isothermen und isochronen DSC Messungen, sowie mit zeitaufgelöster Hoch-Temperatur Diffraktometrie untersucht. Die auftretenden Phasen sind mit Guinier- und Diffraktometer Röntgenbeugungsanalyse identifiziert, und die Mikrostruktur ist mit TEM und EELS charakterisiert.

Der Kristallisationsmechanismus der Mg-Cu Legierungen ist abhängig von der Temperatur: bei hoher Temperatur findet die Kristallisation in zwei Stufen statt, bei niedriger Temperatur kristallisieren die Mg-Cu Legierungen in nur einer Stufe (s. Fig.8.4).

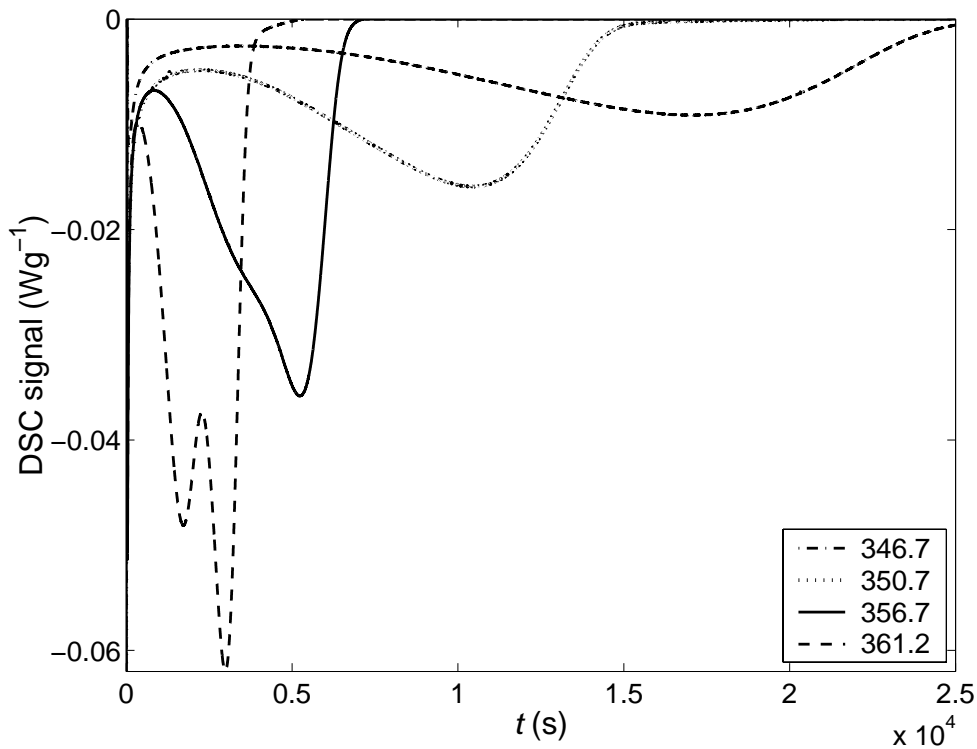


Fig.8.4 Isotherme DSC Messungen einer amorphen $Mg_{85.5}Cu_{14.5}$ Legierung bei den angegebenen Temperaturen. Das DSC Signal von jedem Meßlauf ist so verschoben, daß am Ende der Messung, wo die Kristallisation beendet, das DSC Signal gleich null gesetzt ist.

Die Kristallisation bei tiefen Temperaturen konnte mit dem Modell für grenzflächengeschwindigkeitskontrolliertes Wachstum in drei Richtungen kombiniert mit kontinuierlicher Keimbildung beschrieben werden. Dieses Modell wird durch die beobachtete Mikrostruktur bestätigt: das Vorliegen eines lamellaren Gefüges von abwechselnd Mg und Mg_2Cu Lamellen. Die Kristallisation bei höheren Temperaturen findet in zwei Prozessen statt, wovon der erste (wahrscheinlich) die primäre Ausscheidung von Mg darstellt, und der zweite Prozeß dem bei niedriger Temperatur auftretenden entspricht.

Kristallisation der Mg-Ni Legierungen ist stark abhängig von der Zusammensetzung. Für ein Mg-Gehalt von $y > 0.85$ findet die Umwandlung in zwei Stufen statt: primäre Ausscheidung von Mg und der in dieser Arbeit identifizierten metastabilen Phase $Mg_{-5.5}Ni$ (mit Mg-Gehalt von $y = 0.85$), gefolgt von der Umwandlung des $Mg_{-5.5}Ni$ in Mg und Mg_2Ni . Kristallisation der Mg-Ni Legierung mit einem Mg-Gehalt von $y < 0.85$ findet hauptsächlich in einer Stufe statt: eutektische Kristallisation von Mg und Mg_2Ni .

8.4.4 Austenit-Ferrit Umwandlung einer Fe-Mn Legierung

Die Differential Thermo Analyse (DTA) wurde verwendet, um die Austenit zu Ferrit

Umwandlung beim Abkühlen zu verfolgen. Dafür ist in dieser Arbeit eine neue Kalibrierungs- und Entschmiermethode entwickelt, die die DTA Signalverzerrungen beim Aufheizen sowie beim Abkühlen gleichermaßen bestimmt. Diese Messungen wurden unter anderem für die ferro-paramagnetische Umwandlung bei reinem Eisen durchgeführt.

Die Ergebnisse der DTA Messungen an Fe-1.89at% Mn zeigen eine zweistufige Umwandlung, wobei die erste Stufe nicht thermisch aktiviert ist. Das allgemeine kinetische Modell ist angewandt, mit Keimbildung nach ‚site saturation‘, einer kombinierten Grenzflächengeschwindigkeit $v=M(T)[-\Delta G_{\alpha\gamma}(T,f)]$, die von der Beweglichkeit $M(T)$ und von der Triebkraft $\Delta G_{\alpha\gamma}(T,f)$ abhängt, und mit der Korrektur für das Zusammenstoßen der wachsenden Teilchen nach $f = \tanh(x_c)$. An Hand der DTA-Messungen kann mit dem kinetischen Modell die Grenzflächengeschwindigkeit berechnet werden:

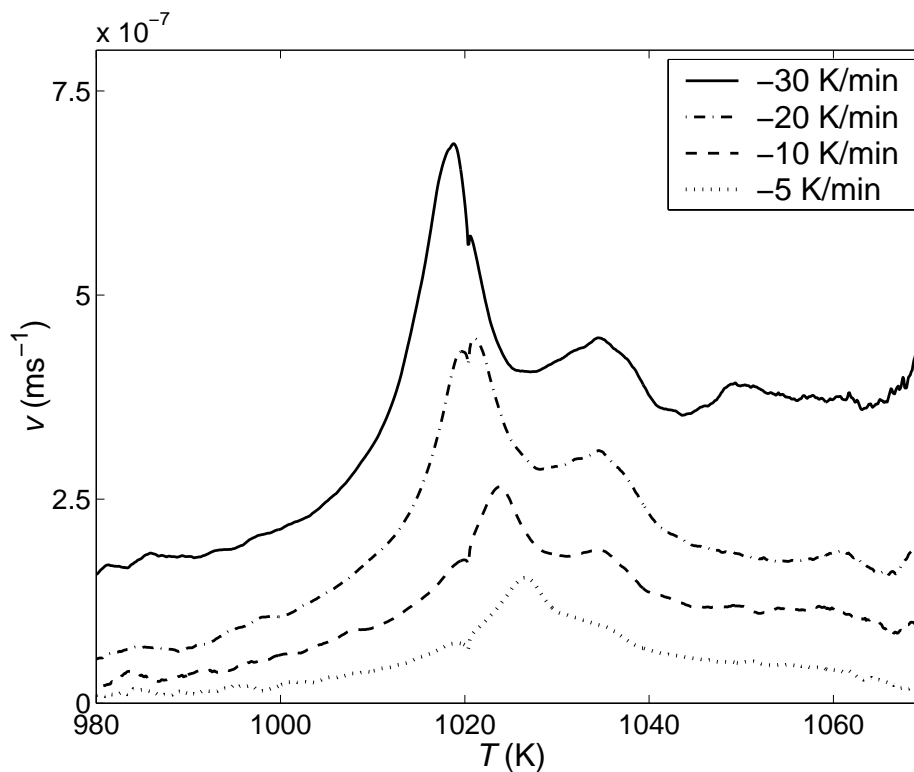


Fig.8.5 Geschwindigkeit der Grenzfläche zwischen Austenit und Ferrit für die angegebenen unterschiedlichen Kühlraten.

In der Literatur wird die gesamte Triebkraft oft durch die chemische Triebkraft angenähert. In diesem Fall ergäbe sich eine Triebkraft, die ausschließlich von der Temperatur abhängt, und damit würde die Grenzflächengeschwindigkeit auch nur von der Temperatur abhängen. In Fig.8.5 ist es aber klar gezeigt, dass die Grenzflächengeschwindigkeit nicht nur von der Temperatur abhängt. Literaturdaten der Beweglichkeit $M(T)$ und der chemischen Triebkraft

$\Delta G_{\alpha\gamma}^{chem}(T)$ ermöglichen die Berechnung der Dissipation der Triebkraft durch Deformation ($\Delta G_{\alpha\gamma}^{def}(f)$) und Aufbau der Grenzfläche ($\Delta G_{\alpha\gamma}^{int}(f)$) unter der Annahme, daß $\Delta G_{\alpha\gamma}^{def}(f) + \Delta G_{\alpha\gamma}^{int}(f) = \Delta G_{\alpha\gamma}(T, f) - \Delta G_{\alpha\gamma}^{chem}(T)$.

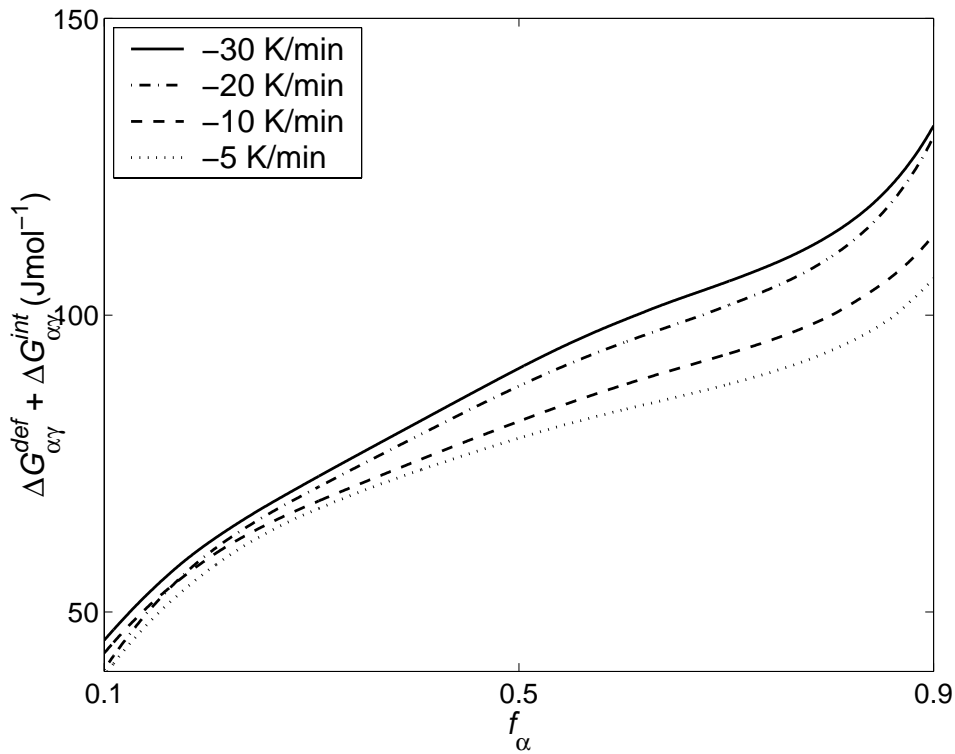


Fig.8.6 Die Dissipation durch Deformation und Aufbau der Grenzfläche als Funktion des Ferrit-Anteils, für die angegebenen Kühlraten.

$\Delta G_{\alpha\gamma}^{def}(f) + \Delta G_{\alpha\gamma}^{int}(f)$ sind in der gleichen Größenordnung wie die chemische Triebkraft, was zeigt, daß die Vernachlässigung von $\Delta G_{\alpha\gamma}^{def}(f) + \Delta G_{\alpha\gamma}^{int}(f)$ hier nicht zu sinnvollen Ergebnissen führen würde.

References

1. Cahn, J.W. *Challenges of Paradigm Building for Solid-State Transformations*. in *PTM'99*. 1999. Kyoto: The Japan Institute of Metals. p. 3-14.
2. Christian, J.W., *The theory of transformations in metals and alloys*. 1965: Pergamon Press, Oxford.
3. Porter, D.A. and K.E. Easterling, *Phase Transformations in Metals and Alloys*. 1981: Chapman and Hall. p. 189.
4. Dieter, G.E., *Mechanical Metallurgy*. 3rd ed. 1988, London: Mc Graw Hill. 751.
5. Johnson, W.A. and R.F. Mehl, *Reaction Kinetics in Processes of Nucleation and Growth*. *Trans. Am. Inst. Min. (Metall.) Eng.*, 1939. **135**: p. 416-41.
6. Avrami, M., *Kinetics of Phase Change I (General Theory)*. *J. Chem. Phys.*, 1939. **7**: p. 1103-12.
7. Avrami, M., *Kinetics of Phase Change II (Transformation-Time Relation for Random Distribution of Nuclei)*. *J. Chem. Phys.*, 1940. **8**: p. 212-24.
8. Avrami, M., *Kinetics of Phase Change III (Granulation, Phase Change, and Microstructure)*. *J. Chem. Phys.*, 1941. **9**: p. 177-84.
9. Mittemeijer, E.J., *Analysis of the kinetics of phase transformations*. *J. Mat. Sci.*, 1992. **27**: p. 3977-87.
10. Bruijn, T.J.W.d., W.A.d. Jong, and P.J.v.d. Berg, *Kinetic parameters in Avrami-Erofeev type reactions from isothermal and non-isothermal experiments*. *Thermochim. Acta*, 1980. **45**: p. 315-25.
11. Greer, A.L., *Crystallisation kinetics of Fe₈₀B₂₀ glass*. *Acta Met.*, 1982. **30**: p. 171-92.
12. Woldt, E., *The relationship between isothermal and non-isothermal description of johnson-mehl-avrami-kolmogorov kinetics*. *J. Phys. Chem. Solids*, 1992. **53**(4): p. 521-7.
13. Krüger, P., *On the relation between non-isothermal and isothermal Kolmogorov-Johnson-Mehl-Avrami Crystallization kinetics*. *J. Phys. Chem. Solids.*, 1993. **54**(11): p. 1549-55.
14. Shewmon, P., *Diffusion in Solids*. 1989: The Minerals, Metals & Materials Society. p. 37.
15. Ham, F.S., *Theory of diffusion-limited precipitation*. *J. Phys. Chem. Solids*, 1958. **6**: p. 335-51.
16. Ranganathan, S. and M.v. Heimendahl, *The three activation energies with isothermal*

- transformations: applications to metallic glasses*. J. Mat. Sci., 1981. **16**: p. 2401-4.
17. Berkenpas, M.B., J.A. Barnard, R.V. Ramanujan, and H.I. Aaronson, *A critique of activation energies for nucleation growth and overall transformation kinetics*. Scripta Metallurgica, 1986. **20**(3): p. 323-8.
 18. Kelton, K.F., *Numerical model for isothermal and non-isothermal crystallization of liquids and glasses*. J. non-cryst. sol., 1993. **163**(3): p. 283-96.
 19. Von Heimendahl, M. and G. Maussner, *The metastable crystallization phases in the amorphous alloy METGLAS 2826A*. J. Mat. Sci., 1979. **14**(5): p. 1238-44.
 20. Benedictus, R., A. Böttger, and E.J. Mittemeijer, *Thermal analysis of solid state amorphization: predicted and measured reaction enthalpies and reaction kinetics*. Zeitschrift für Metallkunde, 1998. **89**(3): p. 168-76.
 21. Abramowitz, M. and I.A. Stegun, *Handbook of Mathematical Functions*. 1965: Dover Publications, Inc. New York. Ch. 5.
 22. Borrego, A. and G. Gonzalez-Doncel, *Analysis of the precipitation behavior in aluminum matrix composites from a Johnson-Mehl-Avrami kinetic model*. Mat. Sci. Eng., 1998. **A252**: p. 149-52.
 23. Krüger, P. and E. Woldt, *The use of an activation energy distribution for the analysis of the recrystallization kinetics of copper*. Acta met. mat., 1992. **40**(11): p. 2933-42.
 24. Press, W.H., S.A. Teukolsky, W.T. Vetterling, and B.P. Flannery, *Numerical Recipes in C*. 1997, NY: Cambridge University Press. p. 408.
 25. Kempen, A.T.W., F. Sommer, and E.J. Mittemeijer, *The Isothermal and Isochronal Kinetics of Crystallisation of Bulk Amorphous Pd₄₀Cu₃₀P₂₀Ni₁₀*. submitted for publication, 2001.
 26. Blanke, H. and U. Köster. *Crystallization statistics in metal-metalloid glasses*. in *Rapidly quenched metals*. 1985: Elsevier Science Publishers B.V. p. 227-30.
 27. Duine, P.A., *Atomic Mobility and Structural Relaxation in Amorphous PdNiP*, in *Department of Materials Science and Technology*. 1994, Delft University of Technology: Delft p. 163
 28. Mehrer, H., ed. *Diffusion in Solids and Alloys*. . Vol. III/26. 1990, Springer-Verlag.
 29. Inoue, A., N. Nishiyama, and T. Matsuda, *Preparation of bulk glassy Pd₄₀Ni₁₀Cu₃₀P₂₀ alloy of 40 mm in diameter by water quenching*. Materials Transactions JIM, 1996. **37**(2): p. 181-4.
 30. Inoue, A., N. Nishiyama, and H. Kimura, *Preparation and thermal stability of bulk*

- amorphous Pd₄₀Cu₃₀Ni₁₀P₂₀ alloy cylinder of 72 mm in diameter.* Materials Transactions JIM, 1997. **38**(2): p. 179-83.
31. Nishiyama, N. and A. Inoue, *Glass transition behavior and viscous flow working of Pd₄₀Cu₃₀Ni₁₀P₂₀ amorphous alloy.* Materials Transactions JIM, 1999. **40**(1): p. 64-71.
 32. Kempen, A.T.W., F. Sommer, and E.J. Mittemeijer, *Determination and interpretation of isothermal and non-isothermal transformation kinetics; the effective activation energies in terms of nucleation and growth.* submitted for publication, 2000.
 33. Cahn, J.W., *The kinetics of grain boundary nucleated reactions.* Acta Met., 1956. **4**: p. 449-59.
 34. Grong, O. and O.R. Myhr, *Additivity and isokinetic behaviour in relation to diffusion controlled growth.* Acta Mat., 2000. **48**(2): p. 445-52.
 35. Russev, K., L. Stojanova, and F.Sommer, *Preparation of Bulk and Ribbon-like Amorphous Metallic Alloys and Study of Their Structure and Rheological Properties. Part I: Preparation and Structural Study.* J.Mat.Sci.Tech., 2000. **8**(1): p. 25-33.
 36. Inoue, A. and N. Nishiyama, *Extremely low critical cooling rates of new Pd-Cu-P base amorphous alloys.* Mat. Sci. Eng. A, 1997. **226**: p. 401-5.
 37. Kim, J.-H., S.-G. Kim, and A. Inoue, *In Situ Observation of solidification behavior in undercooled Pd-Cu-Ni-P alloy by using a confocal scanning laser microscope.* Acta Mat., 2001. **49**: p. 615-22.
 38. Lu, I.R., G. Wilde, G.P. Gorler, and R. Willnecker, *Thermodynamic properties of Pd-based glass-forming alloys.* J. non-cryst. sol., 1999. **252**: p. 577-81.
 39. Kempen, A.T.W., H. Nitsche, F. Sommer, and E.J. Mittemeijer, *Crystallisation kinetics of amorphous magnesium-rich magnisum-copper and magnesium-nickel alloys.* submitted for publication, 2001.
 40. Blank-Bewersdorff, M. and U. Koster, *Transient nucleation in zirconium-based metallic glasses.* Mat. Sci. Eng., 1988. **97**: p. 313-16.
 41. Duine, P.A., J. Sietsma, A.v.d. Beukel, and A.M. Vredenberg, *Time-dependent diffusivity of Au in amorphous Pd₄₀Ni₄₀P₂₀ measured by Rutherford-backscattering spectrometry.* Nuc. Instr. and Methods B, 1992. **71**: p. 445-50.
 42. Sommer, F., G. Bucher, and B. Predel, *Thermodynamic investigations of Mg -Cu and Mg -Ni metallic glasses.* Journal de Physique Colloque, 1980. **41**(C): p. 563-6.
 43. Friedlmeier, G., M. Arakawa, T. Hirai, and E. Akiba, *Preparation and structural,*

- thermal and hydriding characteristics of melt-spun Mg-Ni alloys.* J. All. Comp., 1999. **292**(1-2): p. 107-17.
44. Feufel, H. and F. Sommer, *Thermodynamic Investigations of Binary-Liquid and Solid Cu-Mg and Mg-Ni Alloys and Ternary Liquid Cu-Mg-Ni Alloys.* J. All. Comp., 1995. **224**(1): p. 42-54.
45. Micke, K. and H. Ipsier, *Thermodynamic properties of liquid magnesium-nickel alloys.* Monatshefte für Chemie, 1996. **127**(1): p. 7-13.
46. Nizhenko, V.I., L.I. Floka, and G.P. Khilya, *Composition and Thermodynamic Properties of the Surface-Layer of Binary Melts of Magnesium With Copper, Tin and Lead.* Russian Metallurgy, 1993(5): p. 45-7.
47. Schubert, K. and K. Anderko, *Kristallstruktur von NiMg₂, CuMg₂ und AuMg₃.* Zeits.Metallk., 1951. **42**(11): p. 321-5.
48. Bagnoud, P. and P. Feschotte, *Binary-Systems Magnesium-Copper and Magnesium-Nickel, Especially Non-Stoichiometry of MgCu₂ and MgNi₂ Laves Phases.* Zeitschrift für Metallkunde, 1978. **69**(2): p. 114-20.
49. Gingl, F., P. Selvam, and K. Yvon, *Structure Refinement of Mg₂Cu and a Comparison of the Mg₂Cu, Mg₂Ni and Al₂Cu Structure Types.* Acta Cryst., 1993. **B49**: p. 201-3.
50. Köster, U. and U. Herold, *Crystallization of Metallic Glasses,* in *Glassy metals I, Ionic Structure, Electronic Transport and Crystallization,* H.-J. Günterodt and H. Beck, Editors. 1981.
51. Tiller, W.A., *The Science of Crystallization, Macroscopic Phenomena and Defect Generation.* 1991, Cambridge: Cambridge University Press. 484.
52. Telleria, I. and J.M. Barandiaran, *Kinetics of the primary, eutectic and polymorphic crystallization of metallic glasses studied by continuous scan methods.* Thermochem. Acta, 1996. **280/281**: p. 279-87.
53. Wang, W.H., Y.X. Zhuang, M.X. Pan, and Y.S. Yao, *Glass transition behavior, crystallization kinetics, and microstructure change of Zr₄₁Ti₁₄Cu_{12.5}Ni₁₀Be_{22.5} bulk metallic glass under high pressure.* J. Applied Physics, 2000. **88**(7): p. 3914-8.
54. Massalski, T.B., ed. *Binary Alloy Phase Diagrams.* 2 ed. . 1990, ASM International.
55. Bakonyi, I., F. Mehner, M. Rapp, A. Cziraki, H. Kronmüller, and R. Kirchheim, *Preparation, Structure and Physical Properties of Fe-, Co and Ni-rich Melt-quenched Ribbons Containing Zr or Hf. Part I: Preparation Details and Structural Characterization.* Zeitschrift für Metallkunde, 1995. **86**(9): p. 619-25.

-
56. (US), N.B.S., Monogr., 1984. **25**(21): p. 21.
 57. Yvon, K., W. Jeitschko, and E. Parthe, *LAZY PULVERIX, a computer program, for calculating X-ray and neutron diffraction powder patterns*. J. appl. Cryst., 1977. **10**(1): p. 73-4.
 58. Daams, J.L.C., P. Villars, and J.H.N.v. Vucht, eds. *Atlas of Crystal Structure Types for Intermetallic Phases*. . Vol. 4. 1991, ASM International: Ohio.
 59. Kreiner, G. and H.F. Franzen, *A new cluster concept and its application to quasi-crystals of the i-AlMnSi family and closely related crystalline structures*. J.All.Comp., 1995. **221**: p. 15-36.
 60. Chabot, B., K. Cenxual, and E. Parthe, *Sc₄₄os₇ and Sc₄₄ir₇ With the Mg₄₄rh₇ Structure Type*. Acta Cryst. B, 1980. **36**(OCT): p. 2202-5.
 61. Gmelin, E. and S.M. Sarge, *Temperature, heat and heat flow rate calibration of differential scanning calorimeters*. Thermochim. Acta, 2000. **347**(1-2): p. 9-13.
 62. Höhne, G.W.H., H.K. Cammenga, W. Eysel, E. Gmelin, and W. Hemminger, *The Temperature Calibration of Scanning Calorimeters*. Thermochim. Acta, 1990. **160**(1): p. 1-12.
 63. Cammenga, H.K., W. Eysel, E. Gmelin, W. Hemminger, G.W.H. Höhne, and S.M. Sarge, *The Temperature Calibration of Scanning Calorimeters .2. Calibration Substances*. Thermochim. Acta, 1993. **219**: p. 333-42.
 64. Speyer, R.F., *Thermal analysis of materials*. 1994, New York: Marcel Dekker Inc.
 65. Menczel, J.D., *Temperature calibration of heat flux DSC's on cooling*. J. Thermal Analysis, 1997. **49**(1): p. 193-9.
 66. *Pyris Software for Windows*, . 1999, Perkin Elmer
 67. *Netzsch Messung*, . 1999, Netzsch: Selb
 68. Höhne, G.W.H., J. Schawe, and C. Schick, *Temperature Calibration On Cooling Using Liquid-Crystal Phase- Transitions*. Thermochim. Acta, 1993. **221**(1): p. 129-37.
 69. Schick, C. and G.W.H. Höhne, *On Temperature Calibration of Power Compensation DSC in Cooling Mode*. Thermochim. Acta, 1991. **187**: p. 351-6.
 70. Sarge, S.M., G.W.H. Höhne, H.K. Cammenga, W. Eysel, and E. Gmelin, *Temperature, heat and heat flow rate calibration of scanning calorimeters in the cooling mode*. Thermochim. Acta, 2000. **361**(1-2): p. 1-20.
 71. Flammersheim, H.J., N. Eckardt, and W. Kunze, *The Deconvolution of Dsc-Curves in the Experimental Time Domain*. Thermochim. Acta, 1991. **187**: p. 269-74.
 72. Wiesner, S. and E. Woldt, *An Algorithm For the Reconstruction of the True Specimen*

- Signal of a Differential Scanning Calorimeter*. Thermochim. Acta, 1991. **187**: p. 357-62.
73. Krielaart, G.P. and S. van der Zwaag, *Kinetics of gamma - alpha phase transformation in Fe-Mn alloys containing low manganese*. Mat. Sci. Tech., 1998. **14**(1): p. 10-8.
74. Poessnecker, W., *Theoretical Investigations of the Heat-Transfer At Quantitative DSC-Measurements and Its Influence On the Determination of the Thermal and Calorimetric Properties*. Thermochim. Acta, 1991. **187**: p. 309-22.
75. Schönborn, K.H., *On the Time-Lag Between Thermal Event and Measuring Signal in a Heat-Flux Calorimeter*. Thermochim. Acta, 1983. **69**(1-2): p. 103-14.
76. Wang, X.Y., Y.K. Hou, and C.N. Wu, *Method For Correcting the Time-Lag of a Conduction Calorimeter and Its Application*. Thermochim. Acta, 1988. **123**: p. 177-82.
77. Nicolaus, M.M., *Reconstruction of the Original Heat-Flux Curve For a Calorimetric Measuring Device*. Thermochim. Acta, 1989. **151**: p. 345-51.
78. Kneller, E., *Ferromagnetismus*. 1st ed. 1962, Berlin: Springer-Verlag.
79. Bozorth, R.M., *Ferromagnetism*. 2nd ed. 1951, Toronto: D. van Nostrand company.
80. Jeong, Y.H., D.J. Bae, T.W. Kwon, and I.K. Moon, *Dynamic Specific-Heat Near the Curie-Point of Gd*. J. Appl. Phys, 1991. **70**(10): p. 6166-8.
81. Braun, M., *Über die spezifische Wärme von Eisen, Kobalt und Nickel im Bereich hoher Temperaturen*, . 1964, Universität zu Köln
82. Korn, J. and R. Kohlhaas, *Influence of a Magnetic Field On Specific Heat of Nickel and Iron in Environment of Curie Temperature*. Zeitschrift für Angewandte Physik, 1969. **26**(2): p. 119-&.
83. Pallister, P.R., *The Specific Heat and Resistivity of High-Purity Iron Up to 1250-Degrees-C*. J. the Iron and Steel Institute, 1949. **161**(2): p. 87-90.
84. Wallace, D.C., P.H. Sidles, and G.C. Danielson, *Specific Heat of High Purity Iron By a Pulse Heating Method*. J. Applied Physics, 1960. **31**(1): p. 168-76.
85. McElroy, D.L., . 1957, Tennessee
86. Picklesimer, M.L., . 1954, Tennessee
87. Rogez, J. and J. Lecoze, *Description and Standardization of Adiabatic Scanning Calorimeter (800 K-1800 K)*. Revue De Physique Appliquee, 1980. **15**(2): p. 341-51.
88. Bendick, W. and W. Pepperhoff, *On the Alpha Gamma-Phase Stability of Iron*. Acta Met., 1982. **30**(3): p. 679-84.
89. Awbery, J.H. and E. Griffiths, Proc.Roy.Soc, 1940. **A174**: p. 1-15.
90. Touloukian, Y.S. and E.H. Buyco, *Specific Heat, Metallic Elements and Alloys*.

- Thermophysical Properties of Matter, ed. Y.S. Touloukian. Vol. 4. 1970, New York: Plenum.
91. Dinsdale, A.T., *SGTE Data For Pure Elements*. Calphad, 1991. **15**(4): p. 317-425.
 92. Rao, C.N.R. and K.J. Rao, *Phase Transitions in Solids. An Approach to the Study of the Chemistry and Physics of Solids*. 1978, New York: McGraw-Hill international book company.
 93. Münster, A., *Statistical Thermodynamics*. Vol. II. 1974, Berlin: Springer-Verlag. 841.
 94. Cox, J.D., *Reports Issued By Commission On Physicochemical Measurements and Standards Sub-Commission On Calibration and Test Materials of Physical-Chemistry Division*. Pure and Applied Chemistry, 1974. **40**(3): p. 391-472.
 95. Wits, J.J., T.A. Kop, Y. van Leeuwen, J. Seitsma, and S. van der Zwaag, *A study on the austenite-to-ferrite phase transformation in binary substitutional iron alloys*. Mat. Sci. Eng. A, 2000. **283**(1-2): p. 234-41.
 96. Li, C.-M., F. Sommer, and E.J. Mittemeijer, *Characteristics of the gamma to alpha Transformation in Fe-Mn Alloys*. Mat. Sci. Eng A, 2001. **in press**.
 97. Enomoto, M., T. Sonoyama, and H. Yada, *Kinetics of austenite to ferrite transformation in 3 mass% Mn low carbon steels*. Materials Transactions JIM, 1998. **39**(1): p. 189-95.
 98. Bhadeshia, H.K.D.H., *Ferrite formation in heterogeneous dual-phase steels*. Scripta Metallurgica, 1983. **17**(7): p. 857-60.
 99. Lee, J.L., Y.T. Pan, and K.C. Hsieh, *Assessment of ideal TTT diagram in C-Mn steels*. Materials Transactions JIM, 1998. **39**(1): p. 196-202.
 100. Militzer, M., R. Pandi, and E.B. Hawbolt, *Ferrite nucleation and growth during continuous cooling*. Met. Mat. Trans A., 1996. **27**(6): p. 1547-56.
 101. Kempen, A.T.W., F. Sommer, and E.J. Mittemeijer, *Calibration and Desmearing of a Differential Thermal Analysis measurement signal upon heating and cooling*. Thermochem. Acta, 2001. **in press**.
 102. Troiano, A.R. and F.T. McGuire, *A Study of the Iron-rich Iron-Manganese alloys*. Trans. A.S.M, 1943. **31**: p. 340.
 103. Vandermeer, R.A., *Modeling Diffusional Growth During Austenite Decomposition to Ferrite in Polycrystalline Fe-C Alloys*. Acta Metallurgica Et Materialia, 1990. **38**(12): p. 2461-70.
 104. Hillert, M., *Diffusion and Interface Control of Reactions in Alloys*. Met. Trans. A., 1975. **6**(1): p. 5-19.
 105. Leitch, B.W. and S.Q. Shi, *Accommodation energy of formation and dissolution for a*

- misfitting precipitate in an elastic-plastic matrix*. Modelling and Simulation in Materials Science and Engineering, 1996. **4**(3): p. 281-92.
106. Vooijs, S.I., Y. Van Leeuwen, J. Sietsma, and S. Van der Zwaag, *On the mobility of the austenite-ferrite interface in Fe-Co and Fe-Cu*. Met. Mat. Trans. A, 2000. **31**(2): p. 379-85.
107. Liu, Z.K., *Theoretic calculation of ferrite growth in supersaturated austenite in Fe-C alloy*. Acta Mat., 1996. **44**(9): p. 3855-67.
108. Starink, M.J., *Kinetic equations for diffusion-controlled precipitation reactions*. J. Mat. Sci., 1997. **32**(15): p. 4061-70.
109. Austin, J.B. and R.L. Rickett, *Kinetics of the Decomposition of Austenite at Constant Temperature*. Metals Technology, 1938.
110. DIN, *DIN 50601; Ermittlung der Ferrit- oder Austenit- Korngröße von Stahl und Eisenwerkstoffen*, . 1985, Deutsches Institut für Normung e.V.
111. ASTM E112, *Standart Test Methods for Determining Average Grain Size*. Annual Book of ASTM Standards, 1988. **03.01**: p. 297-321.
112. Witusiewicz, V.T., F. Sommer, and E. Mittemeijer, *Thermodynamics of Fe-Mn Alloys*. to be submitted, 2001.
113. Yang, Z. and R.A. Johnson, *An Eam Simulation of the Alpha-Gamma Iron Interface*. Modelling and Simulation in Materials Science and Engineering, 1993. **1**(5): p. 707-16.

Curriculum Vitae

Personalien

Name: Antonius Theodorus Wilhelmus Kempen

Rufname: Antoine

Geboren: 9.12.1972 in Kamerik/Niederlande

Nationalität: Niederländisch

Ausbildung

1979-1985 Grundschule

1985-1991 Minkema Scholengemeenschap Woerden/Niederlande

Vorbereitender wissenschaftlicher Unterricht

1991-1997 Studium der Materialkunde an der Technischen Universität Delft

Diplomthema: Nitrieren von Fe-V und Charakterisieren der VN Einschlüsse

Beruflicher Werdegang

Nov. 1997 Wissenschaftlicher Mitarbeiter an der Technischen Universität Delft.

Feb. 1998- Doktorarbeit am Max-Planck-Institut für Metallforschung, Stuttgart, und am Institut für Metallkunde der Universität Stuttgart.

Danksagung

Eine Dissertation zu schreiben, ist ein langwieriges Geschäft, das nicht auf die schreibende Person beschränkt bleibt. Vielmehr werden praktisch alle Menschen mit hineingezogen, mit welchen mehr als oberflächlicher Kontakt besteht. Allen diesen gebührt Dank für ihre Ausdauer und Geduld. In starkem Maße wurde letzteres von meiner Freundin, Linda, abverlangt. Darüber hinaus möchte ich an dieser Stelle kurz denjenigen meinen Dank aufschreiben, die in der einen oder anderen Weise das speziell verdient haben.

Es gebührt sich aus gutem Grund, mit seinem Lehrer anzufangen. Besonders bedanken möchte ich mich bei meinem Doktorvater Eric Mittemeijer, der viel positiven Einfluß auf die Arbeit genommen hat, ohne dabei meine Entfaltungsmöglichkeiten einzuschränken.

Zum Gelingen und zur Durchführung dieser Arbeit hat F. Sommer in großer Maße beigetragen. Als Betreuer hatte er immer Zeit für grundlegende Diskussionen, oder aber auch für ein Schwätzchen.

Sybrand van der Zwaag möchte ich danken für die Übernahme des Mitberichts, sowie für die indirekte Inspiration, durch seine Veröffentlichungen, für Teile meiner Arbeit.

Meine Bürokollegin Jutta Breuer gebührt ebenfalls ein Platz auf dieser Seite. Nie hat sie es mir merkbar übel genommen, wenn ich sie wieder mit zuviel Quatsch von der Arbeit abgehalten habe.

Auch die andere Doktoranden der legendären ‚*Ersten Generation*‘ möchte ich danken für die einmalig gute Zusammenarbeit und Atmosphäre: Markus, Udo, Inga, Maik und Dieter.

Heiko danke ich wegen der guten Zusammenarbeit, ohne seine Diplomarbeit wäre Kapitel 5 nicht zustande gekommen.

Weiter gilt mein Dank Andreas, Pe und Peter, wegen der täglichen, manchmal wissenschaftlichen, Anregungen während Kaffeepausen und Mittagessen, sowie Sven, Tolga und Ute für die Unterstützung auf den Gebieten der Erfrischungsgetränke, des maschinenbautechnischen Unterrichtes, und der EDV-Beratung.

Die Mitarbeiter der mechanischen und der elektronischen Werkstatt, sowohl als auch die Elektriker, möchte ich danken wegen der, in der Regel Blitzschnelle, Arbeit.

Alle nicht namentlich Erwähnten mögen mir an dieser Stelle verzeihen.

Am Ende möchte ich dem anonymen Steuerzahler danken, daß er die Güte besaß, mich und meine Kollegen zu finanzieren, auch wenn es nicht immer einfach ist, ihm zu erklären, wozu das alles gut ist.